

# DESIGN OF EQUAL DIVISION MICROWAVE POWER DIVIDERS

**M.L. Strydom**

Thesis submitted in partial fulfilment of the requirements for the degree of  
Master of Science in Engineering at the University of Stellenbosch



**Study Supervisors:**

Prof. P. Meyer and Prof. D.B. Davidson

December 2003

## DECLARATION

I, the undersigned, hereby declare that the work contained in this thesis is my own original work and that I have not previously in its entirety or in part submitted it at any university for a degree.

M.L. Strydom

8 October 2003

## **Abstract**

Equal division microwave power dividers are investigated in this study. A wideband Wilkinson power divider and a wideband directional coupler with a centre frequency of 10 GHz were built. The design of the directional coupler is scaled, such that it can be used between 18 and 40 GHz. The details of the electromagnetic analyses of these structures are discussed and physical implementation issues are investigated.

In a complementary study to the design of planar microwave dividers, the FDTD computational method was implemented and used to analyse the Wilkinson divider and the 18 to 40 GHz directional coupler.

Results are compared to those obtained from commercial numerical method packages and in the case of the Wilkinson divider, to measured results.

Suggestions are made for improvements in the implementation of the directional coupler and methods for a more efficient FDTD implementation are discussed.

## Opsomming

Mikrogolf drywings verdelers wat gelyk verdeel, word in hierdie studie ondersoek. 'n Wyeband Wilkinson verdeler en wyeband gerigte koppelaar met 'n senter frekwensie van 10 GHz is gebou. Die ontwerp van die gerigte koppelaar is ook geskaleer sodat die ontwerp gebruik kan word tussen 18 en 40 GHz. Die details van die elektromagnetiese analise van hierdie strukture word bespreek en kwessies rondom die implementering van die strukture word ondersoek.

In 'n komplementêre studie, is die Eindige Verskil Tyd Gebied numeriese metode (Engels: FDTD) geïmplementeer en gebruik om die Wilkinson en die 18 tot 40 GHz gerigte koppelaar te analiseer.

Resultate word vergelyk met resultate verkry met numeriese metodes geïmplementeer in kommersieële pakkette, en in die geval van die Wilkinson verdeler, ook met gemete resultate.

Aanbevelings word verder gemaak vir verbeterings in die implementering van die gerigte koppelaar asook metodes om 'n meer effektiewe FDTD kode te implementeer.

"The future is not set. There is no fate but what you make for yourself"

*John Connor - Terminator 2*

## ACKNOWLEDGEMENTS

I wish to express my sincere gratitude to the following persons and organisations who contributed to the successful completion of this study project:

- Prof. P. Meyer, who has left deep footprints in my life, both on an academic and on a personal level. He made it possible for me to realise a life dream and exposed me to experiences that fundamentally changed my view of the world. For this I will always be grateful. I thank him for unwavering support, sharing of his knowledge and for showing me Switzerland.
- Prof. D.B. Davidson, whose passion for the field of electromagnetics and, later, computational electromagnetics is the source of my interest and excitement for this field.
- David Howie, along with Avitronics, who made it financially viable for me to finish this degree.
- Dries van Schalkwyk and Applied Wave Research, Inc., who kindly made a personal licence of Microwave Office<sup>®</sup> available to me for use at home. His friendliness and support will always be remembered.
- EMSS, who also made a licence available to me for FEKO<sup>®</sup>.
- Wessel Croukamp and Ashley Cupido, for their willingness to help and their ability in manufacturing the intricate devices.
- Cornell van Niekerk, for his advice and for helping me with the final measurements.
- Marlize Schoeman, for teaching me the basics of using L<sup>A</sup>T<sub>E</sub>X.
- Mandy Hope, for teaching me the basics of using AutoCAD<sup>®</sup> and for drawing the manufacturing specification of the low frequency coupler attached at the end of the thesis.
- Walter Piel, for writing a mesh generating MATLAB<sup>®</sup> file for use in my FDTD code.
- My family, for their love and support through the years and specifically for my mother, for showing me her strength.
- For Vitto and Alanis, who in many ways have shaped my views on life.
- And finally, my biggest thanks go to my friend and soul mate, Walter Piel, who taught me the meaning of life and still continues to amaze me every day. I thank him for his patience and support for all I choose to do.

# Table of Contents

<b>Table of Contents</b>	<b>i</b>
<b>1 Introduction</b>	<b>1</b>
<b>2 Definitions and Terminology</b>	<b>5</b>
<b>3 Directional Coupler</b>	<b>7</b>
3.1 Network Theory of Ideal Couplers . . . . .	7
3.2 Coupler Design at centre Frequency 10 GHz . . . . .	12
3.2.1 Coupling in Terms of Even-Mode Characteristic Impedance . . . . .	12
3.3 Tandem Coupling . . . . .	17
3.4 Design of a $-8.34$ dB Coupler . . . . .	18
3.5 Implementing the Coupler . . . . .	23
3.5.1 Electromagnetic Analysis . . . . .	24
3.5.2 Implementation Issues . . . . .	30
3.5.3 TE and TM Modes . . . . .	33
3.6 Results: Low Frequency Coupler . . . . .	34
3.6.1 EM Results . . . . .	34

*CONTENTS*

ii

3.6.2	Measurement and Final Results . . . . .	36
3.7	A $-3$ dB Coupler with centre Frequency 29 GHz . . . . .	43
3.8	Conclusion . . . . .	47
<b>4</b>	<b>Wilkinson Power Divider</b>	<b>49</b>
4.1	Introduction . . . . .	49
4.2	Analysis . . . . .	50
4.2.1	Finding the S-Parameters of a Wilkinson Divider . . . . .	52
4.3	Implementing the Wilkinson Divider . . . . .	58
4.3.1	Discontinuities due to a Step in Conductor Width . . . . .	58
4.3.2	Y-Junctions . . . . .	61
4.3.3	Non-ideal Behaviour of Resistors at High Frequency . . . . .	64
4.3.4	Connectors and Right-Angled Bends . . . . .	67
4.4	Results: Wilkinson Divider . . . . .	68
4.4.1	Layout . . . . .	68
4.5	Measurement . . . . .	69
4.5.1	Discussion of Results . . . . .	70
4.6	Conclusion . . . . .	73
<b>5</b>	<b>Power Handling</b>	<b>75</b>
5.1	Introduction . . . . .	75
5.2	Peak Power . . . . .	75
5.3	Average Power . . . . .	76
5.4	Predicted Power Handling Capability of Coupler . . . . .	76

<i>CONTENTS</i>	iii
5.5 Conclusion . . . . .	80
<b>6 FDTD</b>	<b>81</b>
6.1 Introduction . . . . .	81
6.1.1 PML and UPML (Uniaxial PML) . . . . .	83
6.1.2 Implementation of UPML in FDTD . . . . .	88
6.1.3 Results . . . . .	96
6.2 Implementing the Devices into the FDTD Code . . . . .	101
6.2.1 Wilkinson Divider . . . . .	106
6.2.2 Analysis of the High Frequency Coupler . . . . .	109
6.3 Conclusion . . . . .	114
<b>7 Recommendations</b>	<b>115</b>
<b>8 Conclusion</b>	<b>117</b>
<b>A Port Reflections</b>	<b>119</b>
A.1 Calculation of $S_{11}$ . . . . .	119
A.2 Calculation of $S_{22}$ and $S_{33}$ . . . . .	121
<b>B Magnetic Fields of the UPML</b>	<b>123</b>
B.1 Physical Location of UPML Magnetic Fields . . . . .	123
B.2 Computer Position of UPML Magnetic Fields . . . . .	125
<b>C UPML</b>	<b>126</b>
C.1 Proof that the UPML region is matched for all angles, polarisation and frequency of incident field . . . . .	126

<i>CONTENTS</i>	iv
<b>D Detailed Track Dimensions for Couplers</b>	<b>130</b>
<b>E Datasheets</b>	<b>132</b>
E.1 Radiall R125.484.000 SMA Connector . . . . .	132
E.2 Mini-Systems, Inc. Microwave Chip Resistor . . . . .	132
E.3 Taconic TLY-5 Laminate . . . . .	132
<b>F Technical Drawing</b>	<b>137</b>
F.1 Low Frequency Coupler . . . . .	137
<b>Bibliography</b>	<b>140</b>

# List of Figures

3.1	Four Port Representation . . . . .	7
3.2	Bisection of a Coupler . . . . .	9
3.3	Bisection of Uniformly Coupled Lines . . . . .	10
3.4	Ideal Coupling . . . . .	14
3.5	Required Function for Obtaining Ideal Response . . . . .	15
3.6	Ideal Coupling Function . . . . .	16
3.7	Representation of Tandem Coupler Layout . . . . .	17
3.8	Location of weighting functions . . . . .	21
3.9	Coupler Division . . . . .	21
3.10	Response of a $-8.34$ dB Coupler Using Ideal Components . . . . .	23
3.11	Positioning of the substrate layers . . . . .	24
3.12	Widths and Offsets of Coupler . . . . .	25
3.13	Completed $-8.34$ dB Coupler . . . . .	25
3.14	EM Results of $-8.34$ dB Coupler . . . . .	29

*LIST OF FIGURES*

vi

3.15 Right-Angled Bends . . . . .	30
3.16 Discontinuities in Connector Transition . . . . .	31
3.17 Designed Connector Transition . . . . .	32
3.18 Reflection due to Connector Transition . . . . .	32
3.19 Layout of the Low Frequency Coupler . . . . .	34
3.20 Calculated S-Parameters of Low Frequency Coupler . . . . .	35
3.21 Calculated Power Division Results of Low Frequency Coupler . . . . .	36
3.22 Measured Results: Coupler $ S_{21} $ and $ S_{31} $ . . . . .	37
3.23 Measured Results: Coupler $ S_{11} $ and $ S_{41} $ . . . . .	38
3.24 Effect of Non-Ideal Parameters (a) . . . . .	40
3.25 Effect of Non-Ideal Parameters (b) . . . . .	41
3.26 Measured Parameters of 50 $\Omega$ Terminations . . . . .	42
3.27 T Parameters . . . . .	43
3.28 Effect of Gender Changers . . . . .	44
3.29 CST Low frequency Coupler results . . . . .	45
3.30 Layout of the High Frequency Coupler. . . . .	45
3.31 EM Analysis of HF Coupler Showing $ S_{21} $ and $ S_{31} $ . . . . .	46
3.32 EM Analysis of HF Coupler Showing $ S_{11} $ , $ S_{21} $ , $ S_{31} $ and $ S_{41} $ . . . . .	46
3.33 The Completed $-3$ dB Coupler . . . . .	48

*LIST OF FIGURES*

vii

4.1	Bisection of Wilkinson Divider . . . . .	51
4.2	Wilkinson Divider with $N=3$ . . . . .	52
4.3	Circuit for Calculating $S_{21}$ . . . . .	54
4.4	Ideal S-Parameters of Wilkinson Divider with $N=3$ . . . . .	57
4.5	Ideal Power Division of Wilkinson Divider with $N=3$ . . . . .	57
4.6	Reactance of Step Discontinuities . . . . .	58
4.7	$S_{11}$ of Step Discontinuities . . . . .	60
4.8	Phase Error of Step Discontinuities . . . . .	60
4.9	Impedances of the Y-junction . . . . .	61
4.10	Lumped Element Representation . . . . .	61
4.11	Definition of Angles . . . . .	62
4.12	$S_{11}$ of Y-Junctions . . . . .	63
4.13	Electrical Lengths of Y-Junctions . . . . .	64
4.14	High Frequency Model of a Resistor . . . . .	64
4.15	Non-ideal Resistor . . . . .	65
4.16	Non-ideal Isolation Properties . . . . .	66
4.17	Reflection Caused by Connector Transition . . . . .	67
4.18	Layout of the Wilkinson Divider . . . . .	68
4.19	Measured Results: Wilkinson Divider . . . . .	70
4.20	Isolation . . . . .	71

4.21	Effect of Non-Ideal $50 \Omega$ Terminations on the Input Reflection of the Wilkinson Divider . . . . .	72
4.22	Effect of Non-Ideal $50 \Omega$ Terminations on the Power Division of the Wilkinson Divider . . . . .	72
4.23	The Completed Wilkinson Divider . . . . .	74
6.1	The Yee Cell . . . . .	90
6.2	3D UPML Regions . . . . .	94
6.3	Illustrating $\sigma_{max}$ . . . . .	95
6.4	UPML and Errors . . . . .	96
6.5	Hertzian Hard Source . . . . .	98
6.6	Observation Points . . . . .	100
6.7	Local E-field Error . . . . .	100
6.8	Cross Section of $50 \Omega$ port (Excitation Plane) with Locations of Excitation Fields Indicated . . . . .	102
6.9	Wilkinson Divider Model . . . . .	106
6.10	Own FDTD: $ S_{21} $ of Wilkinson divider . . . . .	107
6.11	Own FDTD: $ S_{11} $ of Wilkinson Divider . . . . .	108
6.12	Screenshot of Wilkinson Divider . . . . .	109
6.13	Layout of $-8.34$ dB Coupler Used in FDTD Analysis . . . . .	109
6.14	Location of Integral for Determining S-Parameters . . . . .	111
6.15	Own FDTD: S-Parameters of HF Coupler . . . . .	112

*LIST OF FIGURES*

ix

6.16 Screenshot of HF Coupler . . . . .	113
6.17 Effect of UPML . . . . .	113
A.1 Definition of Nodes . . . . .	120
A.2 Definition of Nodes for $S_{22}$ . . . . .	121
D.1 Location of Widths and Offsets for a Broadside Coupler . . . . .	130

# List of Tables

1.1	Characteristics of Power Dividers . . . . .	2
2.1	Symbols and Their Units . . . . .	5
2.2	Explanation of Acronyms . . . . .	6
2.3	Explanation of Terminology . . . . .	6
3.1	Required Even-Mode Impedances and Weighting Functions for $-8.34$ dB Coupler . . . . .	20
3.2	Required Even and Odd Mode Impedances for Discretised $-8.34$ dB Coupler	22
3.3	Material Properties of Taconic TLY-5 . . . . .	24
3.4	Approximate Cutoff Frequencies and Modes in the Low Frequency Coupler	33
4.1	Cutoff Frequencies and Modes in the Wilkinson Divider . . . . .	69
5.1	Material Properties of Selected Substrates . . . . .	76
5.2	Comparison of APHC for Various Substrates . . . . .	79
6.1	Location of the Fundamental Field Coordinates in the Yee-Cell . . . . .	90

*LIST OF TABLES*

6.2	Coding Tradeoffs . . . . .	101
6.3	Allocation of Matrices . . . . .	102
D.1	Track Dimensions for Low-Frequency Coupler . . . . .	131
D.2	Track Dimensions for High-Frequency Coupler . . . . .	131

# Chapter 1

## Introduction

Power division forms an integral part of many microwave components, such as solid-state power amplifiers, mixers and active circulators. Power dividers are also used extensively in MMIC (monolithic microwave integrated circuits) designs [27] and in antenna array feeding networks [39, p135]. Couplers are used in the design of high frequency capacitors, inductors, transformers and DC blocks [26].

Cohn and Levy [12], did an investigation of the history of microwave power dividers and found that the earliest traceable power divider was patented in 1927, although most of the early development on these components was made during the Second World War (1939 to 1945).

Power division can be achieved through many different means. The choice of method depends primarily on the frequency band of interest and the amount of power to be divided. Two way power division is achieved through three or four-port networks, which are commonly implemented using coaxial cable, microstrip, stripline or waveguide. Three-port networks cannot be lossless and matched at all ports, whereas this can be achieved with four-port networks. These four-port networks (commonly called ‘couplers’), make use of electromagnetic coupling between ports to transfer power and always exhibit a phase difference between the output ports. The coupling occurs as a result of different characteristic impedances of the coupler lines when excited in the even and odd modes.

The simplest and least expensive method of manufacturing dividers at frequencies above 1 GHz, is in microstrip or stripline. When compared to the alternatives, it is found that

a design is easily implemented in these planar structures and substrates with the required properties are commercially available.

Some of the options that are available to achieve power division using microstrip and stripline are summarised in table 1.1.

**Table 1.1:** Characteristics of Commonly Found Power Dividers and Couplers

<i>Coupler/divider</i>	<i>Bandwidth</i>	<i>Phase difference in output [degrees]</i>	<i>Coupling /Division</i>	<i>Isolation</i>	<i>Other</i>
Rat-race	Medium	90	High	Good	
Branch line coupler	Medium	90	High	Good	
<b>Cascaded non-uniform coupler</b>	<b>High</b>	<b>90</b>	<b>High</b>	<b>Good</b>	
Coupled line (multisection)	High	90	Medium	Good	
Lange	High	90	Medium	Good	Difficult to realise
Tapered coupler	High	90	Medium	Good	
T-junction	Low	0	High	None	
Wilkinson (multisection)	High	0	High	Good	Difficult to realise at high frequencies

Rat race and branch-line couplers, though suitable for obtaining tight coupling ( $-3$  dB), are inherently narrowband. Techniques to enhance their bandwidth are available and include replacing selected lines with equivalent coupled line sections [26]. A Lange coupler achieves its tight coupling by connecting a number of lines in an interdigital way. Interdigital coupling refers to the parallel connecting of several lines so that the fringing fields at both edges of a line contribute to the coupling. Lange couplers are difficult to fabricate as the lines are very narrow and close together and the bonding wires, which connect the lines, are difficult to manufacture.

Multisection coupled line couplers are made up of contiguously placed coupled line sections. They can achieve decade bandwidths, but coupling levels are low. Cascaded non-uniform couplers cascade the multisection coupled line couplers in order to achieve high coupling levels.

The two-way Wilkinson divider is a three port network. It uses physical division of lines to achieve power division, as opposed to electromagnetic couplers that use coupling of

fields. Wilkinson dividers are ideal for implementation at frequencies under 15 GHz.

This study project describes the development of a 3 dB coupler and an equal split (3 dB) Wilkinson power divider operating in the frequency range 6.2 to 13.8 GHz (bandwidth ratio = 2.22). A full 3D time domain computational method (Finite Difference Time Domain method or FDTD) is implemented, which is particularly suited for broadband applications and finally, the low frequency coupler is scaled for operation between 18 and 40 GHz (bandwidth ratio = 2.2).

The main reason for choosing FDTD as the computational method to verify the response of the coupler at high frequencies, is that the FDTD directly calculates the impulse response of an electromagnetic system. A single FDTD simulation can thus provide ultrawideband information.

The FDTD has become very popular due to the limitless number of structures that can be analysed. Implementing a new structure is a meshing problem, unlike for instance, the Method of Moments (MOM), which requires calculation of structure-dependent Green's functions.

An important contributing factor in the popularity of the FDTD, was the invention of the Perfectly Matched Layer (PML). The PML is a mesh terminating scheme that introduces very little reflection into the computational domain. (For many structures this will be less than  $-100$  dB). The beauty of the PML is that plane waves of arbitrary incidence, polarization and frequency are matched at the boundary.

Chapter 3 shows the complete design for a 3 dB directional coupler at a centre frequency of 10 GHz. It includes development of the theory, explains the necessity for using cascaded couplers and does a study on correct implementation of the design. Before presenting the results of the measured coupler, a detailed study is done on proper EM simulation practices.

Chapter 3.7 summarizes the design of the coupler scaled to a higher frequency and shows simulated results.

Chapter 4 analyses a 3 section Wilkinson power divider at centre frequency 10 GHz, investigates the behaviour of resistors at high frequencies and ends the chapter with measured results.

Chapter 5 investigates power associated with microstrip and stripline configurations and calculates the predicted power handling capability of the coupler and Wilkinson divider.

In chapter 6, a 3D FDTD implementation is done using a boundary termination scheme called the Uniaxial Perfectly Matched Layer (UPML). Results are compared to published results. The details of implementing the Wilkinson divider and the high frequency coupler into the FDTD are discussed and results are presented.

# Chapter 2

## Definitions and Terminology

**Table 2.1:** Symbols and Their Units

<i>Symbol</i>	<i>Definition</i>	<i>Value</i>	<i>Unit</i>
$\epsilon$	Electrical permittivity		F/m
$\epsilon_r$	Relative permittivity		dimensionless scalar
$\epsilon_0$	Free-space permittivity	$8.854 \times 10^{-12}$	F/m
$\mu$	Magnetic permeability		H/m
$\mu_r$	Relative permeability		dimensionless scalar
$\mu_0$	Free-space permeability	$4\pi \times 10^{-7}$	H/m
$\lambda$	Wavelength		m
$\lambda_m$	Wavelength in the medium		m
$c$	Speed of light in free space	$2.9979 \times 10^8$	m/s
$\vec{E}$	Electric field strength		V/m
$\vec{E}$	Time harmonic Electric field		V/m
$Z_0$	Characteristic impedance		$\Omega$
$\eta$	Intrinsic impedance	$\sqrt{\frac{\mu}{\epsilon}}$	$\Omega$
$\tan \delta$	Loss tangent		Dimensionless

**Table 2.2:** Explanation of Acronyms

<i>Acronym</i>	<i>Meaning</i>
3D	Three-dimensional
ABC	Absorbing Boundary Condition
APHC	Average Power Handling Capability
AWR	Applied Wave Research
CST	Computer Simulation Technology
dB	Decibel
EM	Electromagnetic
FDTD	Finite Difference Time Domain
GHz	Giga Hertz
MB	Mega Bytes
MMIC	Monolithic Microwave Integrated Circuits
MOM	Method of Moments
MWO	Microwave Office
PEC	Perfect Electric Conductor
PML	(Berenger's) Perfectly Matched Layer
PPHC	Peak Power Handling Capability
RAM	Random Access Memory
RF	Radio Frequency
SMA connector	Subminiature Type A Connector
TE	Transverse Electric
TEM	Transverse Electromagnetic
TM	Transverse Magnetic
UPML	Uniaxial Perfectly Matched Layer

**Table 2.3:** Explanation of Terminology

<i>Term</i>	<i>Explanation</i>
Computational domain (FDTD)	Region undergoing numerical analysis (excluding UPML regions)
Hard Source (FDTD)	When a desired time function is assigned to a specific component of the E field or H field in the FDTD space lattice
Soft Source (FDTD)	A desired time function is added to the E or H field component already present in the FDTD space lattice

## Chapter 3

# Design of a $-3$ dB Microwave Coupler at 10 GHz

### 3.1 Network Theory of Ideal Couplers

Three-port networks cannot be lossless, reciprocal and matched at all ports [31]. If the network is made lossy, it is possible to obtain a divider that has all outputs matched with isolation between the output ports. The Wilkinson divider is such a network and is discussed in detail in chapter 4. In this chapter, a four port directional coupler is discussed.

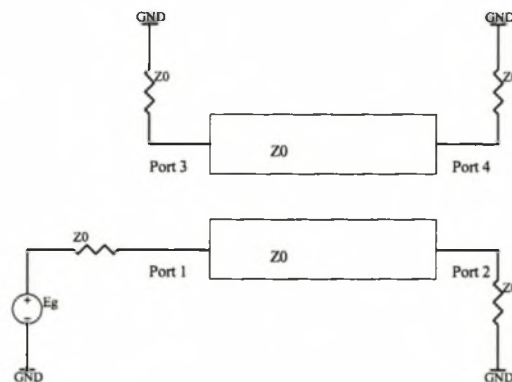


**Figure 3.1:** A Four Port Network Composed of Uniform Coupled Transmission Lines

In general, four-port couplers have the following properties:

The ideal coupler is passive, it contains no anisotropic materials and is therefore reciprocal ( $S_{ij} = S_{ji}$ ) and its S-parameter matrix is symmetric.

All ports are matched ( $S_{ii} = 0$ ) and the network is lossless. Energy conservation requires that the scattering matrix be unitary. In matrix notation this is written as  $[S]^t[S]^* = [I]$ .

In finding the values of the S-parameters, the above mentioned conditions will result in ten equations. Refer to [31, p355] for a full derivation. The S-parameter matrix of an ideal symmetrical coupler is summarised in equation 3.1.

$$\begin{bmatrix} 0 & \alpha & j\beta & 0 \\ \alpha & 0 & 0 & j\beta \\ j\beta & 0 & 0 & \alpha \\ 0 & j\beta & \alpha & 0 \end{bmatrix} \quad (3.1)$$

where  $\beta$  is the coupling and  $|\alpha|^2 + |\beta|^2 = 1$ . For equal power division,  $\alpha = \beta = \frac{1}{\sqrt{2}} = -3dB$

Consider now these S-parameters as they apply to coupled lines where an even and odd mode excitation is used.

Firstly, note that the S-parameters in equation 3.1, can be written as in equation 3.2:

$$[\mathbf{S}] = \begin{bmatrix} [\mathbf{S}_A] & [\mathbf{S}_B] \\ [\mathbf{S}_B] & [\mathbf{S}_A] \end{bmatrix} \quad (3.2)$$

where

$$[\mathbf{S}_A] = \begin{bmatrix} 0 & \alpha \\ \alpha & 0 \end{bmatrix} \quad [\mathbf{S}_B] = \begin{bmatrix} j\beta & 0 \\ 0 & j\beta \end{bmatrix} \quad (3.3)$$

A broadside coupler bisected into even and odd mode excitation is shown in Figure 3.2. Part (a) shows the equivalent circuit for even excitation and part (b) shows the equivalent circuit for odd excitation.

It can be shown that the  $[\mathbf{S}_A]$  and  $[\mathbf{S}_B]$  matrices can be written as [p129][26]:

$$[\mathbf{S}_A] = \begin{bmatrix} \frac{S_{11e} + S_{11o}}{2} & \frac{S_{21e} + S_{21o}}{2} \\ \frac{S_{21e} + S_{21o}}{2} & \frac{S_{22e} + S_{22o}}{2} \end{bmatrix} \quad (3.4)$$

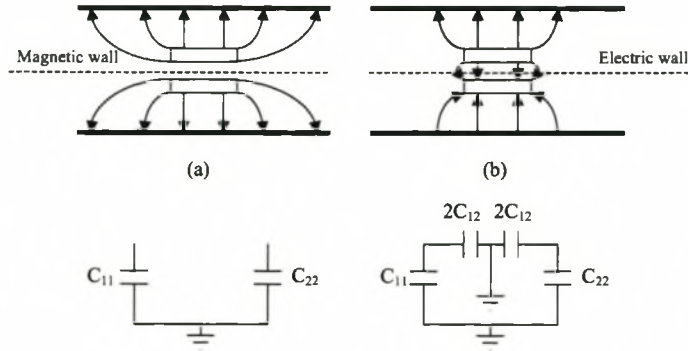


**Figure 3.2:** Even and Odd Mode Bisections of a Broadside Coupler

and

$$[\mathbf{S}_B] = \begin{bmatrix} \frac{S_{11e} - S_{11o}}{2} & \frac{S_{21e} - S_{21o}}{2} \\ \frac{S_{21e} - S_{21o}}{2} & \frac{S_{22e} - S_{22o}}{2} \end{bmatrix} \quad (3.5)$$

such that the S-parameters of the four port network become:

$$\begin{aligned} S_{11} &= \frac{S_{11e} + S_{11o}}{2} & S_{12} &= S_{21} & S_{13} &= S_{31} & S_{14} &= S_{41} \\ S_{21} &= \frac{S_{21e} + S_{21o}}{2} & S_{22} &= \frac{S_{22e} + S_{22o}}{2} & S_{23} &= S_{41} & S_{24} &= \frac{S_{22e} - S_{22o}}{2} \\ S_{31} &= \frac{S_{11e} - S_{11o}}{2} & S_{32} &= S_{41} & S_{33} &= S_{11} & S_{34} &= S_{21} \\ S_{41} &= \frac{S_{21e} - S_{21o}}{2} & S_{42} &= S_{24} & S_{43} &= S_{21} & S_{44} &= S_{22} \end{aligned} \quad (3.6)$$

The  $e$  and  $o$  subscripts refer to ‘even mode’ and ‘odd mode’.

The requirement for matched ports is that  $S_{11} = S_{22} = 0$ . From equation 3.6, this is satisfied when

$$\begin{aligned} S_{11e} &= -S_{11o} \\ S_{22e} &= -S_{22o} \end{aligned} \quad (3.7)$$

where these terms are not equal to zero. In the case where they are equal to zero, it will result in forward wave (co-directional) couplers. The length of a forward wave coupler decides the amount of power transferred. Theoretically it is possible to transfer all power to the coupled port of a forward wave coupler. The limitation is that the coupling depends on the electrical length of the lines and such a coupler is therefore relatively narrow band.

Substituting equation 3.7 into equation 3.6, it is found that

$$S_{31} \neq 0, S_{42} \neq 0 \quad (3.8)$$

To ensure that no power is coupled in the forward direction on the coupled line, it is required that  $S_{41} = 0$ . This is satisfied (from equation 3.6) when

$$S_{21_e} = S_{21_o} \quad (3.9)$$

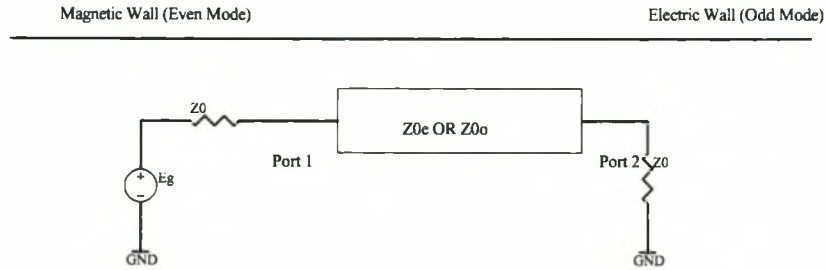


**Figure 3.3:** Even and Odd-Mode Bisections of Uniformly Coupled Lines

**Finding the values of the S-Parameters** Figure 3.3 is one half of the transmission line representation of the coupler in Figure 3.1. This figure shows that the two conductors of the coupler will always be separated by either an open circuit or a short circuit when excited in the even and odd mode. The circuit can thus be analysed by looking at only one of the transmission lines. The S-parameters of the single transmission line can be found from the ABCD parameters for two port circuits. ([31, p208] and [26, p54]). The even and odd mode parameters are summarised in equations 3.10 and 3.11.

$$ABCD_e = \begin{bmatrix} \cos(\beta l) & jZ_{0_e} \sin \beta l \\ jY_{0_e} \sin \beta l & \cos \beta l \end{bmatrix} \quad (3.10)$$

$$ABCD_o = \begin{bmatrix} \cos(\beta l) & jZ_{0_o} \sin \beta l \\ jY_{0_o} \sin \beta l & \cos \beta l \end{bmatrix} \quad (3.11)$$

$Z_{0_e}$ ,  $Y_{0_e}$ ,  $Z_{0_o}$  and  $Y_{0_o}$  refer to the characteristic impedances and admittances of the even and odd modes respectively.  $l$  is the length of the transmission lines. The S-Parameters are found from conversion tables [26, p136].  $S_{11}$  is shown in equations 3.12 and 3.13 :

$$S_{11_e} = S_{22_e} = \frac{j\left(\frac{Z_{0_e}}{Z_0} - \frac{Z_0}{Z_{0_e}}\right) \sin \beta l}{2 \cos \beta l + j\left(\frac{Z_{0_e}}{Z_0} + \frac{Z_0}{Z_{0_e}}\right) \sin \beta l} \quad (3.12)$$

$$S_{11_o} = S_{22_o} = \frac{j\left(\frac{Z_{0_e}}{Z_0} - \frac{Z_0}{Z_{0_o}}\right) \sin \beta l}{2 \cos \beta l + j\left(\frac{Z_{0_e}}{Z_0} + \frac{Z_0}{Z_{0_o}}\right) \sin \beta l} \quad (3.13)$$

Condition 3.7 will be satisfied if

$$\frac{Z_{0_e}}{Z_0} = \frac{Z_0}{Z_{0_o}} \quad (3.14)$$

for any arbitrary value of length  $l$  in equations 3.12 and 3.13.

Under this condition, it is found that  $S_{31} = S_{13} = S_{24} = S_{42} = \frac{S_{11_e} - S_{11_o}}{2} = S_{11_e}$ .

To obtain the S-parameters in the format in which it will be used for further designs, define a constant  $k$ , where  $k$  is defined by

$$k = \frac{Z_{0_e} - Z_{0_o}}{Z_{0_e} + Z_{0_o}} \quad (3.15)$$

Substituting equation 3.15 in equation 3.12, results in the expression for the coupling;

$$S_{31} = \frac{jk \sin \theta}{\sqrt{1 - k^2} \cos \theta + j \sin \theta} \quad (3.16)$$

From equation 3.16, the maximal coupling between ports 1 and 3 occurs when  $\theta = \beta l = \pi/2$ , in which case  $S_{31} = S_{13} = S_{24} = S_{42} = k$ .

In a similar way, the other S-Parameters, listed in 3.17 can be found.

$$[\mathbf{S}] = \begin{bmatrix} 0 & -j\sqrt{1 - k^2} & k & 0 \\ -j\sqrt{1 - k^2} & 0 & 0 & k \\ k & 0 & 0 & -j\sqrt{1 - k^2} \\ 0 & k & -j\sqrt{1 - k^2} & 0 \end{bmatrix} \quad (3.17)$$

where  $k$  is now seen to be the coupling between port 1 and 3.

## 3.2 The design of a nonuniform $-3$ dB coupler at centre frequency 10 GHz

Designing in the microwave frequency band (above approximately 3 GHz) is complicated by the fact that the wavelengths become comparable in size to discontinuities in the microwave structure. This adversely affects the input impedance of the structure [21].

By minimising the physical discontinuities, the performance of the structure will be greatly improved. In the case of the coupler, these physical discontinuities are a result of lines with different characteristic impedances. A coupler which uses a nonuniform method to implement the different characteristic impedances, such that the discontinuities are minimised, has been developed and is called a ‘Nonuniform Coupler’ ([28][41] and [21]).

### 3.2.1 Coupling in Terms of Even-Mode Characteristic Impedance

It was showed that the coupling ( $S_{31}$ ) of the coupler is equal to the even mode reflection coefficient ( $S_{11e}$ ) when the even and odd mode impedances satisfy the condition:

$$Z_{0e}(z)Z_{0o}(z) = Z_0^2 \quad (3.18)$$

The aim is to obtain an expression for  $S_{11e}$ , keeping in mind partial reflection at every mismatch in impedance. This is done using a simple version of the theory of small reflections, where the total reflection coefficient at the input is found by summing differential contributions of the reflection coefficient from each step in phase. The differential reflection at a step discontinuity in the impedance is calculated as shown in equation 3.19.

$$\begin{aligned} d\tau &= \frac{Z_{0e} + dZ_{0e} - Z_{0e}}{Z_{0e} + dZ_{0e} + Z_{0e}} \approx \frac{dZ_{0e}}{2Z_{0e}} \\ &= \frac{1}{2}d(\ln Z_{0e}) \\ &= \frac{1}{2} \frac{d}{dz}(\ln Z_{0e})dz \end{aligned} \quad (3.19)$$

where  $Z_{0e}$  is a function of distance ( $z$ ) and  $2Z_{0e} \gg dZ_{0e}$ .

The total reflection coefficient can be obtained by adding a phase term to 3.19 and summing the contributions over the length of the coupler, such that:

$$S_{11e} = \frac{1}{2} \int_0^d e^{-2j\beta z} \frac{1}{2} \frac{d}{dz}(\ln Z_{0e})dz \quad (3.20)$$

where  $d$  is the length of the divider (in meters).

This expression is non-zero only between  $z = 0$  and  $z = d$ . A new coordinate is defined in terms of  $z$  and  $d$ .

$$u = z - \frac{d}{2}, \quad (3.21)$$

Under the condition that  $S_{11e} = S_{31}$  as explained previously,  $S_{31}$  can then be written in terms of  $u$ .

$$S_{31}e^{j\beta d} = \int_{-\infty}^{\infty} e^{-2j\beta u} p(u) du \quad (3.22)$$

where  $p(u)$  is defined by

$$p(u) = \frac{1}{2} \frac{d}{du} (\ln Z_{0e}). \quad (3.23)$$

Note that  $p(u)$  is also the inverse Fourier transform of  $S_{31}$ :

$$p(u) = \frac{1}{2\pi} \int_{-\infty}^{\infty} S_{31} e^{j\beta d} e^{j2\beta u} d(2\beta), \quad (3.24)$$

where  $d(2\beta)$  denotes integration with respect to  $2\beta$ .

It becomes clear that by choosing an appropriate  $p(u)$  function, it is possible to obtain a desired coupling response.

As an example, consider Figure 3.4, which shows the magnitude of the coupling of an ideal coupler. The y-axis shows the voltage coupling factor  $k$ , and this is plotted against  $\beta$ , as  $\beta$  is the variable of integration in equation 3.24. The phase constant  $\beta$  is related to the frequency  $f$  by the relation

$$\beta = \frac{2\pi f}{v} \quad (3.25)$$

where  $v$  is the phase velocity along the direction of propagation.

$S_{31}$  for this coupling can be written as

$$\begin{aligned} S_{31} &= ke^{j(\pi/2 - \beta d)}, \text{ for } 0 < 2\beta < 1 \\ &= ke^{-j(\pi/2 + \beta d)}, \text{ for } -1 < 2\beta < 0 \\ &= 0 \text{ otherwise,} \end{aligned} \quad (3.26)$$

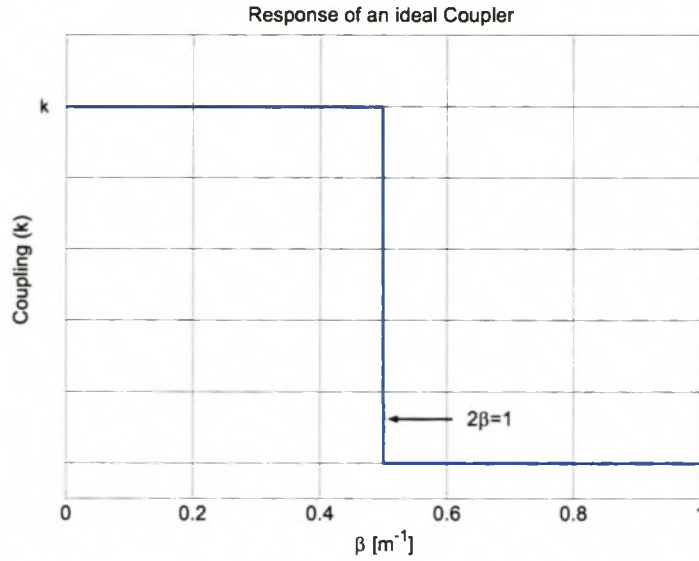


**Figure 3.4:** Ideal Coupling Obtained when using an Infinitely Long Coupler

such that the  $p(u)$  function in equation 3.24 becomes

$$p(u) = -\frac{k \sin^2(u/2)}{\pi u/2}. \quad (3.27)$$

The inverse Fourier transform of Figure 3.4 is shown in Figure 3.5. This figure is the  $p(u)$  function (equation 3.27) required to obtain the ideal response. The unit on the x-axis is a distance function (equation 3.21). From this figure one can see that an infinitely long divider is required to obtain an ideal coupling response. Approximating the ideal response with a finite coupler length (or a finite number of Fourier terms), will result in an approximation of the ideal response, which will be seen in the form of ripple in the passband and overshoot near  $\beta = 0$ . This problem is resolved by employing weighting functions and defining a new function as

$$p_w(u) = w(u)p(u) \quad (3.28)$$

where  $w(u)$  is a weighting function and  $p(u)$  is as defined in equation 3.27.

The even-mode impedance can be calculated by equating equations 3.23 and 3.28 and solving the result as an integral:

$$\frac{1}{2} \ln \frac{Z_{0e}(u)}{Z_0} = \frac{k}{\pi} \int_{-d/2}^u w(u)p(u)du = -\frac{k}{\pi} \int_{-d/2}^u w(u) \frac{\sin^2(u/2)}{u/2} du \quad (3.29)$$

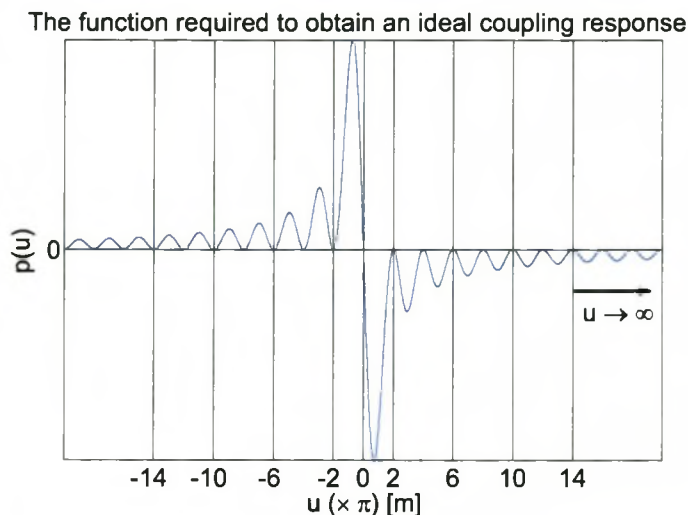


**Figure 3.5:**  $p(u)$  Function Required to Obtain an Ideal Coupling Response

This integral can be evaluated numerically. Refer to [26, p229] for an example on how to evaluate this numerical integral properly.

Thus, in order to design a nonuniform, broadband TEM directional coupler, it is necessary to express the even-mode impedance as a function of the distance along the coupler.

The weighting function is obtained by obtaining a Fourier series representation for the function in Figure 3.6. This figure represents an ideal coupling of  $k$  in a band of interest. The choice of  $\theta$  as an axis will become clear later in this section.

The Fourier approximation of Figure 3.6 is written in equation 3.30.

$$f(\theta) = k \frac{4}{\pi} \left[ w_1 \sin \theta + w_2 \frac{\sin 3\theta}{3} + \dots + w_n \frac{\sin(2n-1)\theta}{2n-1} \right] \quad (3.30)$$

where  $w_1, \dots, w_n$  are the weighting function terms that will be used to equalise the ripple introduced by using a finite number of terms. With suitable choice of the weighting function,  $f(\theta)$  can be made equal ripple.

A suitable equal ripple function is determined from design tables of symmetrical multi-section couplers. The suggested function is given by: [26, p232] :

$$f(\theta) = \sum_{r=1}^n \ln \frac{z_{0e(n+1-r)}}{z_{0e(n-r)}} \sin(2r-1)\theta \quad (3.31)$$

where  $\theta$  is the electrical length of each of the  $N = 2n - 1$  symmetrical sections, with  $n$

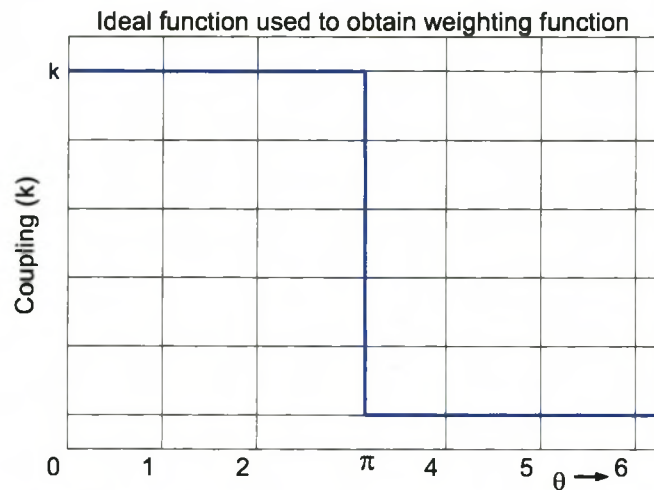


**Figure 3.6:** Function to be Represented by a Finite Number of Fourier Terms in order to Calculate the Weighting Function

the order of the design and  $\theta$  is

$$\theta = \frac{\beta d}{2n - 1} \quad (3.32)$$

In equation 3.31,  $z_{0e(n)}$  is the even mode impedance of each of a standard  $N$ -section coupler. This is the necessary characteristic impedance of the lines to obtain the required coupling and is constant over each line.  $Z_{0e}(z)$  in equation 3.29 is obtained from  $z_{0e(n)}$  by comparing equations 3.30 and 3.31 term by term, to obtain the weighting terms. The integral (equation 3.29) can then be evaluated.

The required values for the even mode impedances for a coupler of  $N$  sections ( $z_{0e(n)}$ ) and specified coupling have been published and are available in reference [26, pp. 200–207].

A detailed evaluation of this theory is presented in section 3.4.

### 3.3 Tandem Coupling

It is difficult to realise a  $-3$  dB nonuniform coupler with high bandwidth as the coupling requirements of the centre section are very high. A way to decrease the tight coupling requirements is to place various couplers of lower coupling coefficient in tandem. [38][20][29]. In this way, the overall coupling factor of  $-3$  dB is achieved across a large bandwidth.

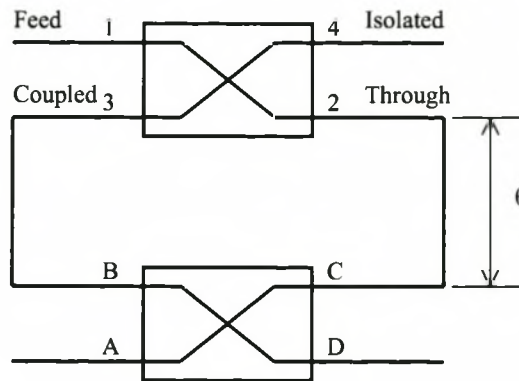


**Figure 3.7:** Representation of Tandem Coupler Layout

The ports of the basic four-port coupling network are defined in the top coupler in Figure 3.7. In a symmetrical coupler such as this, there is a  $90^\circ$  phase shift between ports 2 and 3.

If the signal at port 1 is represented by  $V$ , and the coupling by  $k$ , then, from 3.17, if all ports are matched, the voltages at the ports of the top (ideal) coupler are:

$$\begin{aligned}
 \text{Voltage at Port 1, } V_1 &= V \\
 V_2 &= -j\sqrt{1-k^2}V \\
 V_3 &= kV \\
 V_4 &= 0
 \end{aligned} \tag{3.33}$$

For simplicity in describing the theory, assume  $\theta = 0^\circ$ .

The lower coupler can be seen as having two possible input ports, namely port B or port C. When port C is seen as the input port, the voltages at the ports of the lower coupler

due to the top coupler are shown in equation 3.34.

$$\begin{aligned}
 V_A &= (-j\sqrt{1-k^2})(-j\sqrt{1-k^2})V = (k^2 - 1)V \\
 V_B &= kV \\
 V_C &= -j\sqrt{1-k^2}V \\
 V_D &= -j k\sqrt{1-k^2}V
 \end{aligned} \tag{3.34}$$

When port B is seen as the input port, the voltages on the lower coupler due to the top coupler are summarised in equation 3.35.

$$\begin{aligned}
 V_A &= k^2V \\
 V_B &= kV \\
 V_C &= -j\sqrt{1-k^2}V \\
 V_D &= -j k\sqrt{1-k^2}V
 \end{aligned} \tag{3.35}$$

As port B and C will function as both the feed and isolated ports, the voltages at the output ports (A and D) are a superposition of the individual cases.

$$\begin{aligned}
 V_A &= (2k^2 - 1)V \\
 V_D &= -2jk\sqrt{1-k^2}V
 \end{aligned} \tag{3.36}$$

For a  $-3$  dB coupler,  $V_A$  and  $V_D$  need to have a magnitude of  $0.707$  V. This will be the case when the coupling is  $-8.34$  dB and  $k = 10^{\frac{-8.34}{20}} = 0.383$ . The coupling coefficient and the expected voltages at the output ports of the tandem coupler are summarised in equation 3.37.

$$\begin{aligned}
 k &= 0.383 \text{ (or } -8.34 \text{ dB)} \\
 V_A &= -0.707V \text{ (or } -3 \text{ dB)} \\
 V_D &= -j0.707V \text{ (or } -3 \text{ dB)} \\
 V_4 &= 0V
 \end{aligned} \tag{3.37}$$

It is understood that if  $\theta$  is an increment of  $90^\circ$ , the output voltages will still be purely imaginary or real numbers (as referenced to the input).

### 3.4 Evaluation of $Z_{0e}(z)$ for an Equal Ripple, Symmetrical $-8.34$ dB Coupler of 5 Sections

For a mean coupling of  $-8.34$  dB,  $k = 10^{\frac{-8.34}{20}} = 0.383$ . The bandwidth ratio for the coupler is  $B = \frac{f_2}{f_1} = \frac{13.8 \text{ GHz}}{6.2 \text{ GHz}} = 2.22$ .

Using tables of parameters for symmetrical TEM-mode coupled-transmission-line directional couplers [26, Table 6.1h, p202], it is found that a coupler of three sections will be able to meet the bandwidth requirements. However, since ideal results often deteriorate with implementation, a five section coupler was used.

From the above mentioned tables, the even-mode impedances are found (and is tabulated in table 3.1).

Equation 3.31 then becomes:

$$\begin{aligned} f(\theta) &= \sum_{r=1}^n \ln \left( \frac{z_{0e(n+1-r)}}{z_{0e(n-r)}} \right) \sin(2r-1)\theta \\ &= \ln \left( \frac{z_{0e3}}{z_{0e2}} \right) \sin \theta + \ln \left( \frac{z_{0e2}}{z_{0e1}} \right) \sin 3\theta + \ln \left( \frac{z_{0e1}}{z_0} \right) \sin 5\theta, \end{aligned} \quad (3.38)$$

where  $z_0 = 1 \Omega$ .

Equation 3.30 can now be written as shown in equation 3.39.

$$f(\theta) = 0.383 \frac{4}{\pi} \left[ w_1 \sin \theta + w_2 \frac{\sin 3\theta}{3} + w_3 \frac{\sin 5\theta}{5} \right] \quad (3.39)$$

The weighting functions are calculated from comparing term by term equations 3.38 and 3.39.

$$\begin{aligned} w_1 &= \frac{\pi}{4k} \ln \left( \frac{z_{0e3}}{z_{0e2}} \right) = 1.003 \\ w_2 &= \frac{3\pi}{4k} \ln \left( \frac{z_{0e2}}{z_{0e1}} \right) = 0.6577 \\ w_3 &= \frac{5\pi}{4k} \ln \left( \frac{z_{0e1}}{z_0} \right) = 0.2571 \end{aligned} \quad (3.40)$$

The even-mode impedances for each of the five sections and the required weighting functions are summarised in table 3.1.

The order of this divider is  $n = \frac{N+1}{2} = \frac{5+1}{2} = 3$ . The total electrical length of the coupler is given by [26, eqn 7.34 ]:

$$\theta = n\pi = 3\pi, \quad (3.41)$$

which is a quarter wavelength longer than a multisection coupler of 5 sections. Such a coupler will be  $5 \times 90^\circ = 2.5\pi$  long. The reason for this difference is that the synthesis

**Table 3.1:** Required Even-Mode Impedances and Weighting Functions for  $-8.34$  dB Coupler

Section ( $i$ )	$z_{0e(n)}$	$w_i$
1	1.02538	1.0003
2	1.14102	0.6577
3	1.85802	0.2571
4	1.14102	0.6577
5	1.02538	1.0003

for the non-uniform coupler is for an equal-ripple response in the range  $2\beta = 0$  to  $2\beta = 1$ , where the value of  $\beta$  at the centre frequency is  $1/4$  and the ( $u$ -axis) length of the coupler corresponds to those of  $2n$  lobes and is therefore  $4n\pi$  or  $12\pi$ , such that the total electrical length is  $\theta = \frac{1}{4}4n\pi = n\pi$ .

$Z_{0e}(u)$  can now be evaluated by solving the integral of equation 3.29.

For example, it was decided to divide the coupler into 41 discrete sections. (Graphically illustrated in Figure 3.9.) Each discrete section has an electrical length of  $13.17^\circ$ .

$$\phi = \frac{\theta}{41} = \frac{3\pi}{41} = 13.17^\circ. \quad (3.42)$$

$Z_{0e}(u)$  has to be evaluated at these 41 discrete points. If the discrete point is at  $u = -\pi$ , the integral is solved as follows (Refer to Figure 3.8):

$$\begin{aligned} \frac{1}{2} \ln \left( \frac{Z_{0e}|_{u=-\pi}}{Z_0} \right) &= -\frac{k}{\pi} \left[ w_3 \int_{-6\pi}^{-4\pi} \frac{\sin^2(u/2)}{u/2} du \right. \\ &\quad \left. + w_2 \int_{-4\pi}^{-2\pi} \frac{\sin^2(u/2)}{u/2} du + w_1 \int_{-2\pi}^{-\pi} \frac{\sin^2(u/2)}{u/2} du \right] \end{aligned} \quad (3.43)$$

A summation of integrals is thus required for each of the 41 sections that need to be evaluated. This equation can be numerically solved in a mathematical software package such as Matlab.

$Z_{oe}(z)$  can be found from  $Z_{0e}(u)$  using the relationship in equation 3.21.  $Z_{oo}(z)$  can be obtained from  $Z_{oe}(z)$  using the coupling requirement in equation 3.18.

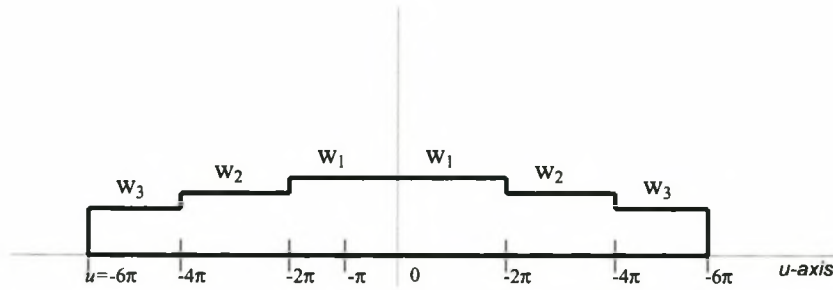


**Figure 3.8:** Location of weighting functions for use in solving the integral in equation 3.29.

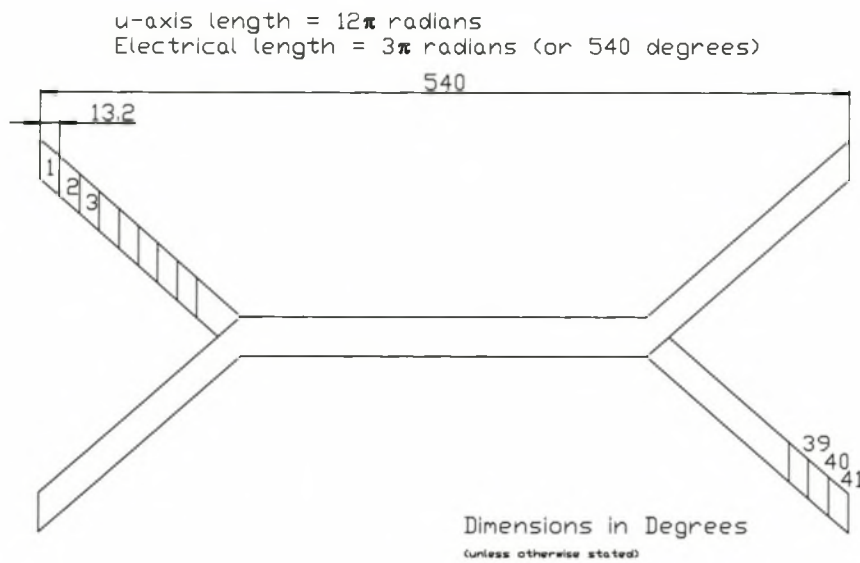


**Figure 3.9:** Illustration of Division of a Coupler into 41 Sections

The required even and odd mode impedances ( $Z_{0e}(z)$  and  $Z_{0o}(z)$ ) for the first 21 sections, are shown in table 3.2. The structure is symmetrical and sections 22 to 41 have the same impedances as sections 20 to 1.

**Table 3.2:** Required Even and Odd Mode Impedances for Discretised  $-8.34$  dB Coupler

<i>Section</i>	$Z_{0e}$	$Z_{0o}$
1	50.0200	49.9801
2	50.1469	49.8535
3	50.4204	49.5831
4	50.7768	49.2350
5	51.0863	48.9368
6	51.2477	48.7827
7	51.2758	48.7559
8	51.3559	48.6799
9	51.8794	48.1887
10	53.0559	47.1201
11	54.6742	45.7254
12	56.1686	44.5089
13	56.9980	43.8612
14	57.1504	43.7442
15	57.4388	43.5246
16	59.5125	42.0080
17	64.9794	38.4737
18	74.5893	33.5169
19	87.1925	28.6722
20	98.7397	25.3191
21	103.5416	24.1449

### 3.5 Implementing the Coupler

The even and odd-mode impedances can be implemented in Microwave Office<sup>®</sup> using ideal coupled transmission line components. The advantage of this step is twofold; the ideal design can be verified easily and the ideal properties can be used for optimisation goals.

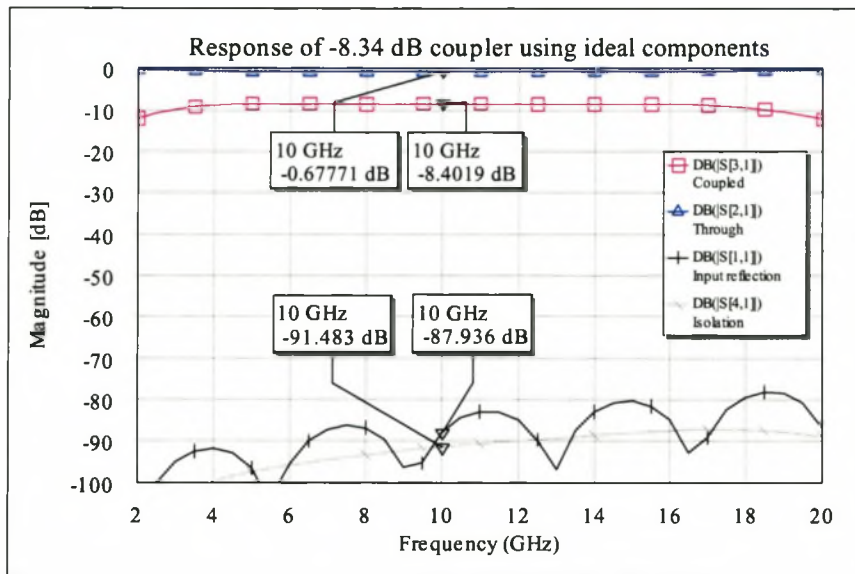


**Figure 3.10:** Response of a  $-8.34$  dB Coupler Using Ideal Components. (Computed using MWO)

Figure 3.10 shows the response of one of the cascaded  $-8.34$  dB couplers using ideal (linear) components.

Translating the impedances into physical line dimensions can be done in various ways. Nomographs are available for very specific strip-line constructions [8]. Closed form expressions for the analysis and synthesis of broadside-coupled offset lines are available. [37]

Electromagnetic software development houses like AWR (developers of Microwave Office<sup>®</sup>) have developed linear models that are based on physical measurements of microwave structures, which can be optimised to obtain the required dimensions. AWR refer to these models as 'quasistatic models'.

### 3.5.1 Electromagnetic Analysis

The substrate chosen after optimisation of the models is Taconic TLY-5. The TLY-5 range has excellent frequency characteristics. Its dissipation factor ( $\tan \delta$ ) is 0.0009 at 10 GHz and its dielectric constant is specified to be almost constant in the frequency range 5–20 GHz.

The material properties of the Taconic dielectric used for implementation of the coupler are shown in table 3.3.

**Table 3.3:** Material Properties of Taconic TLY-5

<i>Parameter</i>	<i>Value</i>
centre Substrate thickness	0.127 mm
Top and bottom Substrate thickness	0.381 mm
Conductor height	18 $\mu\text{m}$
Dielectric Constant	2.2

The positioning of the layers are described in Figure 3.11.

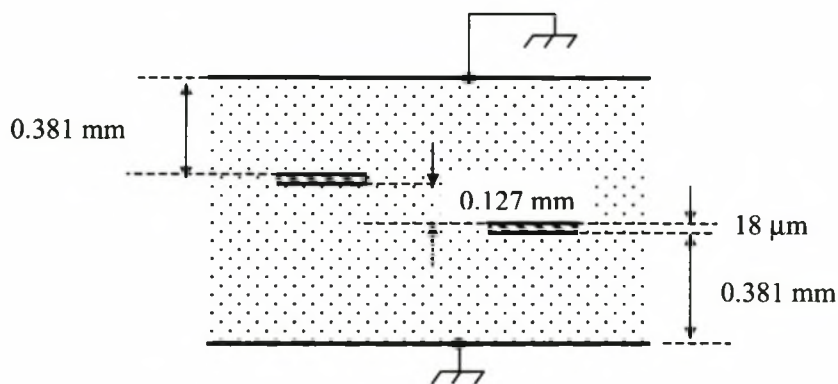


**Figure 3.11:** Positioning of the substrate layers of the broadside coupled stripline

The widths and offsets of the  $-8.34$  dB broadside coupler as obtained using the quasistatic models, are shown in Figure 3.12, where they are drawn as a function of the 41 sections. (The values are available in table form in appendix D.)

Implementing these dimensions resulted in the coupler shown in Figure 3.13. The individual sections are shown with the polygon that was used to smooth out the discontinuities.

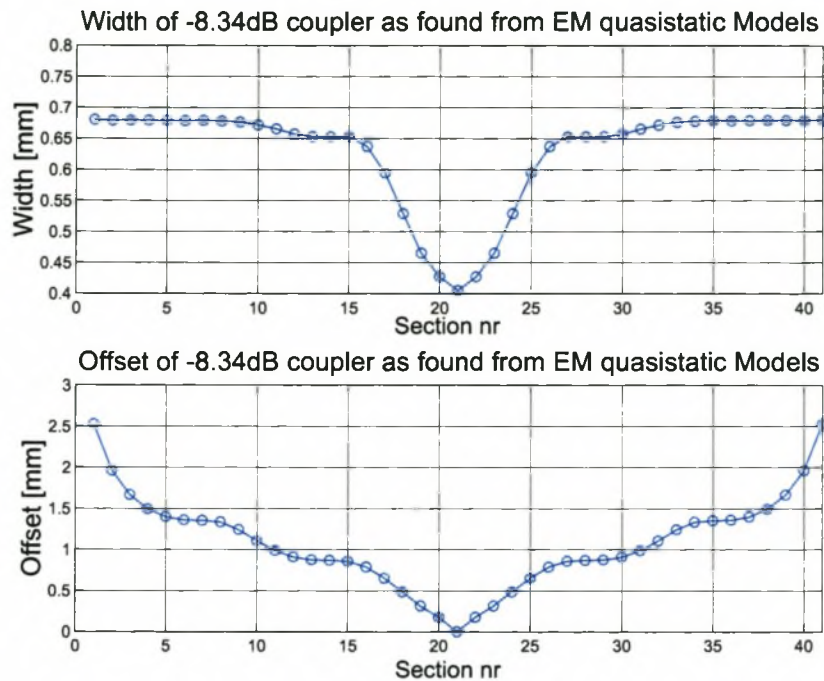


**Figure 3.12:** Widths and Offsets Required for the  $-8.34$  dB Coupler. (Computed using MWO)

The different colours imply that the tracks are on different layers.

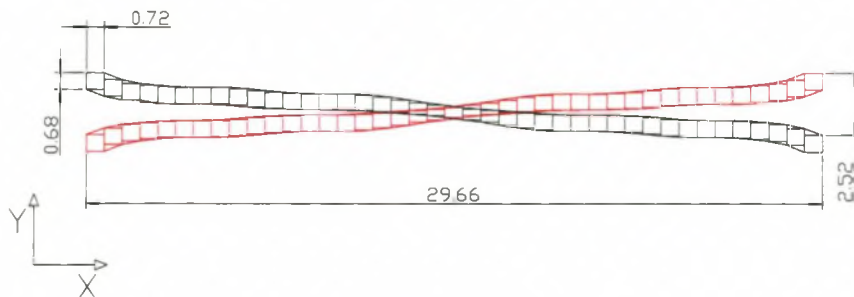


**Figure 3.13:** Completed  $-8.34$  dB Coupler

MWO's full wave EM Solver, EMsight, uses a modified spectral domain MOM (Method of moments) analysis for predominantly planar structures.

Due to the efficient planar nature of the MOM, three-dimensional modelling in the form of a vertical-directed current is difficult and limited. MWO does allow vertical-directed

currents to ensure electrical connections between different layers but these are approximations that are valid only for layers that are thin relative to a wavelength.

Planar currents on conductors (x and y dimensions) are spatially discretised using rooftop basis functions.

**Choosing Appropriate Grid Size** Most of the computational detail of the MOM is automatically taken care of by EMSight. The most important user-input is in the form of choosing the appropriate grid-size for meshing.

Three parameters affect the grid size for a structure. These are frequency, dimension and structure.

1. Frequency — A rule of thumb suggested by AWR, is to use a grid size that is at most  $0.01 \times$  the wavelength of the transmission media.
2. Dimension — Dimensions of lines and spaces in a structure are very critical. If a specified width is not a whole multiple of the grid, this dimension will be snapped to the grid, thereby introducing errors.

Knowledge of the manufacturing process will give insight into tolerances that can be allowed. If the manufacturing process cannot be more accurate than for example 10 mil, then cell size need not be smaller than 10 mil.

3. Structure — Complexity also affects the cell size definition. It is suggested that after a first run, a second run should always be done with a finer mesh.

The grid size along the x-axis was driven predominantly by the wavelength of the structure. Assuming a three layer stripline structure, the wavelength ( $\lambda$ ) at the highest frequency ( $f$ ) in the passband is calculated from:

$$\begin{aligned}
 \lambda &= \frac{c}{\sqrt{\epsilon_r} f} \\
 &= \frac{2.9979 \times 10^8}{\sqrt{2.2} \cdot 15 \times 10^9} \\
 &= 13 \text{ mm} \\
 \Rightarrow \text{maximum grid size} &= 0.13 \text{ mm}
 \end{aligned} \tag{3.44}$$

To keep the width (and therefore the calculation of the input reflection coefficient) as accurate as possible, the reflection introduced by snapping to the grid, should be as small as possible, preferably less than  $-25$  dB. This number was decided upon in order that the model be as accurate as possible, keeping limited resources in mind.

The characteristic impedance of stripline with a conductor placed in the centre, can be calculated from equation 3.45 [33, p156].

$$Z = \frac{30\pi}{\sqrt{\epsilon_r}} \frac{b}{w_e + 0.441b} \quad (3.45)$$

$w_e$  is the effective width of the centre conductor and  $b$  is the height of the stripline.

If  $\frac{w}{b} > 0.35$ , then  $w_e = w$  (the actual width of the line), otherwise,  $w_e = b(\frac{w}{b}) - (0.35 - \frac{w}{b})^2$ .

The reflection ( $\Gamma$ ) caused by a non-perfect width, can be calculated.

$$\Gamma = \frac{Z - Z_0}{Z + Z_0} \quad (3.46)$$

$Z_0$  is the ideal theoretical characteristic impedance of the line.

An error is introduced by snapping to a grid. The worst-case error (or reflection) occurs at the section of highest impedance as the line width is the smallest. The even mode impedance of this section is specified to be  $103 \Omega$  or approximately  $100 \Omega$ .

Using equation 3.45, the width necessary for a  $100 \Omega$  (centre) line is  $0.19$  mm. This theoretical value is different from the width obtained in the analysis because equation 3.45 assumes a centre conductor. As a worst case scenario, the width of a line can increase or decrease by one grid cell width when it is snapped to a grid. When the width is decreased by  $0.034$  mm (the chosen gridsize), the theoretical impedance decreases from  $100 \Omega$  to  $93.08 \Omega$  and the magnitude of a reflection coefficient (assuming a  $90$  degree line) will increase from zero to  $0.036$  or  $-28.9$  dB.

The  $50 \Omega$  line will be the least affected by a similar change in the width. Increasing the width by  $0.034$  mm, the theoretical impedance will increase from  $50 \Omega$  to  $51.55 \Omega$ . The reflection increases from  $0$  to  $0.0153$  or  $-36.3$  dB.

It is thus found that a grid size of  $0.034$  mm along the width (y-direction) will result in acceptable accuracy.

The maximum calculated grid sizes are:

- X-direction — 0.13 mm
- Y-direction — 0.034 mm

This specification resulted in 7438 elements, requiring 506 MB of RAM and was estimated to run for 57 hours by the package MWO.

Halving the number of X-directed elements reduced the requirements to 4721 elements, requiring 413.7 MB of memory. This could be done as the dimensioning along this axis is not as crucial as the widths of the lines. Reducing the grid size further would compromise the results.

In further analyses, the details of the grid will not be discussed. It has to be noted though that due to the physical size of the full cascaded coupler (which includes two  $-8.34$  dB couplers, interconnecting lines and connector transition strips), accurate gridding was not possible and it is expected that simulations of larger structures will not be accurate. MWO does have the feature of breaking up the EM circuit into smaller sections and modelling it as smaller sections that can be linearly connected. This greatly reduces the demands on resources, but interactions between these sections are replaced with ideal interactions; ports are perfect and coupling between tracks in different sections are assumed zero. Predicted values are thus over-optimistic.

The full-wave EM response is shown in Figure 3.14. Note in this figure that the magnitude axis is different from the figure showing the ideal response (Figure 3.10). It is found that  $|S_{11}|$  degrades from better than  $-80$  dB in the whole passband of the ideal (linear) model, to better than  $-20$  dB in the full wave analysis.

The results in Figure 3.14 show the expected results of one of the  $-8.34$  dB couplers and exclude effects from interconnecting 50 Ohm lines and effects from cascading two  $-8.34$  dB couplers. Even though the results seen in this figure are excellent, it is necessary to include the above mentioned effects before its usefulness as a 3 dB coupler can be discussed.

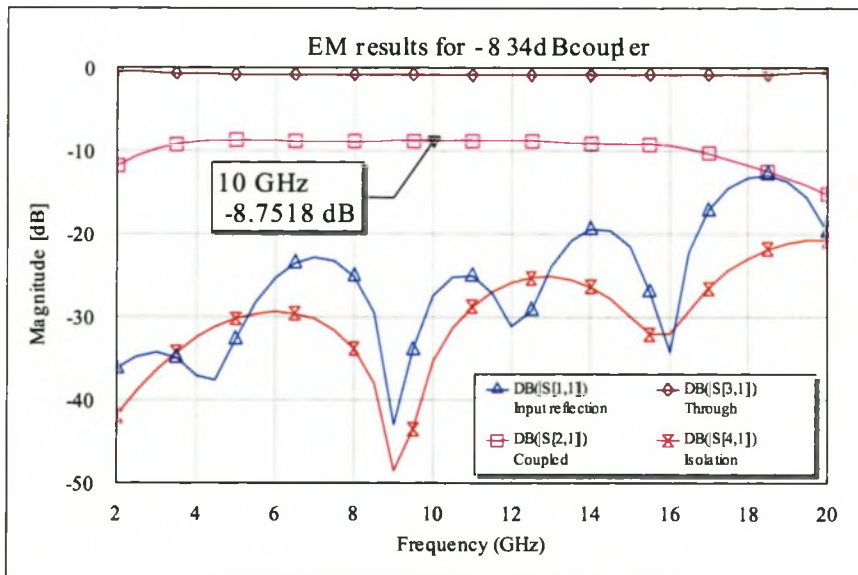


**Figure 3.14:** Electromagnetic Simulation of the Completed  $-8.34$  dB Directional Coupler. (Computed using MWO)

### 3.5.2 Implementation Issues

A very important aspect of microwave design is the physical construction of the microwave device. The reason being that the geometrical discontinuities affect the performance of the device by introducing unwanted reactance into the system. Parasitic capacitance and inductance have a pronounced effect at microwave frequencies. This section will serve to discuss two implementation issues encountered for the coupler. These issues are right-angled bends and connector transitions.

**Bends** Howe [20, pp48-50] investigated right-angled bends. Two methods were investigated, namely using curved angles and using mitered angles. He found that the reflection from curves with a radius of three times the width of the line was almost indistinguishable from the reflection of a straight line and resulted in a better frequency response than using mitered angles. More will be said about mitered angles in section 4.3.

A right-angled bend for a  $50\ \Omega$  line used in the coupler, is shown in Figure 3.15, where an extra section was added to make the electrical length of the line equal to  $90^\circ$ .

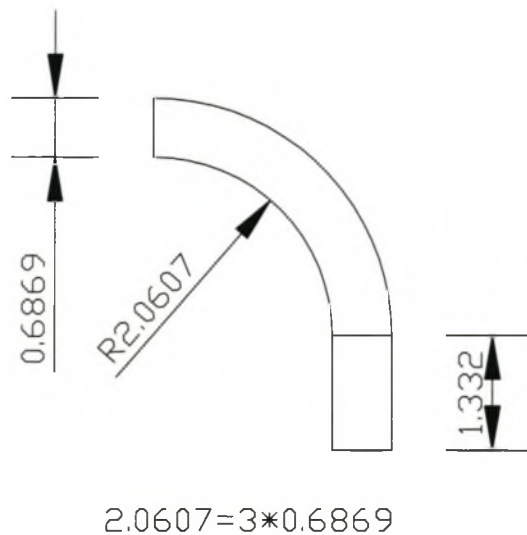


**Figure 3.15:**  $90^\circ$  Turn with Radius equals to  $3 \times$  the Width of Line. The Electrical Length is  $90^\circ$ . (Dimensions in mm)

**Coaxial to Microstrip Transition** The transition between the  $50\ \Omega$  connector and the  $50\ \Omega$  stripline introduced unwanted reactances into the system due to the geometric discontinuities involved. The geometric discontinuities caused higher order modes to be excited at the planes of abrupt changes in geometry. Schematically, the reactance is represented in Figure 3.16.

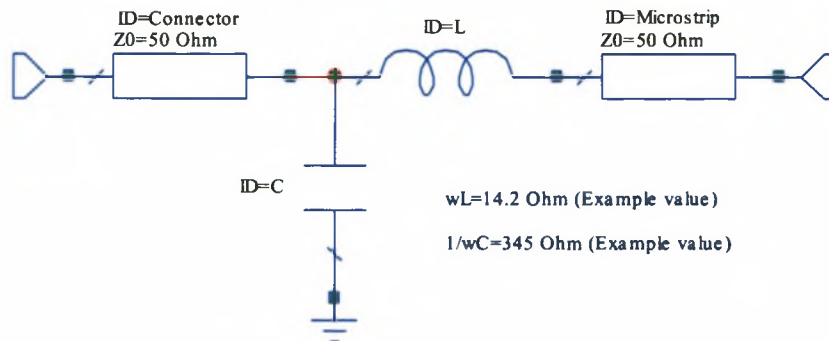


**Figure 3.16:** Schematic Representation of Discontinuities in Transition from Coaxial Connector to Microstrip (Stripline)

Empirical equations are available to approximate the capacitance and inductance introduced by the junction ([2] [42]).

As an example, Wight *et al* in [42] experimentally found the series reactance of an SMA connector connected to a microstrip line at 10 GHz as:

Substrate	Launcher	$\omega L[\Omega]$	$\omega C[mMho]$	
$\epsilon_r = 2.3$	$h = 10mil$	14.2	2.9	(3.47)

where  $h$  is the diameter of the centre conductor of the coaxial connector. These values are indicated in Figure 3.16.

It was found that the series inductance contributes a significant excess phase component.

To compensate for the added reactance, a stripline transition section was designed using Microwave Studio. The built-in optimiser was used to find the best transition dimensions.

The optimised transition is shown in Figure 3.17 and the calculated  $S_{11}$  is shown in Figure 3.18. Note that the transition section is microstrip and not stripline as the rest of the coupler.

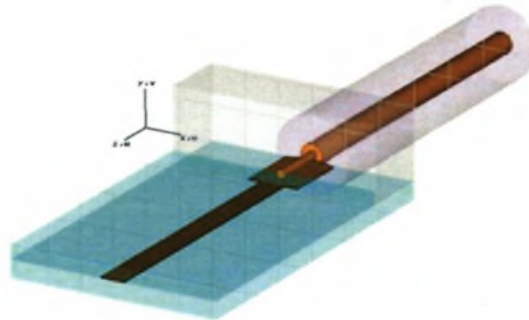


**Figure 3.17:** Perspective View of the Transition between Coaxial Connector and Stripline to achieve a Transition of better than  $-20$  dB over the Pass-band. (Computed using CST)

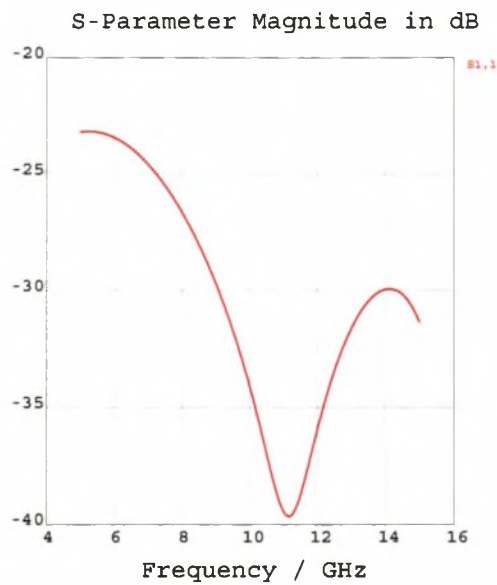


**Figure 3.18:**  $S_{11}$  of the Transition between Connector and Stripline Coupler. (Computed using CST)

### 3.5.3 TE and TM Modes

The cascaded coupler will be housed in a metal box. As such, certain modes will exist.

An approximation of the modes and associated cutoff frequencies (below 13.8 GHz) that can be excited in the waveguide are summarised in table 3.4.

**Table 3.4:** Approximate Cutoff Frequencies and Modes in the Low Frequency Coupler

<i>Mode</i>	<i>m</i>	<i>n</i>	$f_{c_{mn}}$ (GHz)
TE	1	0	4.4
TE	2	0	8.8
TE	3	0	13.2

These frequencies were calculated using standard rectangular waveguide equations [31, pp 123-126]. These equations assume a homogeneous dielectric layer inside a waveguide and exclude the effects of any transmission lines inside such a waveguide. Although the cut-off frequencies and modes will be affected by the transmission lines, the equations do give a fairly accurate estimation of the modes.

As simulation of the complete tandem coupler is not possible, these will not necessarily be seen in the EM analysis, but should be observed in the physical coupler. If the dimensions of the subcircuits are such that the higher order modes can exist, the modes will be present if they are excited.

## 3.6 Results: Low Frequency Coupler

### 3.6.1 EM Results

The layout of the final coupler is shown in Figure 3.19. The four microstrip transition sections are shown at the four ends of the coupler.

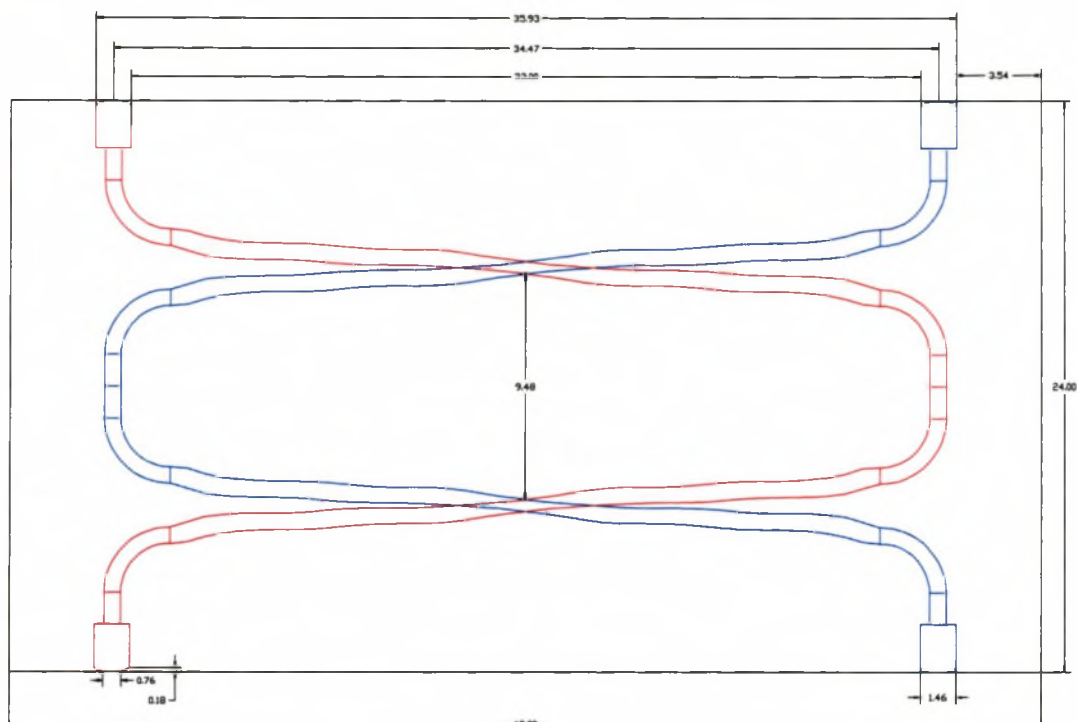


**Figure 3.19:** Layout of the Low Frequency Coupler. Dimensions in mm.

Casing screws were added to the completed coupler. The necessity for these screws was three-fold; it suppressed higher order modes; it ensured an even pressure on the dielectrics, thereby increasing consistency in the dielectric and lastly it ensured an even connection with the ground plane. Screws that are located 2–3 line-widths away from a conductor, should not affect the coupling significantly.

The EM designs in all subsequent chapters were done using Microwave Office Version 5.01 (or MWO for short). Selected results were verified using CST’s Microwave Studio Version 3.0. These are referenced as ‘CST’. CST uses the Finite Integral Time Domain method

for its EM simulations. This method is in many ways similar to FDTD.

The result from the EM analysis is shown in Figure 3.20. This result is a linear combination of individual EM results obtained for the  $-8.34$  dB coupler and the  $90^\circ$  connecting circuits.

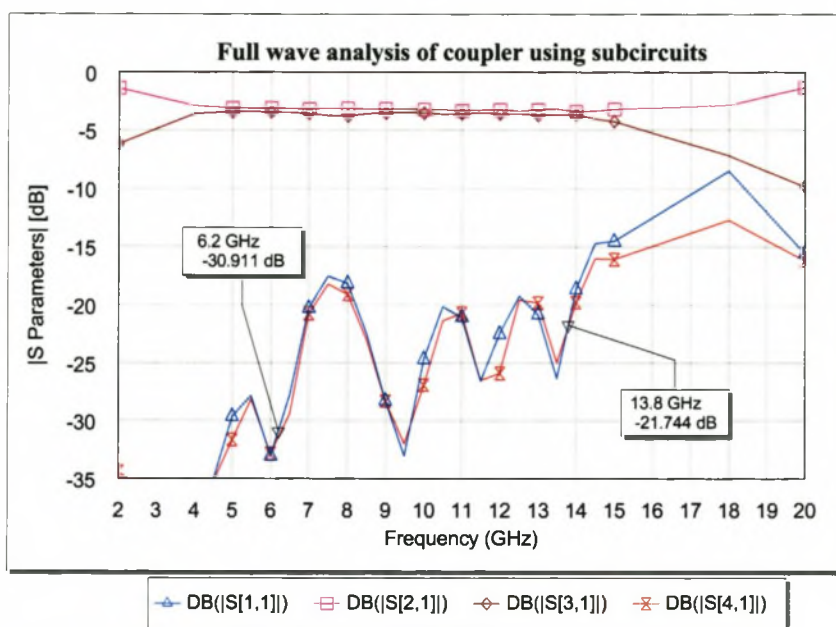


**Figure 3.20:** Calculated S-Parameters of Low Frequency Coupler. (Computed using MWO)

The maximum reflection in the passband is calculated as approximately  $-17$  dB. (Passband is indicated with markers in Figure 3.20.) Power division is achieved at approximately  $-3.3$  dB. The biggest difference in power division is at approximately 8 GHz, where the difference is approximately 0.67 dB. (Refer to Figure 3.21).

A (physically) measured reflection coefficient of  $-17$  dB is excellent. However, it has to be kept in mind that the (analysed) response shown in Figure 3.20 assumes perfect loads and as such the performance of the physical device is expected to degrade. A measured  $|S_{11}|$  of  $-10$  dB is considered acceptable.

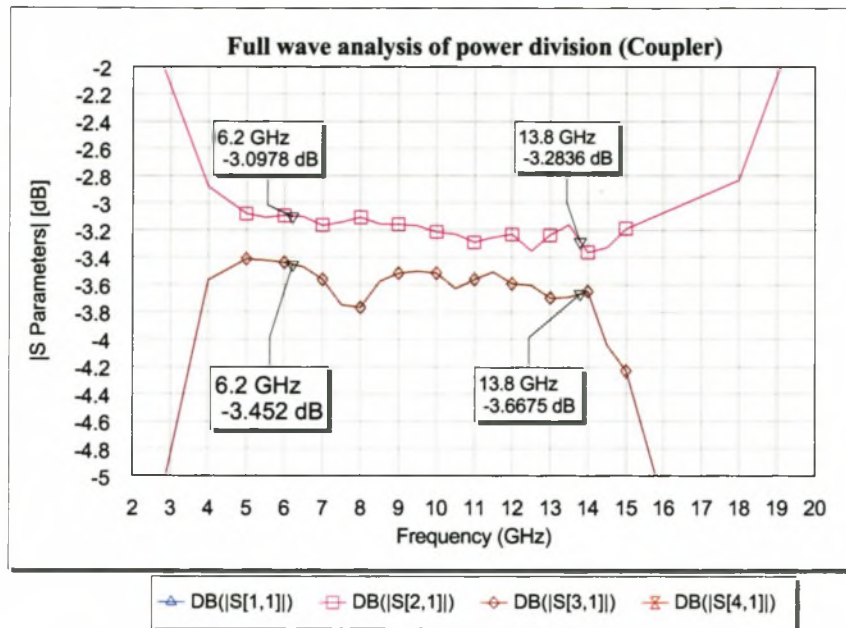


**Figure 3.21:** Calculated Power Division Results of Low Frequency Coupler. Zoomed view of Figure 3.20. (Computed using MWO)

### 3.6.2 Measurement and Final Results

**Calibration** The final measurement was made on an 8510C Agilent Technologies Network Analyser. The calibration was done with an HP85052D 3.5 mm calibration kit.

Calibration is necessary as the accuracy of network measurements is greatly influenced by external factors such as the measurement set-up and interconnecting cables. Errors that are repeatable or that can be predicted are called ‘systematic’ errors and these errors can be removed to a large extent from the measurement through calibration [1].

A full two-port calibration was done as this is the most complete calibration procedure for measurement of transmission and reflection characteristics of 2-port devices.

The frequency band over which the calibration was done, was between 5 and 15 GHz. An averaging factor of 64 was selected. Averaging improves the accuracy and resolution of the measurement by reducing the effect of random noise and other time variant errors.

The reflection obtained after calibration was below  $-50$  dB over the total bandwidth and the phase error obtained for transmission was less than  $1^\circ$ .

**Measurement** Measurement of the coupler required addition of gender change adapters on the ports under test. The other two ports were terminated with  $50\ \Omega$  loads. The adapters will introduce phase errors. It is possible to correct for these errors. Similarly, the loads are not ideal and their influences were investigated.

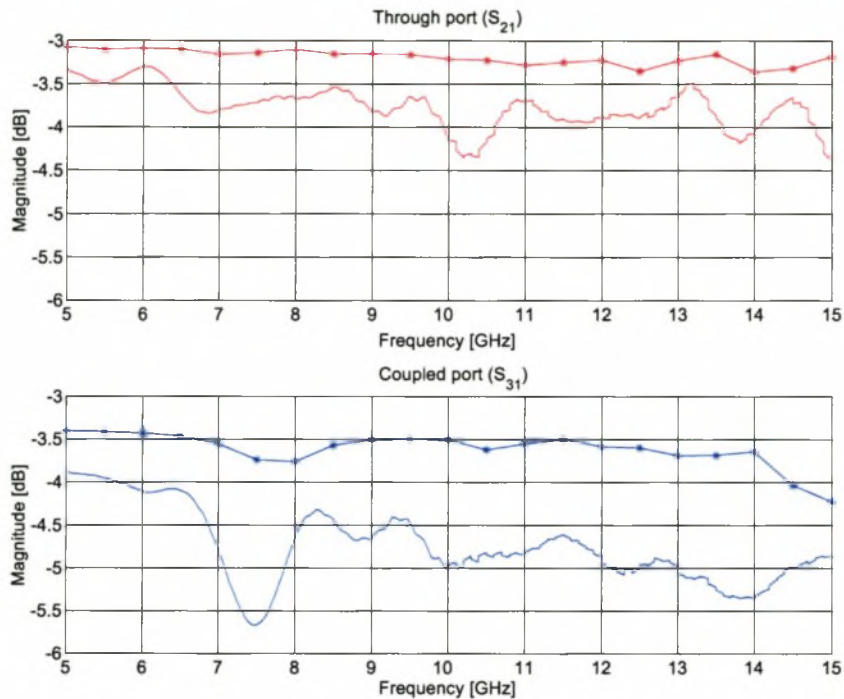


**Figure 3.22:** Measured and Predicted Coupling of Low Frequency Coupler. (Measured and computed using MWO)

The measurement results are shown in Figure 3.22 and Figure 3.23. In these figures, the solid lines with the markers indicate the results computed with MWO and the solid lines with no marker, indicate the measured results.

The measured average power division at port two ( $S_{21}$ ), is  $-3.8$  dB, with a maximum deviation of  $1.079$  dB (or  $\pm 0.54$  dB).

The measured average power division at port three ( $S_{31}$ ) is  $-4.8$  dB with a maximum deviation of  $1.8$  dB ( $\pm 0.9$  dB). In the bandwidth  $8$ – $13.8$  GHz, this deviation is  $1.03$  dB.

The measured  $S_{31}$  (coupled port) is noticeably different from the calculated values. The general trend of the plot of the measured and calculated graphs is the same, with a trough expected at  $7.5$ – $8.0$  GHz. The trough is at a slightly lower frequency in the measured

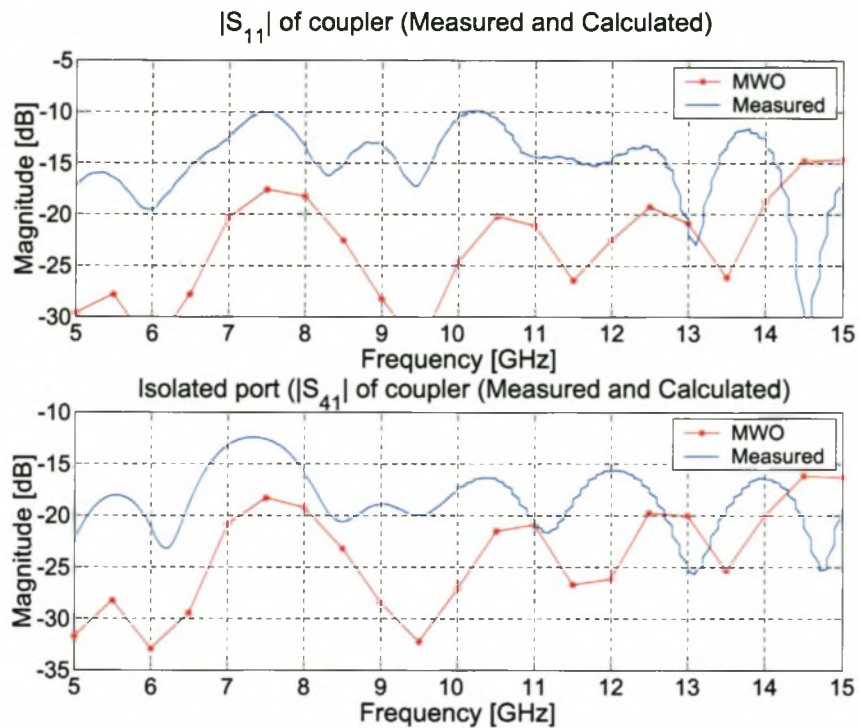


**Figure 3.23:** Measured and Predicted Input Reflection and Isolation. (Measured and computed using MWO)

results, indicating a permittivity slightly different from the specified 2.2. The significant offset between calculated and measured values could indicate a higher substrate loss than specified.

The shape of the graphs for input reflection and isolation, have the same general shape, but not the same value. The slight deviation in frequency, caused by a slightly different dielectric constant is once again observed.

A further analysis on the EM model, revealed that doubling the specified loss tangent and changing the dielectric constant ( $\pm 20\%$ ) did not affect the performance of the coupler greatly. Changing the dielectric constant did move the passband of the coupler as expected.

The other parameters that were investigated to find an explanation for the discrepancy between measured and calculated values are itemised below:

- The thickness of the substrates was measured to be 0.17 mm. This includes two

copper tracks of specified thickness of approximately 0.018 mm. This indicates that the substrate could be 0.134 mm thick as opposed to the specified 0.127 mm. In simulation this difference did not significantly affect the results.

- The terminating and source impedances are not ideal. The effect of non-ideal source/termination impedances greatly affected the results. The non-ideal impedances could be as a result of incorrectly designed transition sections.
- The insertion of screws could have affected the effective material properties of the substrate. Their proximity to the lines may have influenced the circuit more than was intended. The only way to verify this, would be to remanufacture the coupler circuit and only insert screws that are more than three line-widths away from the conductors.

Figure 3.24 is an EM simulation showing the effect of changing the heights of the substrates to the measured heights. The brown and pink lines indicate that there is more than 1 dB difference between the voltage at the coupled port and the voltage at the through port. The grey lines (obtained with a Monte Carlo analysis) indicate the effect of a 10 % mismatch in the port impedances. The real part of the port impedance was given a statistically determined normal distribution and allowed a standard deviation of 10 %.

Note that the sharp trough at 8 GHz of the coupled port corresponds well with that measured at 7.5 GHz. (The difference in frequency is due to a different dielectric constant; also the MWO results are only plotted at multiples of 1 GHz.)

It is concluded that the deep trough measured at 7.5 GHz, is due to mismatches at the connectors; either by imperfect  $50 \Omega$  terminations or by the (by now slightly damaged) microstrip transitions between connector and circuit.

The effect on  $|S_{11}|$  is shown in Figure 3.25.

The S-Parameters of the terminations were measured. Figure 3.26 shows the reflection measured on the  $50 \Omega$  loads and shows the actual impedances of these loads. The terminations are quite accurate over the frequency range and is not the primary cause of port-impedance mismatches.

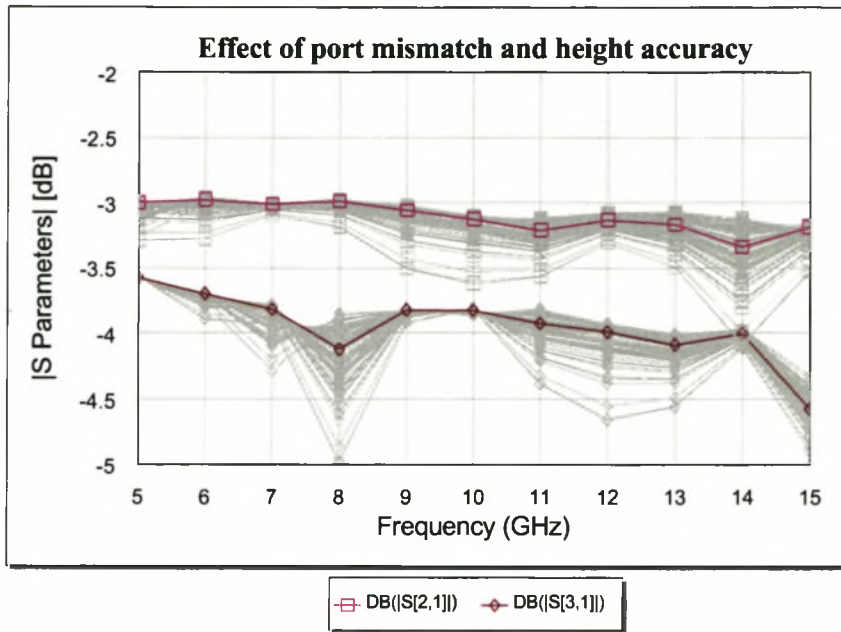


**Figure 3.24:** Effect of Actual Height of Substrate and Mismatch in Port Impedance on the Coupling of the Directional Coupler. (Computed using MWO)

**Removing the Effect of the Gender Changers on the Actual S-Parameters of the Coupler.** The S-Parameters of the coupler excluding the gender changers are determined from the Transmission (or T) parameters of the network.

The transmission (or T) parameters of a two port system are defined with reference to Figure 3.27.

$$\begin{aligned} b_2 &= T_{11}a_1 + T_{12}b_1 \\ a_2 &= T_{21}a_1 + T_{22}b_1 \end{aligned} \quad (3.48)$$

In equation 3.48, the T parameters can be written in terms of S-Parameters as shown in equation 3.49.

$$\begin{aligned} T_{11} &= S_{21} - \frac{S_{11}S_{22}}{S_{12}} & T_{12} &= \frac{S_{22}}{S_{12}} \\ T_{21} &= -\frac{S_{11}}{S_{12}} & T_{22} &= \frac{1}{S_{12}} \end{aligned} \quad (3.49)$$

When two of the ports of the coupler are under test, they are connected through two gender changers to the network analyser. The T parameters of three cascaded networks

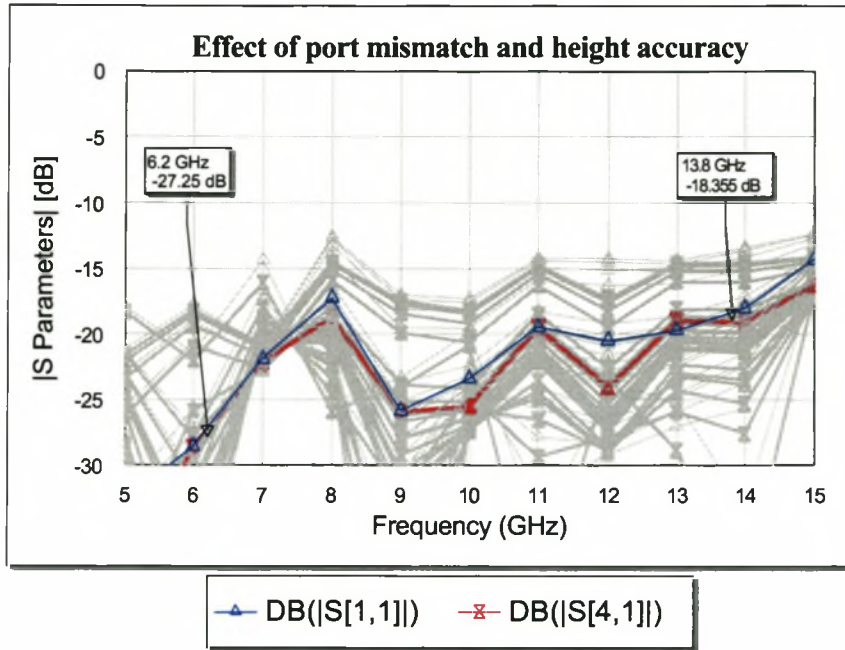


**Figure 3.25:** Effect of Actual Height of Substrate and Mismatch in Port Impedance on the Input Port Match of the Directional Coupler. (Computed using MWO)

are given in equation 3.50.

$$\begin{bmatrix} T_{11} & T_{12} \\ T_{21} & T_{22} \end{bmatrix} = \begin{bmatrix} (T_{11})_c & (T_{12})_c \\ (T_{21})_c & (T_{22})_c \end{bmatrix} \begin{bmatrix} (T_{11})_b & (T_{12})_b \\ (T_{21})_b & (T_{22})_b \end{bmatrix} \begin{bmatrix} (T_{11})_a & (T_{12})_a \\ (T_{21})_a & (T_{22})_a \end{bmatrix} \quad (3.50)$$

The ‘a’ subscript refers to the T parameters of the shorter gender changer. The short gender changer was connected to port 1 of the network analyser and as such was always considered to be at the ‘input’ side of the coupler. The ‘b’ subscript refers to the T parameters of the coupler and ‘c’ refers to the T parameters of the longer gender changer. The T parameters of the coupler can be found by multiplying the inverse of the T parameters of the gender changers with the measured T parameters of the whole system.

$$\begin{bmatrix} (T_{11})_b & (T_{12})_b \\ (T_{21})_b & (T_{22})_b \end{bmatrix} = \begin{bmatrix} (T_{11})_c & (T_{12})_c \\ (T_{21})_c & (T_{22})_c \end{bmatrix}^{-1} \begin{bmatrix} T_{11} & T_{12} \\ T_{21} & T_{22} \end{bmatrix} \begin{bmatrix} (T_{11})_a & (T_{12})_a \\ (T_{21})_a & (T_{22})_a \end{bmatrix}^{-1} \quad (3.51)$$

Implementation of equation 3.51 leads to the results depicted in Figure 3.28. Part (a) shows the improvement when the effect from the gender changers is eliminated. Part (b)

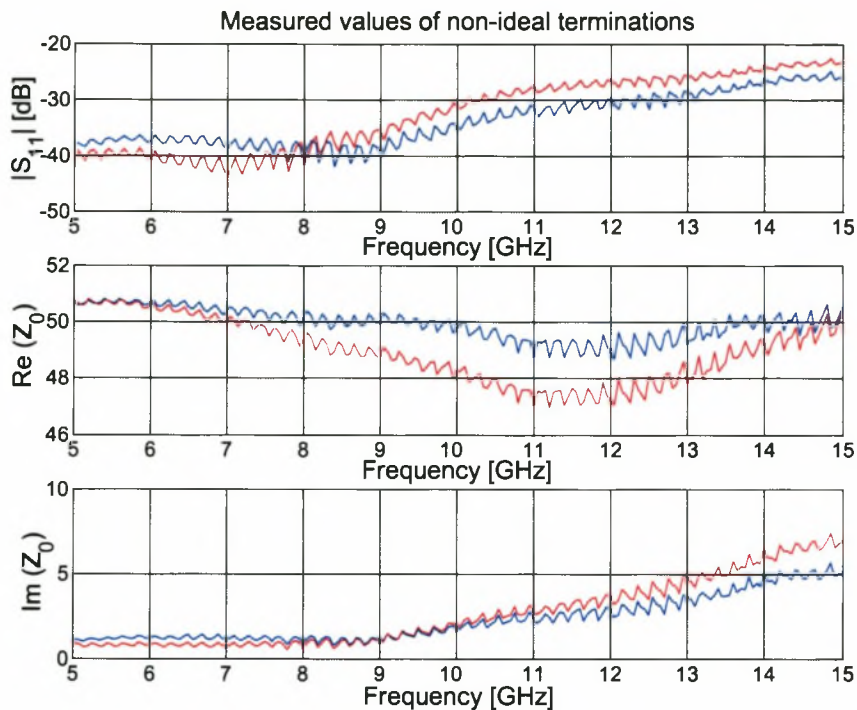


**Figure 3.26:** Measured  $|S_{11}|$  and Resultant Actual Impedances of Non-ideal  $50 \Omega$  Terminations used in all Measurements. (Computed using Measured)

is a plot of the difference between the measured and corrected results and shows that the gender changers introduce an error of more than  $\pm 0.3$  dB at higher frequencies. This effect was also observed at the ‘through’ port, since the same gender changers were used.

As a comparison, the coupler was analysed with CST as well. It was not possible to analyse the complete structure. Above a certain resolution, CST was not able to mesh the coupler successfully. This resolution was too low for accurate results.

Instead, one of the  $-8.34$  dB couplers was analysed to an accuracy of  $\lambda/200$ . (It was calculated that a resolution of  $\lambda/450$  is necessary for high accuracy.) The lack of availability of resources required (both in time and RAM), made it impossible to do an accuracy study on this result.

Figure 3.29 shows the result of cascading the  $-8.34$  dB coupler to obtain a  $-3$  dB coupler. Coupling levels are lower than calculated with MWO and the measured results. This could be due to the limited mesh accuracy.

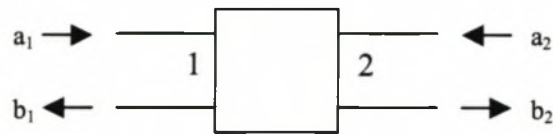


**Figure 3.27:** Definition of Incident and Reflected Waves for Determining T Parameters

### 3.7 A $-3$ dB Coupler with centre Frequency 29 GHz

A  $-3$  dB coupler, operating in the frequency band between 18 GHz and 40 GHz was designed.

As the bandwidth ratio is the same as that of the low frequency coupler, the theoretical design for the low frequency coupler was used for the high frequency coupler. Operating at a higher frequency meant that the coupled line sections had to be shorter. This had a non-linear influence on the coupling characteristics of the coupled-line sections. In implementing the specified even and odd mode impedances obtained in table 3.2, individual coupled line sections had to be optimised for the new centre frequency. This was done in exactly the same way as before and is therefore not discussed any further.

The completed high frequency coupler is shown in Figure 3.30. Note that the spacing between connectors is 11.84 mm. If this dimension is too small to fit connectors, more  $50 \Omega$  lines (arcs in the figure) can be added.

The arcs have electrical lengths of  $90^\circ$ . No optimisation was done on this design. It is strongly suggested that optimisation of the sections between the arcs and the  $-8.34$  dB couplers are done before implementation. An EM analysis package such as CST is ideal for EM optimisation. (MWO cannot optimise EM structures).

Figure 3.31 shows the coupling calculated with MWO. The maximum ripple is calculated to be 0.78 dB.

Some of the other S-Parameters are shown in Figure 3.32. Reflection and isolation is calculated to be better than  $-14.3$  dB in the passband.

The high frequency coupler will be discussed in more detail in chapter 6 where an FDTD

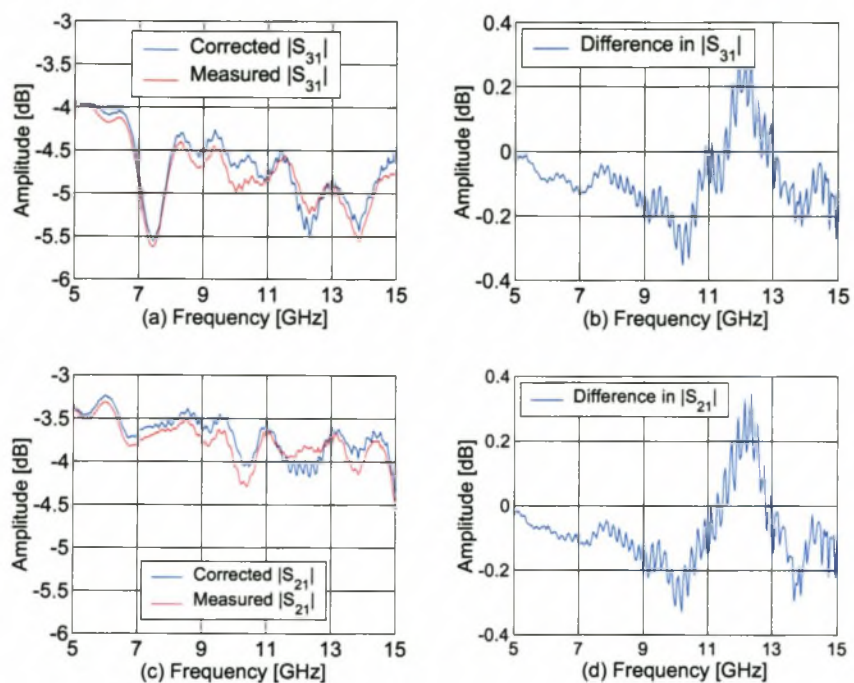


**Figure 3.28:** Effect of Gender Changers on Coupled ((a) and (b)) and Through port ((c) and (d)) of Directional Coupler. (Computed using Measured)

analysis will be done on the structure.

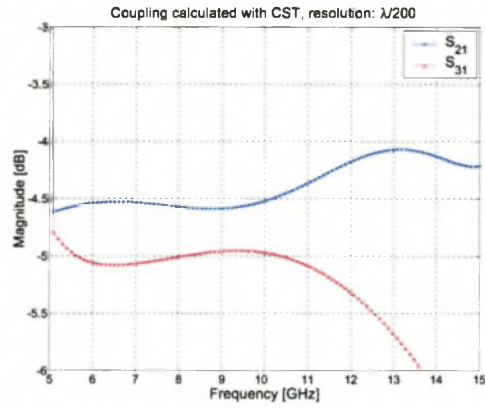


Figure 3.29: Simulated coupling of the low frequency divider (Computed using CST)

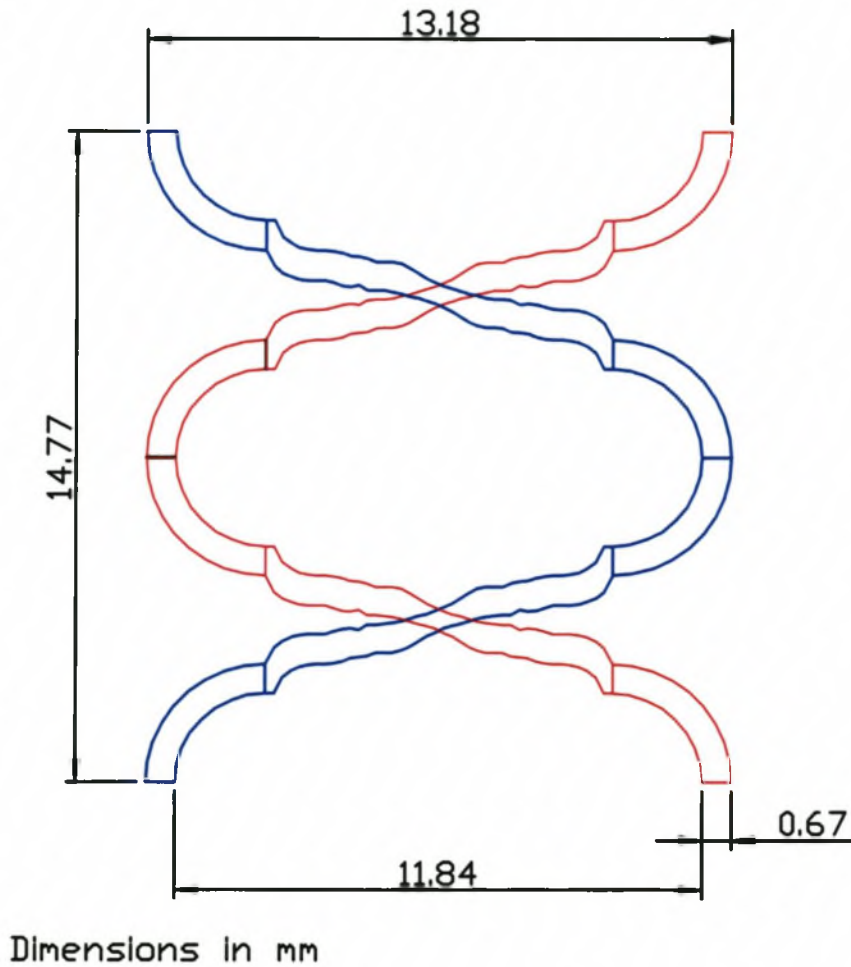
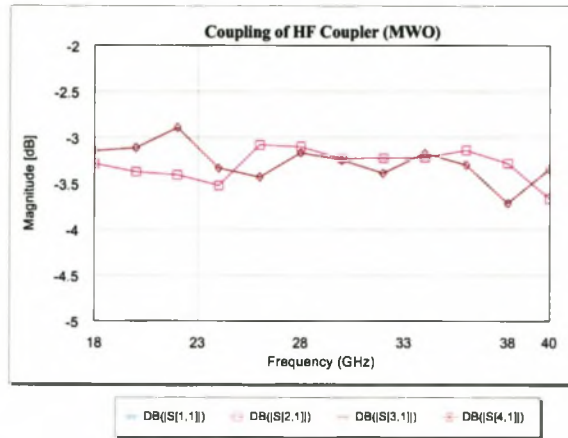
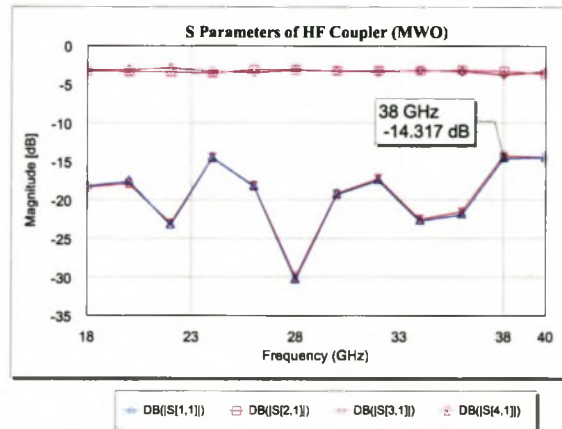


Figure 3.30: Layout of the High Frequency Coupler.



**Figure 3.31:** EM Analysis of HF Coupler Showing  $|S_{21}|$  and  $|S_{31}|$ . Results are a Linear Combination of EM Results and Subcircuits. (Computed using MWO)



**Figure 3.32:** EM Analysis of HF Coupler Showing  $|S_{11}|$ ,  $|S_{21}|$ ,  $|S_{31}|$  and  $|S_{41}|$ . Results Are a Linear Combination of EM Results and Subcircuits. (Computed using MWO)

## 3.8 Conclusion

This chapter introduced four port microwave couplers and showed the network analyses of these using the even and odd mode excitation method. The design of cascaded couplers was done using a method that finds an expression for the even mode impedance of coupled lines along the length of a coupler.

Details of the EM analysis of the coupler were given with specific reference to implementing such a coupler in MWO. The details of correct grid size were discussed and the effect of using too large a grid size was shown.

Physical implementation issues (related to the low frequency coupler) were discussed, after which the results obtained were presented.

The chapter ended with the design of an 18–40 GHz (high frequency) coupler, which was derived from the 6.2–13.8 GHz (low frequency) coupler.

The design of a cascaded coupler is intricate, resulting in an electrically large structure. The complex pattern of the coupler requires that the EM modelling of the structure has to be extremely accurate (on the order of  $\lambda/450$  or 30 micron). With limited resources, compromises had to be made. The device can be modelled using subcircuits, where high accuracy can be obtained for parts of the circuit. The linear combination of these subcircuits hide the non-ideal interplay between sections. If the accuracy is lowered, the complete model can be analysed, but the results may not be accurate.

The design is very sensitive to mismatches at the ports. Even though a design was done to minimise mismatches at the transition, the physical implementation of the transition sections proved to be difficult due to the different substrate layers of the coupler and the design of the box surrounding the coupler.

The low frequency coupler was housed in a metal box, consisting of a base and a lid. This implementation should be avoided as it makes it extremely hard to access the connector-transitions at the bottom. It is suggested that the box should have a removable floor, making it symmetrical along its length. It was also found that the non-symmetrical layout of the box caused more pressure to be exerted on the top connector pins, resulting in bent pins.

A second iteration, which incorporates a different box with screws moved further away from the conductors and new undamaged connectors, should have results significantly closer to the designed values.

The microwave design of this component is at a high enough standard to use in most microwave systems, but the implementation issues make it necessary to rethink the housing and connector transitions before using this component in such a system.

A picture of the completed low frequency directional coupler is shown in Figure 3.33.

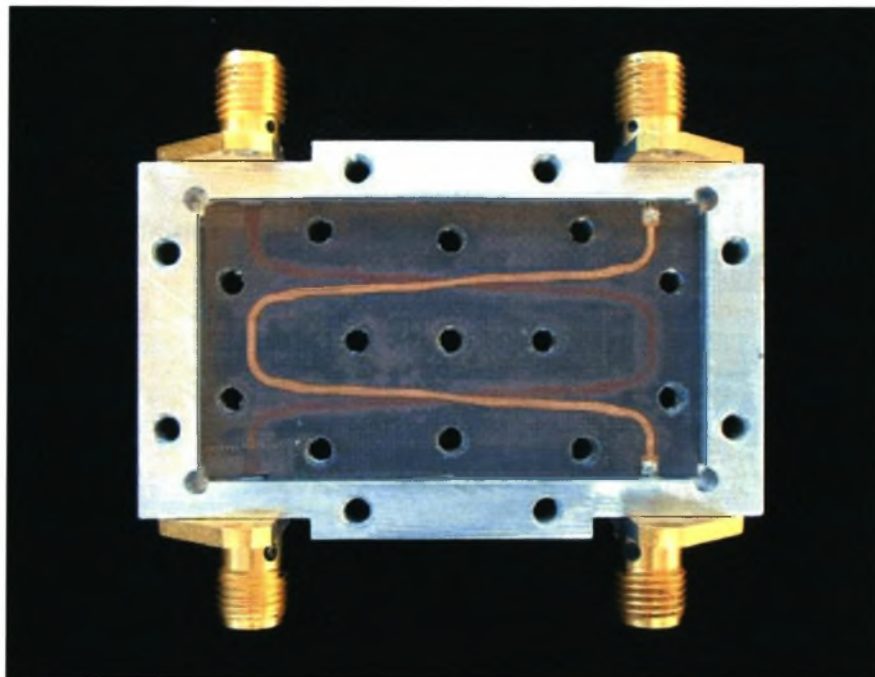


**Figure 3.33:** The Completed  $-3$  dB Coupler

## Chapter 4

# Design of a Wilkinson power divider with centre frequency 10 GHz

### 4.1 Introduction

Wilkinson power dividers have the advantage of having in-phase power-division at all frequencies. This makes them particularly suitable for use in broadband applications such as in feed systems of multi-element antennas.

Two-way Wilkinson dividers are three port networks. When terminated in matched loads, the ports of the Wilkinson divider are matched, the network is reciprocal and there is isolation between the output ports. Although Wilkinson dividers are considered to be lossy dividers, they are lossless when excited at the input port and when all the ports are perfectly matched. Due to the symmetry of the divider, no power is dissipated in the resistors when an equal amount of power is injected at the output ports (in which case it functions as a combiner rather than a divider). All other reflected power (or power purposefully injected at the output ports) is dissipated by the resistors.

The design of Wilkinson power dividers have been done by various authors. Lim *et al* [24] successfully implemented a 4:1 unequal Wilkinson power divider using a defected ground structure (DGS). The DGS on the ground plane provides an additional effective inductive component to the microstrip line. This makes it possible to realise microstrip lines of

very high impedances (above  $150 \Omega$ ), which is typically difficult, as a very thin conductor is required. Scardelletti *et al* [35] capacitively loaded the quarter wave Wilkinson divider transmission lines in order to obtain a reduction in size in the dividers.

Cohn [11], developed design equations and tabulated line impedance values and resistor values necessary for N-port Wilkinson dividers up to a maximum of 1000 % bandwidth. Using these tables simplifies a design as the process to obtain the resistor values is typically iterative in nature.

## 4.2 Analysis

The matched property of the Wilkinson divider implies that  $S_{11} = S_{22} = S_{33} = 0$ . Due to reciprocity,  $S_{ij} = S_{ji}$ . The isolated property implies that  $S_{23} = S_{32} = 0$ . The final S-parameters are obtained from knowledge that all the power entering through port 1 should pass through port 2 and 3 and should be equal. This means  $|S_{12}|^2 + |S_{13}|^2 = 1$ . Therefore,  $|S_{12}| = |S_{13}| = 0.707$ . Indeed, the S-parameters of an ideal single section Wilkinson divider can be summarised as [31, p365]:

$$\begin{bmatrix} 0 & -0.707i & -0.707i \\ -0.707i & 0 & 0 \\ -0.707i & 0 & 0 \end{bmatrix} \quad (4.1)$$

The bandwidth of the standard divider can be increased by adding more  $90^\circ$  lines to the standard design.

The iterative design followed by Cohn is based on a synthesis of the standard Wilkinson configuration using even and odd mode excitations. The even and odd mode bisections of a three section Wilkinson divider are shown in Figure 4.1. (The unbisected Wilkinson schematic is shown in Figure 4.2.) The magnetic wall in Figure 4.1 refers to the fact that when the divider is excited in the even mode (by adding voltages of equal size and phase to ports 2 and 3), an open circuit (magnetic wall) can be placed as shown without affecting the S-Parameters seen at port 2 (or port 3). For odd mode, the symmetry wall is a short circuit (electric wall), which effectively places a short circuit between the two bisections.

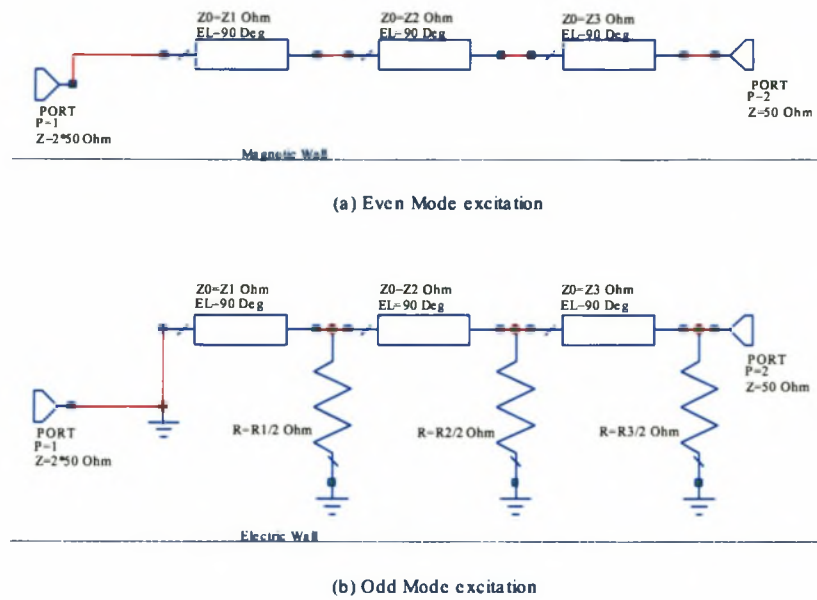


**Figure 4.1:** (a) Even Mode and (b) Odd Mode Bisections of Wilkinson Divider

The characteristic impedances of the lines are obtained from noticing that the even-mode circuit of Figure 4.1 is a stepped transformer between 50 and 100  $\Omega$ .  $|S_{11}| = |S_{11e}|$  will have optimum equal ripple behavior if the characteristic admittances of the 90° transmission line sections yield optimum stepped-transformer response. This information is available in the form of tables and equations [10].

In determining the resistor values, it will be necessary to compute these resistances such that the isolation ( $S_{23}$ ) and matching ( $S_{22}$  and  $S_{33}$ ) are optimum. Cohn found that it is much easier to design for an optimum  $S_{11}$  and showed that when  $S_{11}$  is optimum, the matching at the other two ports are close to optimum. Refer to [11] for more details on the iterative design of such a divider.

The values given in Cohn's article were used in this thesis. The bandwidth specification of between 18 and 40 GHz, gives a factor of  $\frac{f_2}{f_1} = \frac{40}{18} = 2.22$ . (The divider will be implemented with a bandwidth ratio of 2.22, but at a centre frequency of 10 GHz. Theoretically, the design can be scaled to work at the higher frequency.)

The bandwidth ratio of 2.22 requires an  $N = 3$  section divider, with the following

impedances:

$$\begin{aligned}
 Z_1 &= 1.150 \cdot 50 = 57.5 \, \Omega \\
 Z_2 &= 1.414 \cdot 50 = 70.7 \, \Omega \\
 Z_3 &= 1.740 \cdot 50 = 86.0 \, \Omega \\
 R_1 &= 8 \cdot 50 = 400 \, \Omega \\
 R_2 &= 4.229 \cdot 50 = 211.5 \, \Omega \\
 R_3 &= 2.144 \cdot 50 = 107.2 \, \Omega
 \end{aligned} \tag{4.2}$$

Figure 4.2 is a schematic representation of the final divider. It will be shown that these values result in a theoretically ideal divider.

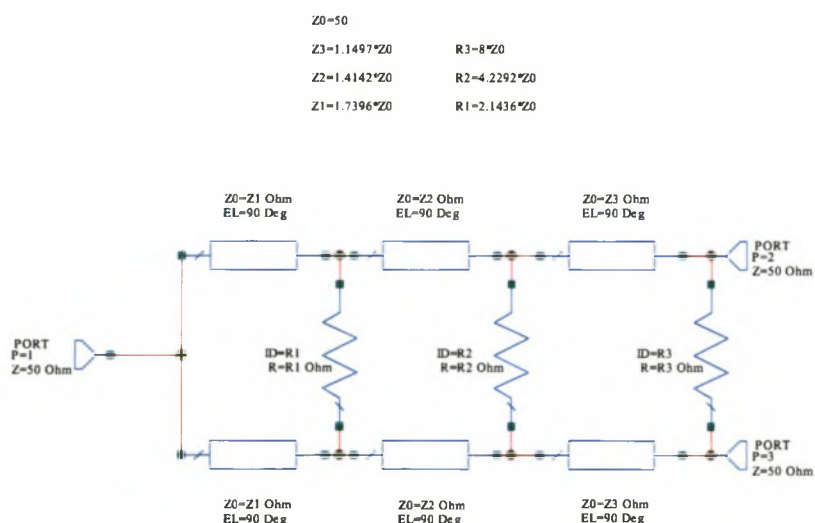


Figure 4.2: Wilkinson Divider with  $N=3$

### 4.2.1 Finding the S-Parameters of a Wilkinson Divider using impedances suggested by Cohn [11]

Referring to Figure 4.1, it is found that when the circuit is excited in the even mode, a magnetic wall can be placed as a symmetry line, resulting in an open circuit, which effectively removes the resistors from the circuit.

For odd mode excitation, the symmetry line is replaced with an electrical wall (effectively

short circuiting the resistors) and it is possible to analyse the circuit by looking at one half of the circuit.

**Port Reflection Coefficients ( $S_{11}$ ,  $S_{22}$  and  $S_{33}$ )** The three port reflection coefficients are calculated from Figure 4.2. This is done by finding the input impedance as seen at each port while the other ports are terminated in  $50 \Omega$  loads. Due to the 90 degree electrical length of the transmission lines, load impedances are easily transferred into input impedances through the relation  $Z_{in} = \frac{Z_0^2}{Z_L}$ , where  $Z_0$  is the characteristic impedance of the line and  $Z_L$  is the load impedance.

This property of a 90 degree line and some basic circuit analysis, shows that all the input impedances are matched. (Refer to appendix A for the full derivation)

$$Z_{in}^1 = 50.00 \quad (4.3)$$

$$Z_{in}^2 = 50.00 \quad (4.4)$$

$$Z_{in}^3 = 50.00 \quad (4.5)$$

Consequently, all ports are matched, since the input port-reflection coefficients are equal to the reflection coefficients when the ports are matched. From

$$\Gamma = \frac{Z_{in} - Z_g}{Z_{in} + Z_g}, \quad (4.6)$$

it follows that

$$S_{11} = 0$$

$$S_{22} = 0$$

$$S_{33} = 0 \quad (4.7)$$

**Isolation ( $S_{23}$  and  $S_{32}$ )** It was shown in equation 3.6, that the isolation between the two output port is determined by the mismatch between the even and odd mode matching of the output ports. (Note that  $S_{24}$  and  $S_{42}$  in this equation corresponds to  $S_{23}$  and  $S_{32}$  for the Wilkinson divider) . Thus, in a symmetrical divider, isolation is found from the difference between  $S_{22_e}$  and  $S_{22_o}$  and the reciprocity of the network.

$$S_{23} = \frac{S_{22_e} - S_{22_o}}{2} = 0$$

$$S_{32} = 0 \quad (4.8)$$

**Power Transfer ( $S_{21}$ ,  $S_{31}$ ,  $S_{12}$  and  $S_{13}$ )** Referring to part (b) of Figure 4.1, it is seen that the short circuit at port 1 will ensure that no power is delivered to this port and this port cannot deliver power to any other port. Therefore, the contribution from this port (and to this port) is always zero when excited in the odd-mode.<sup>1</sup>

Thus, using Figure 4.1 (a), a source is added to port 1. The voltage wave incident on  $Z_1$  is then  $V_1^+$  and the reflected wave amplitude ( $V_2^-$ ) is measured at the output of port 2 while port 3 is terminated in a  $50\ \Omega$  such that  $S_{21} = \frac{V_2^-}{V_1^+}$ .

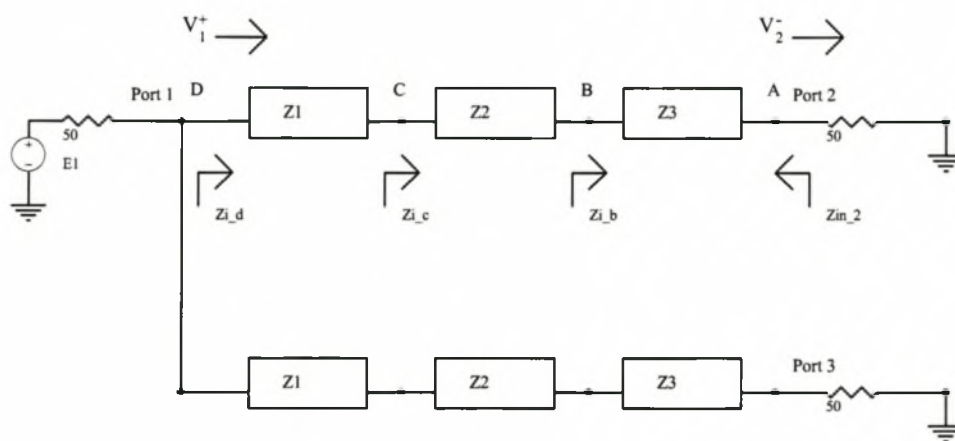


**Figure 4.3:** Circuit for Calculating  $S_{21}$

For each transmission line, the familiar transmission line equation will be used to calculate the voltage at the different nodes. This equation is  $V(x) = V^+(e^{-j\beta x} + \Gamma e^{j\beta x})$ , where  $x$  is defined as positive in the direction from port 1 to port 2

Defining node B as position  $x = 0$  and node A as position  $x = \lambda/4$  the following analysis is done:

<sup>1</sup>The parameters  $S_{ij}$  relate the square root of the power reflected at port  $i$  to the square root of the power incident at port  $j$ . The term 'Power Transfer' is thus technically not a power relation, but rather relates the square roots of reflected and incident power.

Investigating section B-A:

$$\begin{aligned}
 V_A &= V\left(x = \frac{\lambda}{4}\right) \\
 &= V_B^+(e^{-j\beta x} + \Gamma_A e^{j\beta x}) \\
 &= jV_B^+(-1 + \Gamma_A) \\
 \Rightarrow V_B^+ &= \frac{-V_A}{j(1 - \Gamma_A)} \tag{4.9}
 \end{aligned}$$

$$\begin{aligned}
 V_B &= V(x = 0) \\
 &= V_B^+(1 + \Gamma_A) \tag{4.10}
 \end{aligned}$$

By treating each section as a quarter wavelength line between  $x = 0$  and  $x = \lambda/4$ , the rest of the voltages follow easily from the previous analysis:

$$V_C^+ = \frac{-V_B}{j(1 - \Gamma_B)} \tag{4.11}$$

$$V_C = V_C^+(1 + \Gamma_B) \tag{4.12}$$

$$V_D^+ = \frac{-V_C}{j(1 - \Gamma_C)} \tag{4.13}$$

such that

$$V_D^+ = \frac{-1}{j(1 - \Gamma_C)} \frac{-(1 + \Gamma_B)}{j(1 - \Gamma_B)} \frac{-(1 + \Gamma_A)}{j(1 - \Gamma_A)} V_A \tag{4.14}$$

But

$$\begin{aligned}
 V_A &= V_A^+ + V_A^- \\
 &= V_A^+(1 + \Gamma_A) \tag{4.15}
 \end{aligned}$$

The  $S_{21}$  parameter is obtained from the relationship between the incident voltage at port 1 and the reflected voltage at port 2:

$$S_{21} = \frac{V_1^-}{V_2^+} = \frac{V_D^+}{V_A^+} \tag{4.16}$$

Substituting 4.15 into 4.14 results in the necessary relationship:

$$V_D^+ = \frac{-1}{j(1 - \Gamma_C)} \frac{1 + \Gamma_B}{j(1 - \Gamma_B)} \frac{1 + \Gamma_A}{j(1 - \Gamma_A)} \frac{1 + \Gamma_A}{1} V_A^+ \tag{4.17}$$

with

$$\begin{aligned}\Gamma_A &= \frac{50 - Z_3}{50 + Z_3} = -0.270 \\ \Gamma_B &= \frac{Z_{iB} - Z_2}{Z_{iB} + Z_2} = 0.363 \\ \Gamma_C &= \frac{Z_{iC} - Z_1}{Z_{iC} + Z_1} = -0.270\end{aligned}\tag{4.18}$$

It is thus found that

$$S_{21} = \frac{V_D^+}{V_A^+} = -j0.707\tag{4.19}$$

and due to symmetry and reciprocity,  $S_{12} = S_{31} = S_{13} = S_{21} = -j0.707$ .

In summary, the S-parameters were calculated and are summarised:

$$\begin{bmatrix} S_{11} & S_{12} & S_{13} \\ S_{21} & S_{22} & S_{23} \\ S_{31} & S_{32} & S_{33} \end{bmatrix} = \begin{bmatrix} 0 & -0.707i & -0.707i \\ -0.707i & 0 & 0 \\ -0.707i & 0 & 0 \end{bmatrix}\tag{4.20}$$

The S-Parameters of the ideal Wilkinson divider are shown in Figures 4.4 and 4.5. Figure 4.5 accentuates that the ideal division is very flat over the passband.

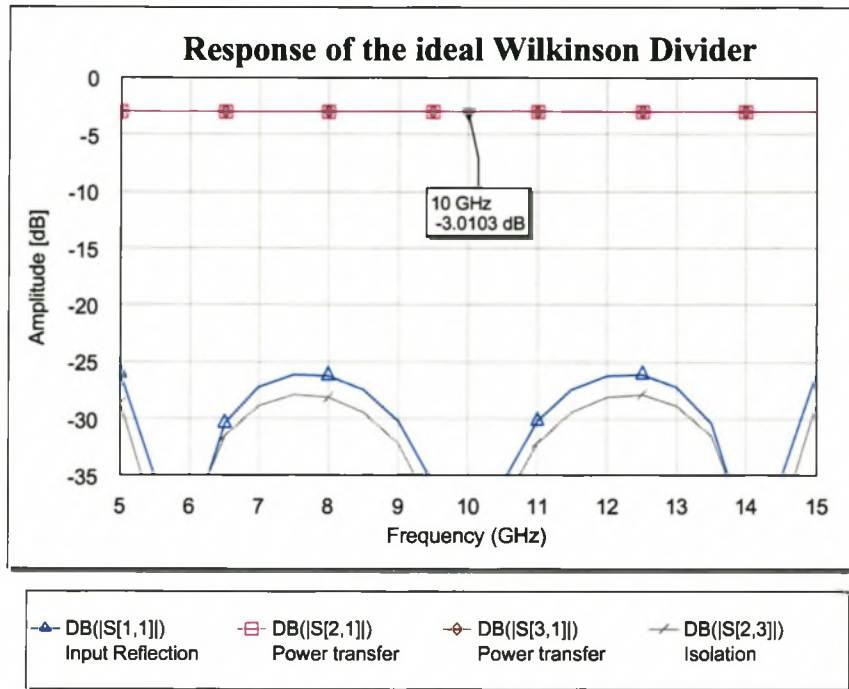


Figure 4.4: Ideal S-Parameters of Wilkinson Divider with N=3

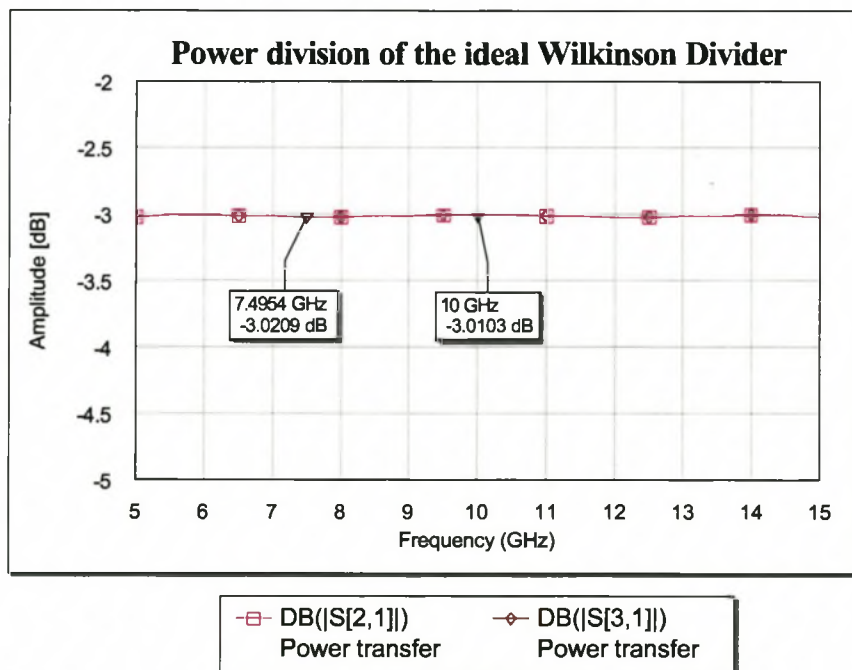


Figure 4.5: Ideal Power Division of Wilkinson Divider with N=3

### 4.3 Implementing the Wilkinson Divider

The Wilkinson divider (Figure 4.2) is implemented in microstrip in order that resistors can be added. The substrate used is a Rogers 5870, which is a low loss substrate of thickness 0.787 mm and dielectric constant 2.33.

Implementing the divider introduced three new issues that need consideration. These are steps in conductor width, splitting of the conductor (to achieve power division) and the behaviour of resistors at high frequency.

#### 4.3.1 Discontinuities due to a Step in Conductor Width

One of the most common problems encountered in implementation of microwave components, is a step change in the impedance of two contiguous lines. The discontinuity adds an unwanted reactance to the structure in the form of extra series inductance and parallel capacitance. Figure 4.6 schematically illustrates the per unit circuit model of two lossless transmission lines and the step discontinuity between them.

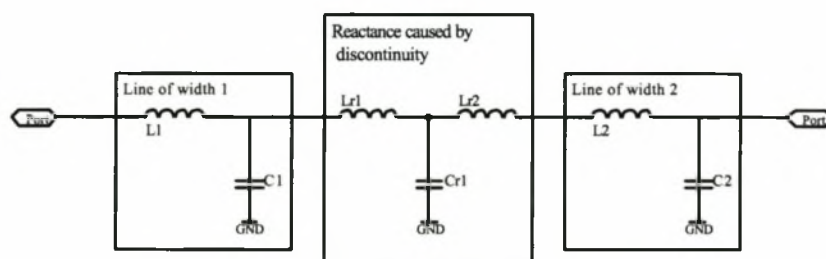


**Figure 4.6:** Reactance Caused by Differing Widths in Microstrip Lines

Empirical equations have been developed to calculate the values of the capacitance and inductance associated with the step in discontinuity [15]. These equations are valid in very specific ranges of dielectric constant, dimensioning of lines and are valid for symmetrical steps in width.

Discontinuity compensation has been covered extensively in the literature ([2] [18]). A simple and highly effective method was introduced by Chadha and Gupta [9] and is the basis of all discontinuity modelling in this thesis.

To reduce the effects of discontinuity reactances associated with steps in width, the step can be mitered so that the width varies in a tapered manner. Chadha and Gupta investigated 3 cases. In all cases the taper was linear and the angle of the taper was changed from 30 to 45 and finally to 60 degrees. If the angle is  $\theta$  in Figure 4.11, they found the optimum angle to be 30 degrees.

This thesis approaches the investigation to the optimum angle slightly differently from the article due to the availability of numerical method resources. (Refer to [9] for details on a different approach).

Two requirements need to be met when deciding on a compensating profile. The first is that the magnitude of  $S_{11}$  should be as small as possible and secondly, the phase response should not be affected by the compensation. This is done by ensuring that the electrical length (phase of  $S_{21}$ ) of the tapered line is as close as possible to that of two ideal contiguous lines.

**Determining and Compensating for the Error Introduced by a Step Discontinuity** Upon determining the dimensions required to obtain the characteristic impedances of the contiguously spaced  $90^\circ$  lines of the Wilkinson divider,  $|S_{11}|$  and  $\angle S_{21}$  are calculated (using EM software). These values are compared to the parameters of ideal and mitered transmission lines of the same impedance and electrical length.

Figures 4.7 and 4.8 show the input reflection coefficients and error in phase of  $S_{21}$  for differently angled tapers when compared to an ideal transition. In all cases the widths of the two lines were 1.23 mm and 1.76 mm, resulting in a 0.53 mm step. From Figure 4.7, it is evident that the magnitude of  $S_{11}$  is not greatly affected by changing the angle of the taper. The reason being that the step is small compared with a wavelength ( $\approx 0.03\lambda$  at 10 GHz). There is however, a phase error observed in the electrical length when the line is not mitered. The parasitic discontinuity reactance has the effect of making the line look longer, thereby lowering the resonant frequency of the line. When no compensation is done, a phase difference of approximately  $6^\circ$  is calculated between the ideal and unmitered case. This is indicated in Figure 4.8, where a logarithmic scale was used to highlight the error. If the line was shortened a little bit, this error would disappear.

Mitering removes some of the excess reactance, thereby reducing the phase error.

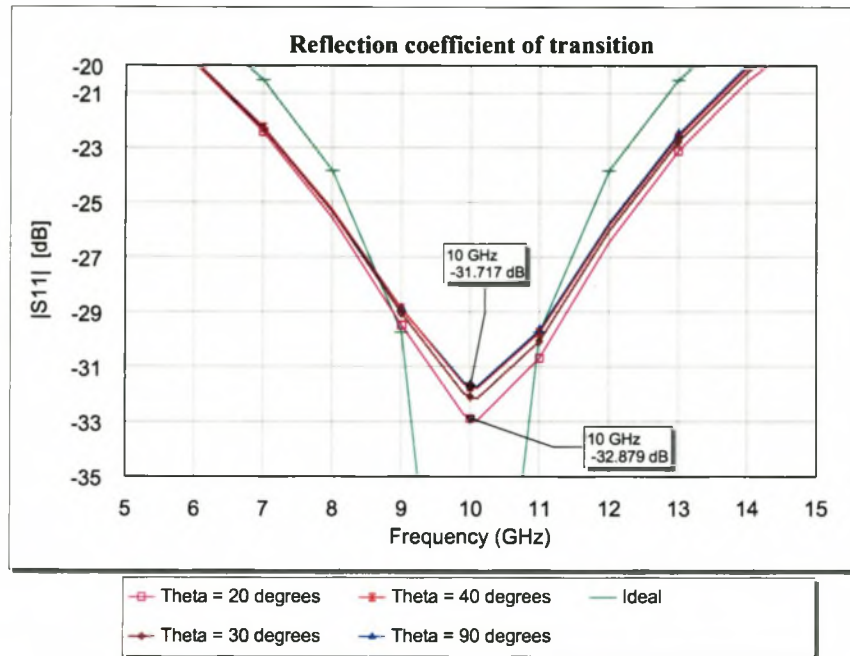


**Figure 4.7:** Input Reflection Coefficient ( $S_{11}$ ) of two Contiguous Lines of Different Widths. Step Size is 0.53 mm. Angle of Transition is Varied from  $20^\circ$  to  $90^\circ$ . (Computed using MWO)

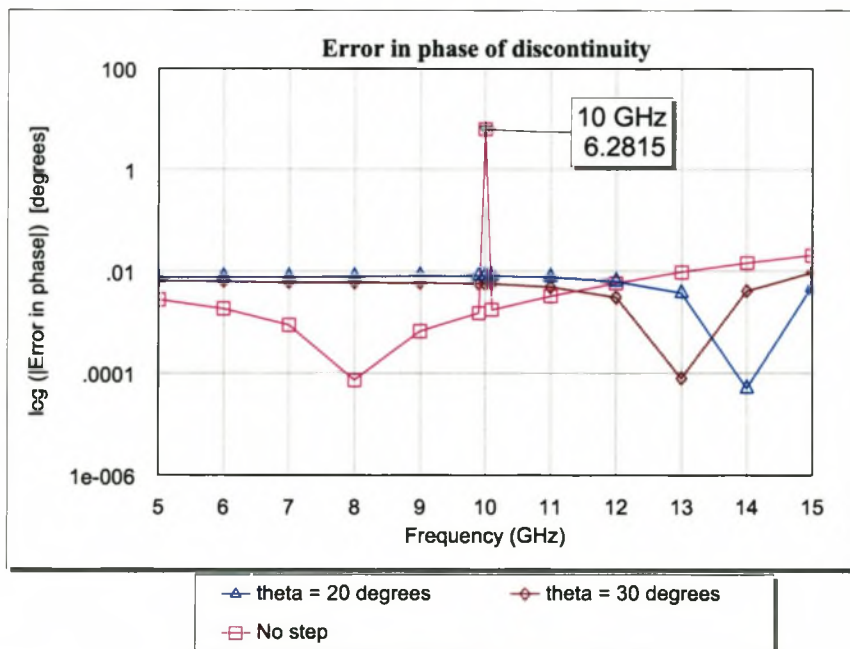


**Figure 4.8:** Error in Phase for Differently Mitered Angles when Compared to an Ideal Transition. (Computed using MWO)

It is concluded that a mitered corner of either  $20^\circ$  or  $30^\circ$  should be used as the  $|S_{11}|$  results are slightly better and the phase error is reduced. The literature suggests  $30^\circ$ , as such lines are shorter than  $20^\circ$  lines. Angles smaller than  $20^\circ$  become impractical as the structure becomes too long.

### 4.3.2 Y-Junctions

This Wilkinson power divider requires a  $50\ \Omega$  line to be connected to the parallel combination of two  $86.98\ \Omega$  lines. Due to the required geometry restrictions, this was implemented using a Y-junction, where the  $50\ \Omega$  line would be represented by the bottom leg of the "Y".

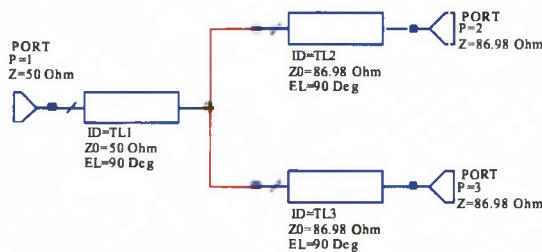


**Figure 4.9:** Circuit for Measuring Input Reflection Coefficient of Y-Junction

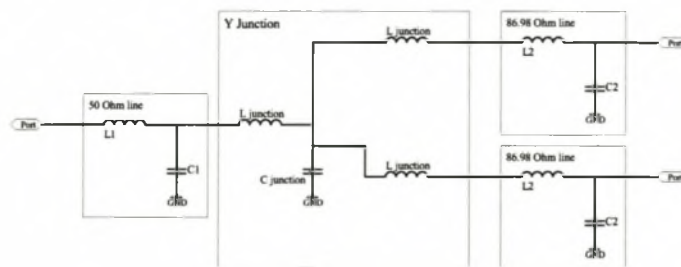


**Figure 4.10:** Lumped Element Representation of Transmission Line and Y Junction

The per unit circuit model of a Y-junction is shown in Figure 4.9 and the lumped element representation of the junction is shown in Figure 4.10. The model shows three lossless transmission lines connected with a Y-junction. In the lossless line, the capacitance is a function of the cross sectional properties (width of microstrip, distance between ground and microstrip and the dielectric constant of the sandwiched dielectric). The inductance

is mostly due to the length of the microstrip. As such, the Y-junction is seen to increase the effective length of each line, whereas the capacitance represents a discontinuity in cross-sectional properties.

To compensate for the unwanted reactance of the junction, it is necessary to decrease the length of each line and reduce the effect of the discontinuity capacitance by making the junction gradual and not abrupt.

In the article by Chadha and Gupta, T-junctions were investigated. Since the Y junction is in many ways similar to a T-junction, concepts about T-junctions can be used for the Y-junction application.

Their method involves removing a triangular portion from the section of intersect of a T-junction. Similar to before, three cases were investigated; namely when the angle is  $30^\circ$ ,  $45^\circ$  and  $60^\circ$ .

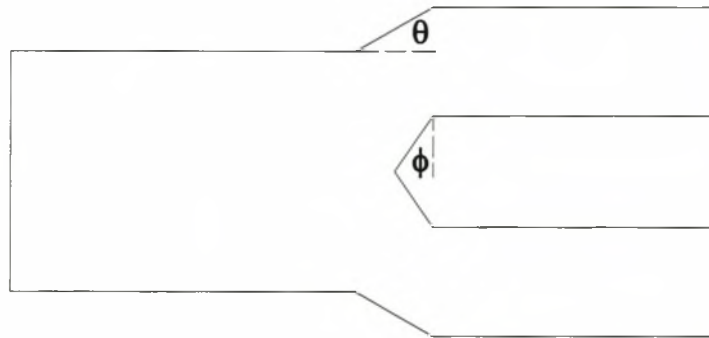


**Figure 4.11:** Definition of Angles for Y-Junction Compensation

The article finds that an angle of  $30^\circ$  is optimum in the cases they investigated. (Note that the angle in this article is the complement of the angle  $\phi$ , shown in Figure 4.11)

The same method as before is followed, but now angles  $\theta$  and  $\phi$  (Figure 4.11) are varied. The cases investigated are summarised in 4.21.

$$\begin{aligned}
 \theta &= 90^\circ & \phi &= 0^\circ \\
 \theta &= 30^\circ & \phi &= 30^\circ \\
 \theta &= 45^\circ & \phi &= 0^\circ \\
 \theta &= 45^\circ & \phi &= 30^\circ
 \end{aligned}
 \tag{4.21}$$

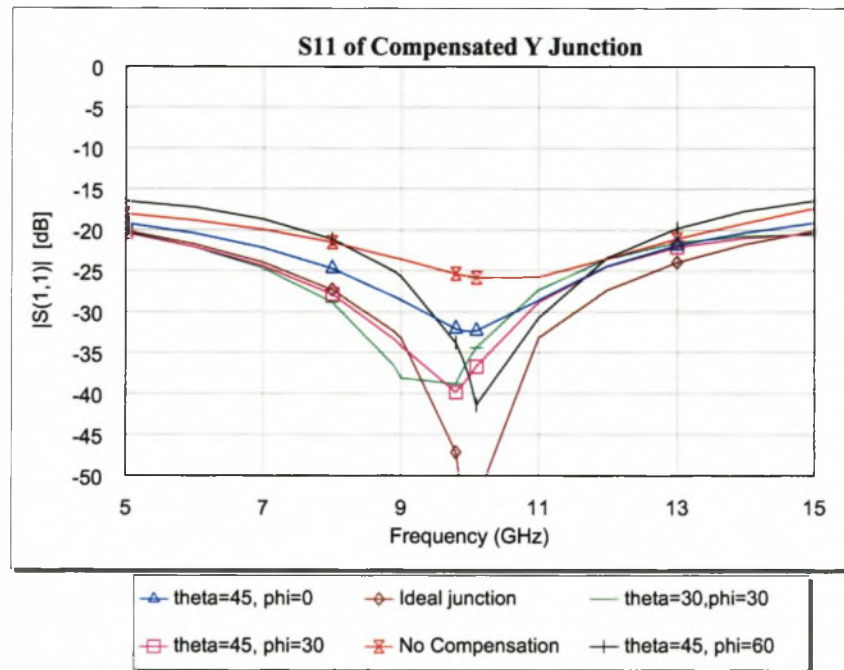


**Figure 4.12:** Comparison of Selected S-Parameters of Compensated Y-Junction and Ideal Transmission Line Junction Model. (Computed using MWO)

The expected  $|S_{11}|$  results are shown in Figure 4.12. This figure depicts that an uncompensated ( $\theta = 90^\circ, \phi = 0^\circ$ ) Y-junction has more reflection than the compensated structure. The optimum angles are  $\theta = 45^\circ$  and  $\phi = 30^\circ$ .

Due to a calculation error in the early stages of the design, the optimum angles were not implemented. The implemented angles are  $\theta = 30^\circ$  and  $\phi = 60^\circ$ . The line of the microstrip sections had to be shortened to ensure the correct electrical length. Figure 4.13 compares the difference in phase between  $S_{21}$  of the uncompensated junction and ideal junction and the difference in phase between the implemented junction and the ideal junction. (Note the logarithmic y-axis, which is used to highlight the theoretical differences). The difference between the implemented junction ( $\theta = 30^\circ$  and  $\phi = 60^\circ$ ) and ideal junctions are theoretically  $0.03^\circ$ . The significant difference in electrical length for the uncompensated case results because the resonant frequency of the uncompensated line has been lowered by the added reactance.

In conclusion, it is possible to improve reflection and phase errors caused by step discontinuities by mitring the angles and reducing the line lengths.

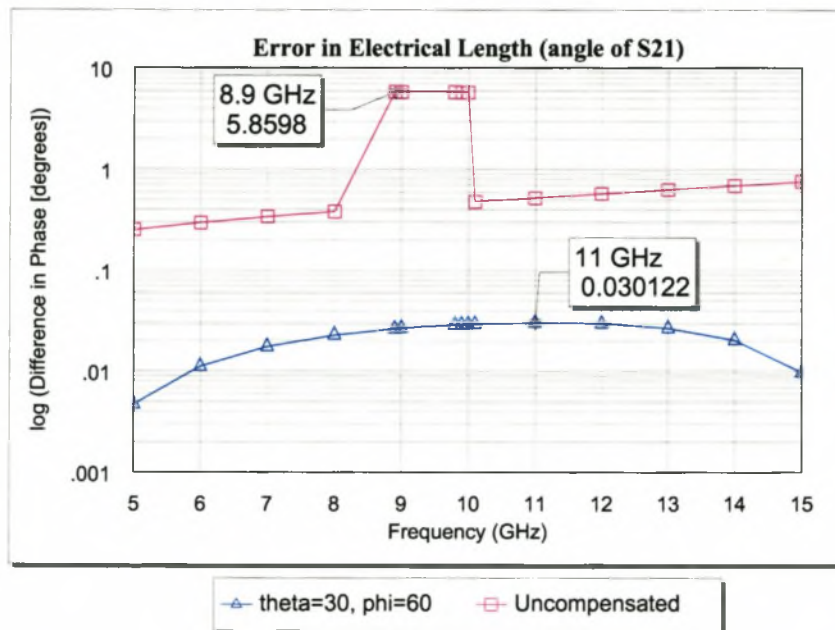


**Figure 4.13:** Comparison of Electrical Length of Compensated Y-Junction and Ideal Transmission Line Junction Model. (Computed using MWO)

### 4.3.3 Non-ideal Behaviour of Resistors at High Frequency

The circuit model for a resistor at high frequencies is shown in Figure 4.14. The values shown on the figure are typical of good quality high frequency resistors and not the actual values of the resistors used.

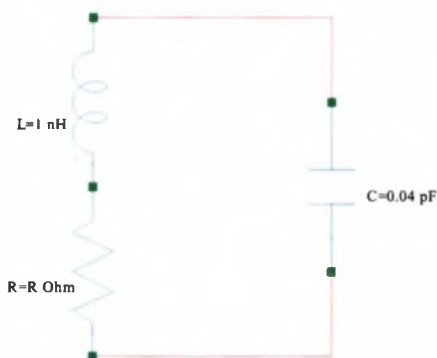


**Figure 4.14:** High Frequency Model of a Resistor

The frequency behaviour of a typical 100 Ω resistor is shown in Figure 4.15, where it is seen

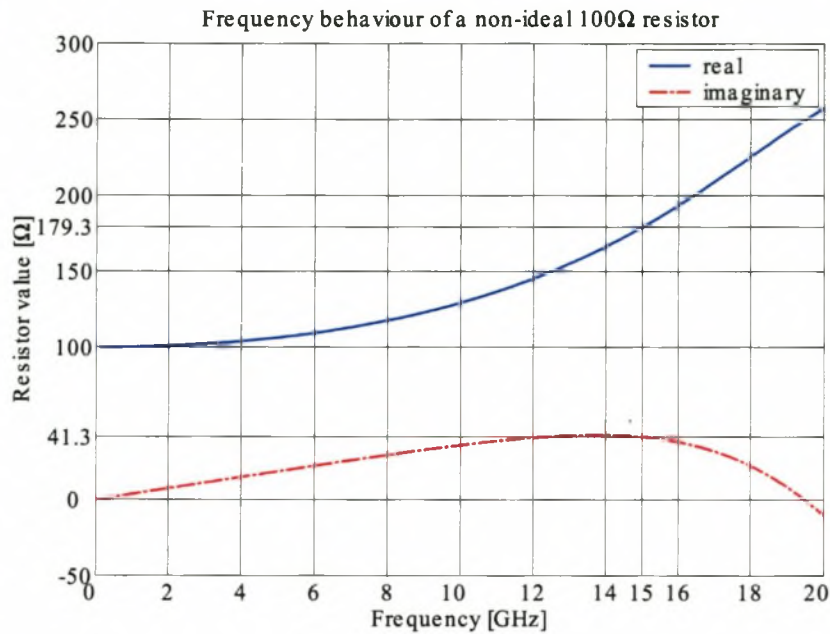


**Figure 4.15:** Frequency Behaviour of a Non-ideal 100  $\Omega$  Resistor. (Computed using Matlab)

that the ideal 100  $\Omega$  increases to a value of  $179.3 + j41.3 \Omega$  at 15 GHz. (The inductance value is an estimate of the inductance of a transmission line of physical dimensions similar to those of a typical resistor. Refer to appendix D for capacitance data for a typical high frequency resistor.)

The effect of increasing the capacitance of the typical high frequency resistor on the isolation properties of the Wilkinson divider is shown in Figure 4.16. The isolation provided by ideal resistors is compared to the isolation provided by typical high frequency resistors (capacitance = 0.04 pF, inductance 1 nH) and resistors with capacitance = 0.08 pF. From this figure, it is seen that a resistor with parallel capacitance exceeding 0.04 pF will greatly affect the useful bandwidth of the divider.

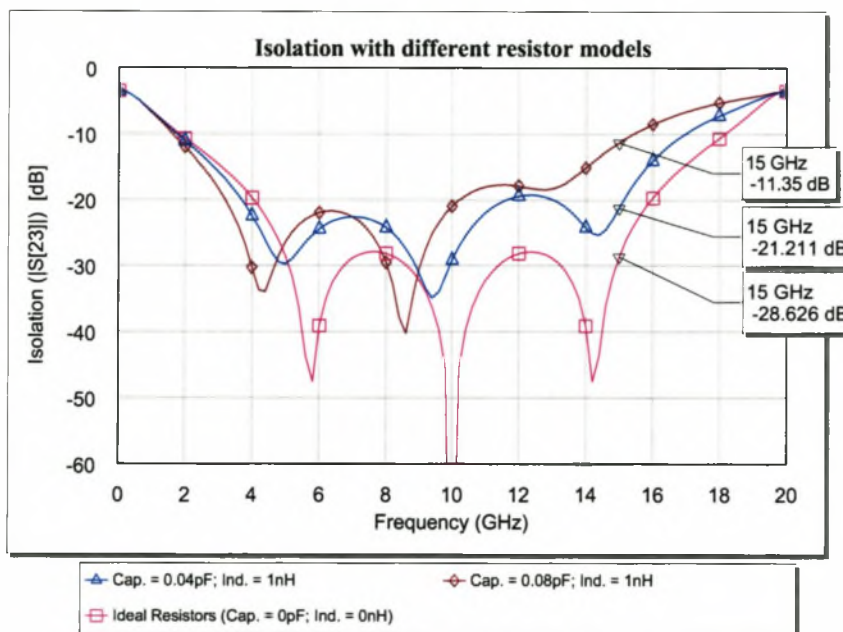


**Figure 4.16:** Effect of Non-Ideal Resistor Values on Isolation of the Wilkinson Divider. (Computed using MWO)

### 4.3.4 Connectors and Right-Angled Bends

As discussed in 3.5.2, connector junction compensation is necessary. This was done in a similar way to the low frequency coupler. The calculated response of the junction is shown in Figure 4.17

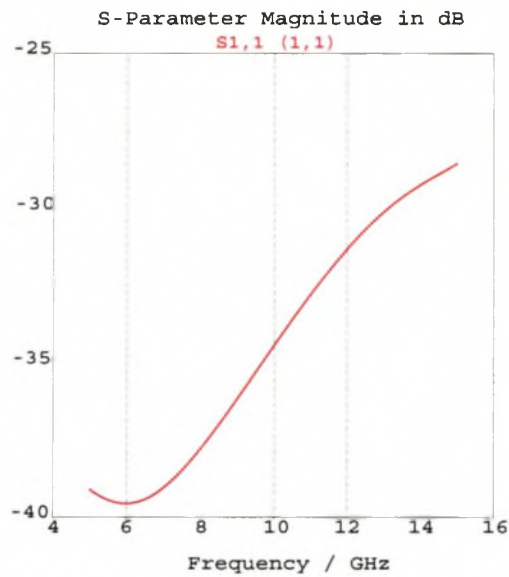


**Figure 4.17:** Calculated Reflection Coefficient of the Connector Transition to Wilkinson Divider. (Computed using CST)

## 4.4 Results: Wilkinson Divider

### 4.4.1 Layout

The layout of the Wilkinson divider is shown in Figure 4.18, where the circles indicate the position of the screws. The inner dimensions of the box housing the divider are 24 mm × 43 mm × 10.79 mm.

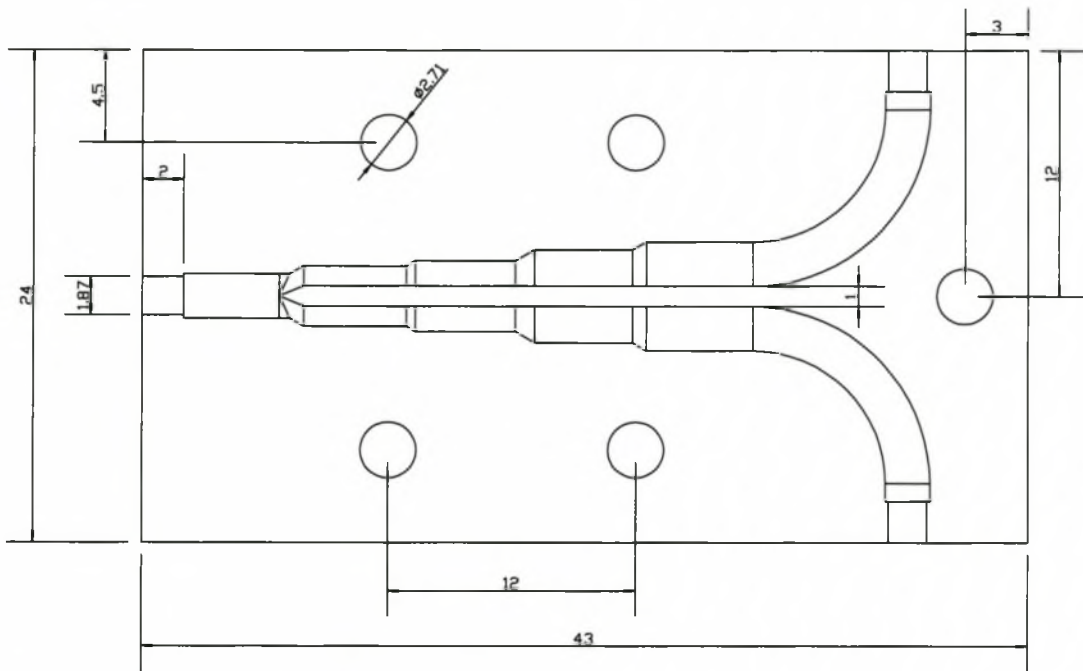


**Figure 4.18:** Layout of the Wilkinson Divider. Dimensions in mm.

The approximate cutoff frequencies and modes that can propagate in the Wilkinson divider, are calculated using equation 4.22.

$$f_{c_{mn}} = \frac{1}{2\pi\sqrt{\mu\epsilon_0\epsilon_{re}}}\sqrt{\left(\frac{m\pi}{a}\right)^2 + \left(\frac{n\pi}{b}\right)^2} \quad (4.22)$$

$\epsilon_{re}$  is the effective dielectric constant of the waveguide partially filled with microstrip.

$$\begin{aligned}\epsilon_{re} &= \frac{\epsilon_r}{2} + \frac{\epsilon_r - 1}{2} \frac{1}{\sqrt{1 + 12h/W}} \\ &= 1.952\end{aligned}\tag{4.23}$$

The height ( $h$ ) of the microstrip is 0.787 mm and the width ( $W$ ) of the ( $50 \Omega$ ) line is 2.154 mm.

The unwanted modes that can be excited in the cavity are indicated in table 4.1.

**Table 4.1:** Cutoff Frequencies and Modes in the Wilkinson Divider

<i>Mode</i>	<i>m</i>	<i>n</i>	$f_{c_{mn}}$ (GHz)
TE	1	0	3.8
TE	2	0	8.0
TE,TM	1	1	11
TE	3	0	12
TE,TM	2	1	13

The screws are necessary for suppressing undesirable higher order modes. An absorbing material was added to the roof of the cavity, which succeeded in suppressing those resonant frequencies not suppressed by insertion of the screws.

## 4.5 Measurement

The Wilkinson divider was tested at the same time as the directional coupler. The calibration and general set-up is as before. The Wilkinson divider did not require gender changers.

The measured results are shown in Figure 4.19 where it is plotted against the MOM results obtained using MWO.

The calculated input reflection is better than  $-18.5$  dB across the bandwidth. Power division at the output ports is calculated to be between  $-3.75$  dB and  $-3.65$  dB. The ripple amplitude for  $S_{21}$  and  $S_{31}$  is therefore  $\pm 0.05$  dB.

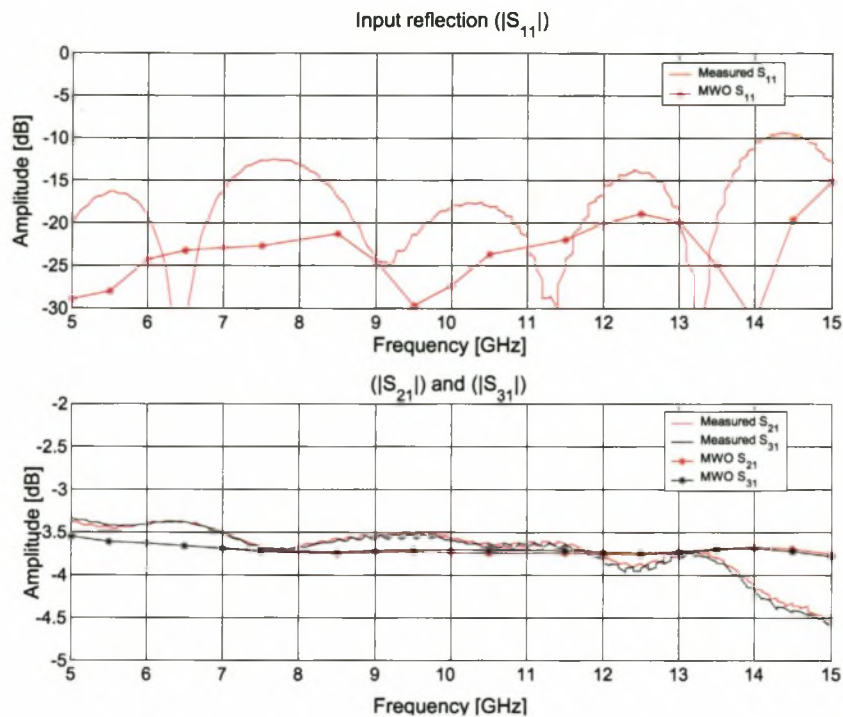


**Figure 4.19:** Comparison of Measured and Calculated Results of Wilkinson Divider. (Measured and computed using MWO)

The measured input reflection coefficient ( $|S_{11}|$ ) is better than  $-12.5$  dB across the whole passband. Power division is measured to be between  $-3.96$  dB and  $-3.37$  dB. The measured ripple amplitude is thus  $\pm 0.3$  dB.

The isolation ( $|S_{23}|$ ) achieved was excellent. (Figure 4.20). It was measured below  $-17$  dB over the passband. Port matching ( $|S_{22}|$ ) was achieved with a maximum mismatch of  $-11.5$  dB. The reciprocal nature of the Wilkinson divider is demonstrated by  $|S_{23}|$  being equal to  $|S_{32}|$  in this graph.

#### 4.5.1 Discussion of Results

The calculated results obtained for  $S_{21}$  and  $S_{31}$  agree very well with the measured results.

The measured and calculated  $|S_{11}|$  differ significantly. The superior performance of the calculated values is due to the ideal ports used in simulation ( $50 \Omega$  at all frequencies). In practice, the ports are not ideal and the transition from connector to microstrip was

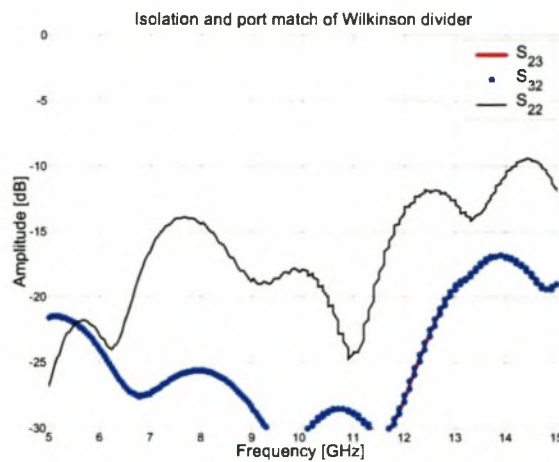


**Figure 4.20:** Isolation and Port Match of the Wilkinson Divider ( $S_{23}$ ,  $S_{32}$  and  $S_{22}$ ). (Computed using Measured)

non-ideal. As with the coupler, various factors can affect  $S_{11}$ . Two of these are listed below:

- Simulation of junction sections may not have been accurate. CST has two independent accuracy settings. The mesh density is specified independent of an accuracy setting that must be selected at simulation time. After the junctions were simulated, it was found that the accuracy of the default mesh settings is not good when simulating complex structures. Due to inexperience with CST, the transition was designed with the default mesh settings. The other accuracy setting works with the selected (or default) mesh setting, but runs more analyses. Selecting this accuracy to be higher, mathematically yields a more accurate number, but accuracy is still limited to the mesh size.
- Non-ideal terminations affect the results. This has already been discussed.

The effect of a 5 % variation in (real part of the) terminating impedances (and consequently variation in connector transitions) is shown in Figures 4.21 and 4.22.

Figure 4.21 shows that the non-ideal behaviour of the loads can cause a reflection coefficient of  $-13.6$  dB, which is near the measured value of  $-12.5$  dB.

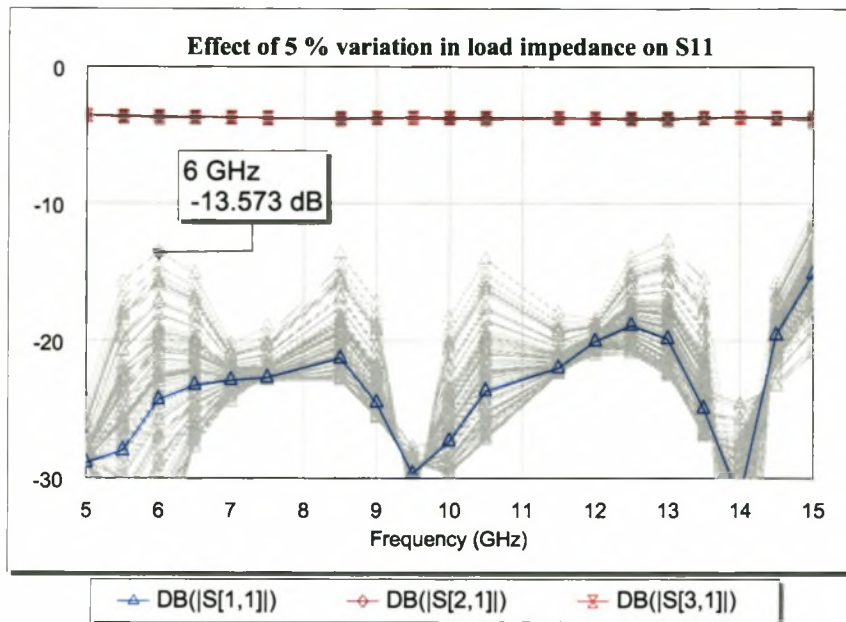


Figure 4.21: Effect of Non-ideal 50 Ω Terminations on the Input Reflection of the Wilkinson Divider. (Computed using MWO)

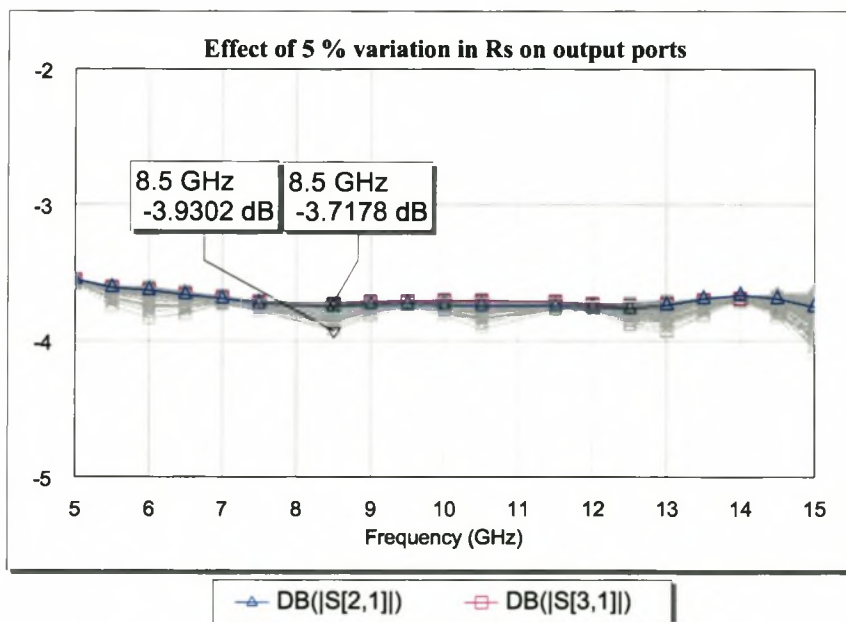


Figure 4.22: Effect of Non-ideal 50 Ω Terminations on the Power Division of the Wilkinson Divider. (Computed using MWO)

## 4.6 Conclusion

This chapter showed the details involved in designing and implementing a three section Wilkinson power divider at microwave frequencies. An even and odd mode analysis was done to verify design parameters obtained from the literature.

The details of implementing the divider, with specific reference to those problems not encountered in the low-frequency coupler, are discussed. A discussion on the frequency behaviour of resistors is presented and it is shown that typical high frequency resistors are only suitable up to approximately 15–20 GHz. In the final part of the chapter, the measured results are shown, where it was found that the power division corresponds extremely well with the designed power division across the whole frequency band. The reflection is better than  $-12.5$  dB over the whole passband.

It is easy to design a Wilkinson divider and to implement the divider at low frequencies. As X-band is approached however, the parasitic effects of junctions and resistors become significant. Above approximately 15 GHz, typical high frequency resistors cannot provide sufficient isolation.

For frequencies up to 15 GHz, the Wilkinson divider performs significantly better than the coupler in that its output power division is almost constant over the bandwidth. At higher frequencies, the resistors will severely affect this performance and it will be difficult to implement.

The Wilkinson divider performs well enough not to require a second iteration.

A picture of the completed Wilkinson divider is shown in Figure 4.23.

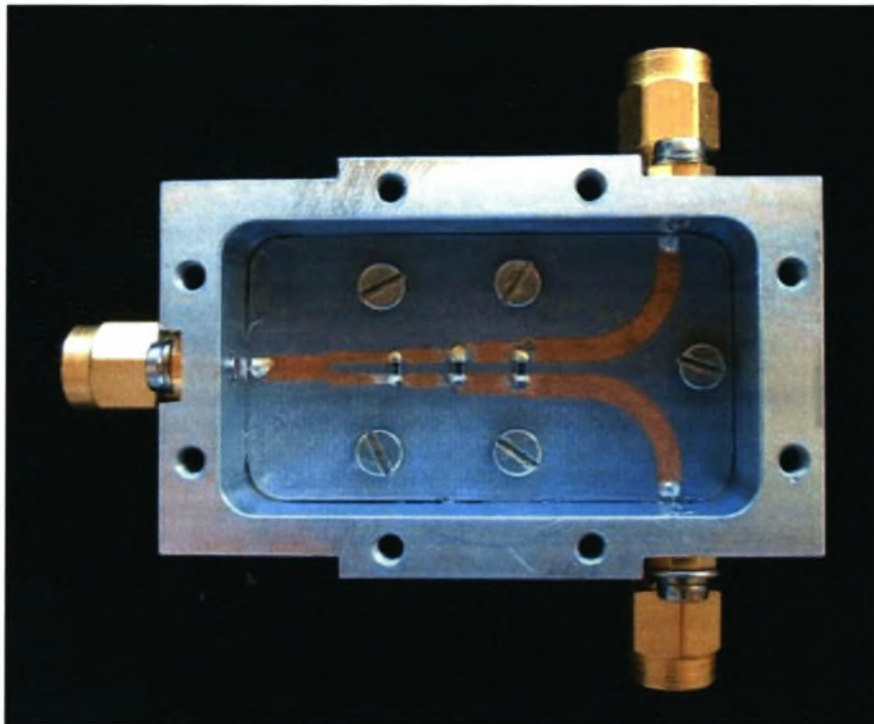


**Figure 4.23:** The Completed Wilkinson Divider

# Chapter 5

## Power Handling

### 5.1 Introduction

As a subset of microwave passive components, stripline and microstrip configurations are not fundamentally suited to high power applications. For a comparable cross-section, waveguide and coaxial cable can handle significantly higher power. [20]

Microstrip and striplines are not limited to milliwatt applications. By designing the microstrip and stripline device properly, it is possible to achieve power handling of up to tens of kilowatts.

### 5.2 Peak Power

The peak power that can be applied without causing dielectric breakdown determines the peak power handling capability (PPHC) of these lines. In table 5.1 the dielectric strength and other material properties of the materials used in designing the coupler (Taconic TLY-5) and Wilkinson divider (Rogers 5870) are compared to those of Alumina (which is a low loss substrate) and air. It is found that the Taconic substrate can handle very high peak voltages.

In some cases connectors or launchers decide the PPHC of the device. For instance,

**Table 5.1:** Material Properties of Selected Substrates

<i>Material</i>	$\epsilon_r$	<i>Loss Tangent, <math>\tan \delta</math> at 10 GHz</i>	<i>Thermal conductivity, K (W/cm/°C)</i>	<i>Dielectric strength (kV/cm)</i>
Alumina	9.7	0.0002	0.3	4000
Taconic TLY-5	2.2	0.0009	0.4	4724
Rogers 5870	2.33	0.0012	0.22	
Air	1	0	0.00024	30

the Radial SMA connector used in the design of the coupler has a maximum dielectric withstanding voltage of 1000 V, compared to the 60 000 V of the Taconic TLY-5 substrate.

### 5.3 Average Power

The average power handling capability (APHC) of microstrip is determined by the temperature rise of the strip conductor and the supporting substrate. Gupta *et al* in [23, p88] list the parameters that affect average power handling in microstrip and striplines as: (i) transmission line losses; (ii) thermal conductivity of the substrate material; (iii) surface area of the strip conductor; and (iv) ambient temperature of the medium surrounding the microstrip.

Another aspect that influences the power handling capability of microstrip and striplines, is the profile of the metal conductor. A rectangular cross-section will cause a concentration of electric fields at the corners, and breakdown will happen at a lower applied voltage. This can be overcome by manufacturing the conductors with slightly rounded edges.

Howe [19] has reported successful operation of microstrip lines up to 4 kW at X-band frequencies.

### 5.4 Predicted Power Handling Capability of Coupler

The predicted maximum average power that the coupler and divider can handle was calculated from the theory developed by Gupta *et al*. The coupler was taken as a symmetrical

stripline, with a single track of width equal to the minimum width of the actual coupler. This may not be accurate as the coupler consists of two tracks that cross over each other. Theoretical data for this is not available and tests would have to be done to find the actual power handling capability.

The equation for the predicted power is the same for microstrip and stripline, but the calculation is slightly different. For the stripline coupler, the rise in temperature per watt in a line is given by Gupta *et al* as

$$\Delta T = \frac{0.2303 b}{K} \left[ \frac{\alpha_c}{W_e} + \frac{\alpha_d}{2W_{eff}} \right] \quad (^\circ C/W) \quad (5.1)$$

where

- b = height of stripline =  $0.889 \times 10^{-3}$  [m]  
 K = Thermal conductivity =  $0.4$  [ $W/m/^\circ C$ ]  
 $\alpha_c$  = attenuation due to conductor loss  
 $\alpha_d$  = attenuation due to dielectric loss  
 $W_{eff}$  = Effective width = Width (when stripline)

The attenuations are calculated from

$$\begin{aligned} \alpha_c &= \frac{2.7 \times 10^{-3} R_s \epsilon_r Z_0}{30\pi(b-t)} A \\ A &= 1 + \frac{2W}{b-t} + \frac{1}{\pi} \frac{b+t}{b-t} \ln \left( \frac{2b-t}{t} \right) \end{aligned} \quad (5.2)$$

with

- $R_s$  = Surface resistivity of copper =  $\frac{1}{5.8 \times 10^7} = 17.24 \times 10^{-9} \Omega$   
 W = smallest width of the line =  $0.4825$  mm  
 t = thickness of conductor =  $18 \mu m$ ,

such that

$$\begin{aligned} \alpha_c &= 62.38 \times 10^{-9} \text{ Np/m} \\ &= 541.8 \times 10^{-9} \text{ dB/m} \end{aligned} \quad (5.3)$$

The attenuation due to dielectric loss is calculated from

$$\begin{aligned}\alpha_d &= \frac{k \tan \delta}{2} \\ &= 139.8 \text{ mNp/m} \\ &= 1.214 \text{ dB/m}\end{aligned}\tag{5.4}$$

with

$$\begin{aligned}k &= \omega \sqrt{\mu \epsilon} \\ &= 2\pi \cdot 10e^9 \sqrt{\mu_0 \epsilon_0 \cdot 2.2} \\ &= 310.6 \\ \tan \delta &= 0.0009\end{aligned}\tag{5.5}$$

The rise in temperature is calculated from 5.1 as  $0.644^\circ\text{C}/\text{W}$ . The maximum average power for a line with a continuous width as specified above is calculated from:

$$P_{avg} = (T_{max} - T_{amb})/\Delta T,\tag{5.6}$$

where  $T_{max}$  is the maximum operating temperature and  $T_{amb}$  is taken as  $25^\circ\text{C}$ . For purposes of later comparison,  $T_{max}$  is taken as  $100^\circ\text{C}$ .

The maximum calculated average power capability of the coupler (assuming a constant line width equal to the minimum width of the track) is calculated to be  $116.5\text{W}$ .

A similar calculation is done for the Wilkinson divider (excluding resistors). High frequency resistors of the dimensions used in this thesis can typically dissipate a continuous power of less than  $100\text{mW}$ .

For microstrip, the effective width is frequency dependent.  $W_{eff}$  is calculated as follows:

$$W_{eff}(f) = W + \frac{W_{eff}(0) - W}{1 + (f/f_p)^2}\tag{5.7}$$

where

$$f_p = \frac{Z_0}{2\mu_0 h}\tag{5.8}$$

$$W_{eff}(0) = \frac{120\pi h}{Z_0 \sqrt{\epsilon_{re}}}\tag{5.9}$$

The effective dielectric constant was calculated earlier.

In summary,

$h$ =height of microstrip substrate =0.787 mm

$\epsilon_{re}$ = effective dielectric constant =1.952

$W$ =width of 50  $\Omega$  microstrip line =2.154 mm

The attenuation due to the microstrip dielectric is calculated in the same way as before and is 1.7 dB/m. Attenuation due to the conductor is found to be  $5.4 \times 10^{-6}$  dB/m. The maximum calculated average power that the Wilkinson divider can handle (assuming a constant line width equal to the minimum width of the track) is calculated to be 433W.

These values were higher than intuitively expected, but upon comparison with microstrip lines of similar dimensions it was found that these values were reasonable. Table 5.2 compares the maximum Average Power Handling Capability of various substrates. In all cases (except for the coupler, where the smallest width of the line was used as this number is lower than the 50  $\Omega$  case),  $T_{max}$  was taken as 100°C,  $T_{amb}$  was 25°C,  $Z_0$  was taken as 50  $\Omega$  and  $f$ = 10 GHz.

**Table 5.2:** Comparison of APHC for Various Substrates[23]

<i>Substrate</i>	<i>Maximum Average Power (kW)</i>
Polystyrene	0.124
Quartz	0.523
Alumina	5.17
Beryllium oxide (BeO)	75.7
Wilkinson divider (Rogers 5870)	0.433
Coupler (Taconic) (50 $\Omega$ )	0.164
Coupler (Taconic) (Smallest width)	0.116

Alumina is a substrate that is favoured by many designers. It was found that one of the reasons for this, is that its power handling capability is far superior to other commonly found substrates. This is ascribed to it being a very low loss substrate ( $\tan \delta = 0.0002$  at 10 GHz), with a comparatively high thermal conductivity coefficient.

## 5.5 Conclusion

The power handling capability of microstrip line structures is affected by frequency of operation, material properties, construction and often is limited by the connector or the junction between the connector and the structure.

To increase the capacity of the microstrip line to handle power at a given frequency, it is imperative to use a low loss substrate with a high thermal conductivity (K). Wider tracks (lower impedance) can handle more power than thinner tracks. In the case of the coupler, this implies designing a coupler with even less stringent coupling requirements. A cascaded design is well suited for this, as increasing the number of cascaded sections, will decrease the coupling requirements and therefore increase the maximum power the coupler can handle.

# Chapter 6

## Finite Difference Time Domain method (FDTD)

### 6.1 Introduction

Gedney and Hagness describe the FDTD method as follows:

‘FDTD and related space-grid time-domain techniques are direct solution methods for Maxwell’s curl equations. These methods employ no potentials. Rather, they are based upon volumetric sampling of the unknown electric field  $\vec{E}$  and magnetic field  $\vec{H}$  within and surrounding the structure of interest, and over a period of time. The sampling in space is at sub-wavelength (sub- $\lambda_0$ ) resolution set by the user to properly sample the highest near-field spatial frequencies thought to be important in the physics of the problem. Typically, 10–20 samples per  $\lambda_0$  are needed. The sampling in time is selected to ensure numerical stability of the algorithm’[40].

The FDTD technique uses a marching-in-time (sometimes called ‘leapfrogging’) procedure that simulates actual electromagnetic wave propagation and is terminated at a boundary outside the computational region of interests by a boundary condition, such as an absorbing boundary condition (ABC), a perfect electric conductor (PEC) or by inserting an absorbing layer at the outer boundary.

The Perfectly Matched Layer (or PML), is such a layer. It is in many ways similar to RF

and acoustic absorbers found in anechoic chambers; it simulates free space by absorbing electromagnetic signals, which reach a dimensionally small absorbing layer around the area of interest. Manufacturers of RF-absorbers and anechoic chambers can guarantee reflection levels of approximately  $-50$  dB at 10 GHz in a standard chamber.

For the RF designer it is important not to be limited by computational ABC's, but rather by physical constraints, such as RF absorbing in anechoic chambers. It will be shown later that current computational boundary termination methods can easily satisfy the  $-50$  dB requirement of typical anechoic chambers.

Some of the current ABCs used in the FDTD method are summarised below. [40, Chap. 6]

**Bayliss-Turkel Radiation Operators** This method constructs a linear partial differential operator from a weighted sum of three types of derivatives of the field. The differential operator systematically 'annihilates' terms of the outgoing-wave expansion, leaving a remainder term that diminishes to zero as an inverse power of  $R$ , the distance from the observation point to the origin.

**Engquist-Majda one-way wave equations** This is a partial differential equation method that permits wave propagation only in certain directions and can therefore absorb impinging outgoing waves. The one-way wave equation method includes Taylor series approximations, Mur first and second order schemes, Trefethen-Halpern Generalized and Higher Order ABCs such as Padé, Chebyshev and the least squares method.

**Higdon Radiation Operators** Higdon's technique involves the construction of a series of linear differential operators to annihilate outgoing numerical waves propagating at specific angles in a Cartesian grid rather than the Bayliss-Turkel sum of radially propagating waves in a cylindrical or spherical grid.

**Liao Extrapolation in space and time** This extrapolation is based upon what the authors called the 'multitransmitting theory' and exhibits 10-20 dB less reflection than the second-order Mur condition.

**Ramahi Complementary operators (COM or C-COM)** These operators cancel the residual outer-boundary numerical wave reflections that result from applying standard analytical ABCs such as the one-way wave equations. This method can achieve

an outer-boundary reflectivity as little as 1/1000th that of the best previous analytical ABCs such as Higdon's fourth-order operator (typically  $-100$  dB)

**Berenger's Perfectly Matched Layer (PML)** An absorbing layer that matches plane waves of arbitrary incidence, polarization and frequency at reflections of less than  $-75$  dB (depending on layer thickness). This method can be shown to have more utility than the C-COM method for classes of problems involving the need to terminate space lattices in guided-wave structures having multiple, significant corner-type reflections and other reverberations.

Balanis *et al* did a comparative study in [3], where the Berenger PML is compared to a 7<sup>th</sup> order Lindman ABC and a second order Mur ABC. (The Lindman ABC falls into the Enquist and Majda category above).

The Berenger PML consistently outperformed the other two, which were more frequency dependent. The PML performs significantly better at low frequencies as its layer thickness is independent of frequency (typically between 5 and 15 cells) and both the other methods are dependent on wavelength or part thereof, thus greatly increasing the required number of cells at low frequency.

The Lindman ABC performed better than Mur at lower frequencies but equalled the Mur performance at higher frequencies. Tavlove *et al* in [22] found that the Berenger PML yields approximately  $-40$  dB less reflection than second order Mur [40].

Wu and Fang [43], in a comparative study of PML and Higdon's ABC, found that the Berenger PML cannot absorb evanescent waves, and that under the specific conditions of the paper (analysing waveguide structures) the performance of Higdon and PML for propagation is similar (approximately  $-100$  dB reflection). Higdon's ABC, however, is geometry and mode dependent and numerical stability is difficult to achieve, whereas the PML does not need much tuning in its implementation.

### 6.1.1 PML and UPML (Uniaxial PML)

The original PML as derived by Berenger in 1994 [4], formulated Maxwell's equations by artificially splitting each vector field component into two orthogonal components. Each

of the 12 resulting components is then expressed as satisfying a coupled set of first-order partial differential equations. Loss parameters are chosen such that a perfectly matched planar interface is derived.

Members of the scientific community dislike this hypothetical, non-Maxwellian mathematical model. It is not physical, not intuitive and therefore difficult to implement in other coordinates. Due to the coordinate-dependence of the loss term, it is also anisotropic.

Using Berenger's PML as a starting point, Sacks *et al.* formulated a physical model based on an anisotropic, perfectly matched medium [34] and thus was born the Uniaxial PML. The UPML is based on anisotropic material properties  $(\epsilon, \mu, \sigma)$  rather than split fields to describe the absorbing layer.

When comparing the UPML to the Berenger PML, Sacks found that the results were the same when implemented in a frequency domain Finite Element Method formulation.

Stephen Gedney in [16], was the first to implement the UPML in FDTD where it was found that the UPML and PML results were equivalent within four to five digits ( $-80$  to  $-100$  dB). He also showed that application of the UPML in FDTD is more computationally efficient than the PML.

In [32] and [43], the authors state that the original split-field absorber (otherwise known as the Berenger PML, or just PML), exhibits several difficulties in modelling evanescent waves, such as those in lossy, dielectric media. The first paper [32] also states, without explanation, that the PML is ill-posed under certain perturbations. These perturbations could be due to the fact that the PML does not satisfy Gauss' law ( $\nabla \cdot \vec{D} = 0$ ), but rather satisfies  $\nabla \cdot \vec{E} = 0$  [40]. This implies that the  $E_x$  field, for instance, is continuous across the  $x = 0$  boundary for the PML and that  $D_x$  is continuous across this boundary for the UPML.

Within the UPML, Gauss' Law for the E-field is explicitly written in differential form as shown in equation 6.1. In this equation,  $\bar{s}$  is a diagonal tensor defined in equation 6.12.

$$\nabla \cdot \vec{D} = \nabla \cdot (\epsilon \bar{s} \vec{D}) = \frac{\partial}{\partial x} \left( \epsilon \frac{s_y s_z}{s_x} E_x \right) + \frac{\partial}{\partial y} \left( \epsilon \frac{s_x s_z}{s_y} E_y \right) + \frac{\partial}{\partial z} \left( \epsilon \frac{s_x s_y}{s_z} E_z \right) = 0 \quad (6.1)$$

where

$$\begin{aligned} s_x &= \kappa_x + \frac{\sigma_x}{j\omega\epsilon} \quad \text{etc. and} \\ \epsilon &= \epsilon_0\epsilon_r \end{aligned} \quad (6.2)$$

The definition of  $\kappa$  and  $\sigma$  will become clear in subsequent paragraphs. For now, they can be understood as scaling parameters for the relative permittivity ( $\epsilon_r$ ) and relative permeability ( $\mu_r$ ) of the boundary regions of the structure under analysis.

The corresponding formulation of the divergence equation for the PML is:

$$\nabla \cdot \vec{D} = \frac{1}{s_x} \frac{\partial}{\partial x} (\epsilon E_x) + \frac{1}{s_y} \frac{\partial}{\partial y} (\epsilon E_y) + \frac{1}{s_z} \frac{\partial}{\partial z} (\epsilon E_z) = 0 \quad (6.3)$$

In equation 6.3, the  $\nabla$  operator is defined in a mapped space, which redefines the PML equations in a nonsplit form and maps Maxwell's equations into a complex coordinate space. [40, p29].

As an example, consider a wave travelling across a PML boundary, normally incident at  $x = 0$ . In this UPML region,  $s_y$  and  $s_z$  will be 1 and the value of  $s_x$  is as shown in equation 6.2. (The UPML is uniaxial in this region). The divergence equations simplify to:

$$\nabla \cdot \vec{D} = \nabla \cdot (\epsilon \vec{s} \vec{D}) = \frac{\partial}{\partial x} (\epsilon s_x^{-1} E_x) + \frac{\partial}{\partial y} (\epsilon s_x E_y) + \frac{\partial}{\partial z} (\epsilon s_x E_z) = 0 \quad (\text{UPML}) \quad (6.4)$$

$$\nabla \cdot \vec{D} = \frac{1}{s_x} \frac{\partial}{\partial x} (\epsilon E_x) + \frac{\partial}{\partial y} (\epsilon E_y) + \frac{\partial}{\partial z} (\epsilon E_z) = 0 \quad (\text{PML}) \quad (6.5)$$

In equation 6.4,  $D_x$  and  $s_x^{-1} E_x$  (the normally incident fields) are continuous across  $x = 0$  and in equation 6.5,  $E_x$  and  $D_x$  are continuous because  $\frac{1}{s_x}$  occurs outside the derivative.

The UPML and PML methods both satisfy the wave equations shown in equation 6.6.

$$\begin{aligned} \nabla^2 \vec{E} + \omega^2 \mu \epsilon \vec{E} &= 0 \\ \nabla^2 \vec{H} + \omega^2 \mu \epsilon \vec{H} &= 0 \end{aligned} \quad (6.6)$$

They therefore have the same propagation characteristics, however the  $E$  and  $H$  fields that are normal to the layers (UPML and PML) will differ by a factor of  $s_x$ .

In developing the theory behind the UPML, the references ([40] and [4]), use time-harmonic conditions and thus they assume all signals to be sinusoidal in nature by limiting

the derivation to the sinusoidal steady state. This assumption makes it possible to replace time derivatives with  $j\omega$ . Since a field with general time dependence can be thought of as a linear superposition of fields that vary harmonically in time at different frequencies (as formally described by the Fourier transform), this assumption is reasonable.

In a source free region, under time-harmonic conditions, Maxwell's curl equations are:

$$\nabla \times \vec{\check{E}} = -j\omega\mu\vec{\check{H}} \quad (6.7)$$

$$\nabla \times \vec{\check{H}} = j\omega\epsilon\vec{\check{E}} \quad (6.8)$$

The ‘ $\check{\cdot}$ ’ on the vectors  $\vec{\check{E}}$  and  $\vec{\check{H}}$  indicates time harmonic conditions.

The UPML defines a tensor, which provides for absorbers adjacent to the outer lattice boundary planes, such that equation 6.7 and 6.8 can be written as:

$$\nabla \times \vec{\check{E}} = -j\omega\mu\bar{\bar{s}}\vec{\check{H}} \quad (6.9)$$

$$\nabla \times \vec{\check{H}} = j\omega\epsilon\bar{\bar{s}}\vec{\check{E}} \quad (6.10)$$

where  $\bar{\bar{s}}$  is a diagonal tensor defined by

$$\sigma_{||} = \begin{bmatrix} \frac{1}{s_x} & 0 & 0 \\ 0 & s_x & 0 \\ 0 & 0 & s_x \end{bmatrix} \begin{bmatrix} s_y & 0 & 0 \\ 0 & \frac{1}{s_y} & 0 \\ 0 & 0 & s_y \end{bmatrix} \begin{bmatrix} s_z & 0 & 0 \\ 0 & s_z & 0 \\ 0 & 0 & \frac{1}{s_z} \end{bmatrix} \quad (6.11)$$

$$= \begin{bmatrix} \frac{s_y s_z}{s_x} & 0 & 0 \\ 0 & \frac{s_x s_z}{s_y} & 0 \\ 0 & 0 & \frac{s_x s_y}{s_z} \end{bmatrix} \quad (6.12)$$

and

$$\begin{aligned} s_x &= \kappa_x + \frac{\sigma_x}{j\omega\epsilon} \\ s_y &= \kappa_y + \frac{\sigma_y}{j\omega\epsilon} \\ s_z &= \kappa_z + \frac{\sigma_z}{j\omega\epsilon} \end{aligned} \quad (6.13)$$

Note that the individual matrices in equation 6.11 are uniaxial, where axial symmetry is achieved, for example, around the x-axis, by observing that  $s_{ij} = s_{ji}$  where  $s_{ij}$  and  $s_{ij} \neq s_{11}$  in the first matrix. The resultant matrix (6.12) is therefore not uniaxial anymore but

rather just anisotropic. However, the anisotropic PML is still referenced as uniaxial since it is uniaxial in the non-overlapping PML regions.

$\kappa$  and  $\sigma$  are scaling parameters, which simplify to  $\kappa = 1$  and  $\sigma = 0$  in the non-UPML (or computational domain), such that the tensor reduces to equation 6.14 in this region.

$$\bar{\mathbf{s}} = \begin{bmatrix} 1 & 0 & 0 \\ 0 & 1 & 0 \\ 0 & 0 & 1 \end{bmatrix} \quad (6.14)$$

The profile for  $\kappa$  and  $\sigma$  could be polynomial, geometric or any other gradually increasing gradient. The method chosen in this thesis is polynomial. This choice was arbitrarily made over the choice of geometric grading. These two methods were shown by Berenger to be the most successful in the PML loss profile [6].

Gedney [40, p 306] specifies the polynomial grading of  $\kappa$  and  $\sigma$  in a PML with depth  $d$  in the  $x$ -direction as:

$$\begin{aligned} \sigma_x(x) &= \left(\frac{x}{d}\right)^m \sigma_{x,max} \\ \kappa_x(x) &= 1 + (\kappa_{x,max} - 1) \left(\frac{x}{d}\right)^m \end{aligned} \quad (6.15)$$

Various sources have shown that a value for  $m$  between 3 and 4 is nearly optimal. The value for  $\kappa_{max}$  is usually taken to be 1. In highly elongated structures this value should be increased. This is due to the degraded reflectivity performance for waves impinging on the UPML at highly oblique angles.

$\sigma_{x,max}$  can be determined from a given error estimate [6, 5, 40]. If a desired reflection error  $R(0)$  is specified,  $\sigma_{x,max}$  can be computed from [40, p 306]:

$$\sigma_{x,max} = -\frac{(m+1) \ln[R(0)]}{2\eta d} \quad (6.16)$$

with

$$\begin{aligned} 3 &\leq m \leq 4 \\ \eta &= \sqrt{\mu/\epsilon} \\ d &= \text{physical thickness of UPML region} \end{aligned} \quad (6.17)$$

It has been found that a desired reflection error of  $R(0) = e^{-16}$  is nearly optimal for most applications using a 10 cell thick polynomial-graded PML[16].

### 6.1.2 Implementation of UPML in FDTD

The implementation is twofold; firstly the UPML update equations are derived and then the computer implementation is done. (Refer to [40] and [16] for further details.)

Starting with equation 6.10, Ampere's Law in a matched UPML is expressed in equation 6.18.

$$\begin{bmatrix} \frac{\partial \check{H}_z}{\partial y} & - & \frac{\partial \check{H}_y}{\partial z} \\ \frac{\partial \check{H}_x}{\partial z} & - & \frac{\partial \check{H}_z}{\partial x} \\ \frac{\partial \check{H}_y}{\partial x} & - & \frac{\partial \check{H}_x}{\partial y} \end{bmatrix} = j\omega\epsilon_r\epsilon_0 \begin{bmatrix} \frac{s_y s_z}{s_x} & 0 & 0 \\ 0 & \frac{s_x s_z}{s_y} & 0 \\ 0 & 0 & \frac{s_x s_y}{s_z} \end{bmatrix} \begin{bmatrix} \check{E}_x \\ \check{E}_y \\ \check{E}_z \end{bmatrix} \quad (6.18)$$

The frequency dependent terms can be decoupled by the substitution in equation 6.19.

$$\begin{aligned} \check{D}_x &= \epsilon_r\epsilon_0 \frac{s_z}{s_x} \check{E}_x \\ \check{D}_y &= \epsilon_r\epsilon_0 \frac{s_x}{s_y} \check{E}_y \\ \check{D}_z &= \epsilon_r\epsilon_0 \frac{s_y}{s_z} \check{E}_z \end{aligned} \quad (6.19)$$

and applying the inverse Fourier transform using the identity  $j\omega f(\omega) \longrightarrow \frac{\partial f(t)}{\partial t}$ .

This results in the system of time-domain differential equations shown in equation 6.20.

$$\begin{bmatrix} \frac{\partial \check{H}_z}{\partial y} & - & \frac{\partial \check{H}_y}{\partial z} \\ \frac{\partial \check{H}_x}{\partial z} & - & \frac{\partial \check{H}_z}{\partial x} \\ \frac{\partial \check{H}_y}{\partial x} & - & \frac{\partial \check{H}_x}{\partial y} \end{bmatrix} = \frac{\partial}{\partial t} \begin{bmatrix} \kappa_y & 0 & 0 \\ 0 & \kappa_z & 0 \\ 0 & 0 & \kappa_x \end{bmatrix} \begin{bmatrix} D_x \\ D_y \\ D_z \end{bmatrix} + \frac{1}{\epsilon} \begin{bmatrix} \sigma_y & 0 & 0 \\ 0 & \sigma_z & 0 \\ 0 & 0 & \sigma_x \end{bmatrix} \begin{bmatrix} D_x \\ D_y \\ D_z \end{bmatrix} \quad (6.20)$$

Approximating the time-derivatives using a central difference approximation and averaging  $\vec{D}$  and  $\vec{E}$  in time, results in the second-order accurate explicit update equations that are numerically stable[16]. The approximation and averaging are shown in equation 6.21, where  $A$  is a scalar representing the  $x, y$  or  $z$  coordinate of the fields.

$$\begin{aligned} \frac{\partial A}{\partial t} &= \frac{A^{n+1} - A^n}{\Delta t} \\ A &= \frac{A^{n+1} + A^n}{2} \\ \frac{\partial A}{\partial y} &= \frac{A^{j+\frac{1}{2}} - A^{j-\frac{1}{2}}}{\Delta y} \end{aligned} \quad (6.21)$$

In equation 6.21,  $n$  indicates the current time and  $j$  the current spatial increment.

The frequency dependent terms of equation 6.19 is also implemented using the approximations and averaging in equation 6.21.

As an example,  $E_z$  is implemented from the definition of the electric flux density in equation 6.19 as follows:

$$\begin{aligned} \check{D}_z &= \epsilon_r \epsilon_0 \frac{s_y}{s_z} \check{E}_z \\ \check{D}_z &= \epsilon \frac{\kappa_y + \frac{\sigma_y}{j\omega\epsilon}}{\kappa_z + \frac{\sigma_z}{j\omega\epsilon}} \check{E}_z \\ \left[ \kappa_z + \frac{\sigma_z}{j\omega\epsilon} \right] \check{D}_z &= \epsilon \left[ \kappa_y + \frac{\sigma_y}{j\omega\epsilon} \right] \check{E}_z \\ \epsilon \kappa_z [j\omega \check{D}_z] + \sigma_z \check{D}_z &= \epsilon [\epsilon \kappa_y (j\omega \check{E}_z) + \epsilon \sigma_y \check{E}_z] \end{aligned} \quad (6.22)$$

Applying the inverse Fourier transform and using the approximations in equation 6.21, equation 6.22 becomes

$$\begin{aligned} \epsilon \kappa_z \frac{\partial}{\partial t} [D_z] + \sigma_z D_z &= \epsilon \left( \epsilon \kappa_y \frac{\partial}{\partial t} [E_z] + \epsilon \sigma_y E_z \right) \\ \frac{\epsilon \kappa_z}{\Delta t} [D_z^{n+1} - D_z^n] + \frac{\sigma_z}{2} [D_z^{n+1} + D_z^n] &= \epsilon \left( \frac{\epsilon \kappa_y}{\Delta t} [E_z^{n+1} - E_z^n] + \frac{\sigma_y}{2} [E_z^{n+1} + E_z^n] \right) \end{aligned} \quad (6.23)$$

$E_z$  and  $D_z$  are time domain signals found after applying the inverse Fourier transform to the frequency domain signals  $\check{E}_z$  and  $\check{D}_z$ .

Rearranging the terms in equation 6.23, results in the update equation for  $E_z$ :

$$E_z^{n+1} = \left[ \frac{2\epsilon\kappa_y - \sigma_y\Delta t}{2\epsilon\kappa_y + \sigma_y\Delta t} \right] E_z^n + \frac{1}{\epsilon} \left[ \frac{2\epsilon\kappa_z + \Delta t\sigma_z}{2\epsilon\kappa_y + \sigma_y\Delta t} \right] D_z^{n+1} - \frac{1}{\epsilon} \left[ \frac{2\epsilon\kappa_z - \sigma_z\Delta t}{2\epsilon\kappa_y + \sigma_y\Delta t} \right] D_z^n \quad (6.24)$$

In further derivations, reference will be made to the spatial point  $(i, j, k)$ . In a rectangular lattice, this refers to:

$$(i, j, k) = (i\Delta x, j\Delta y, k\Delta z) \quad (6.25)$$

where  $\Delta x, \Delta y$  and  $\Delta z$  are respectively, the lattice space increments in the  $x, y$  and  $z$  coordinate directions, and  $i, j$  and  $k$  are integers.

Before presenting these, the position of each field component needs to be described. K.S. Yee suggested a cubic unit cell for the positioning of the electric and magnetic field vector components. (Refer to Figure 6.1) :

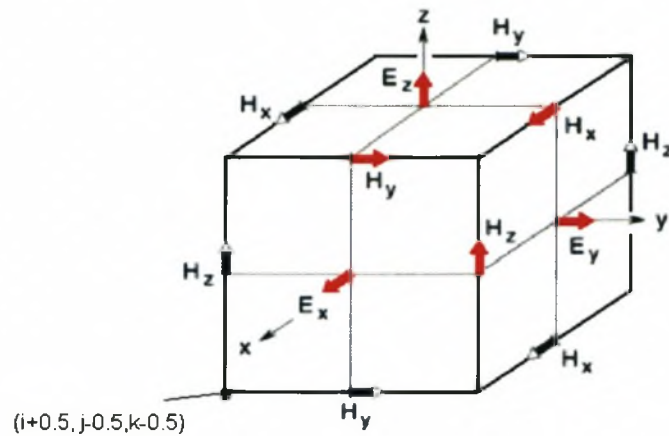


**Figure 6.1:** Magnetic and Electric Field Vector Positioning on the Yee Cell ([40] and [44])

From Figure 6.1, the physical positions of the field coordinates of the fundamental cell are expressed in table 6.1 (assuming the origin is at the centre of the cube).

**Table 6.1:** Location of the Fundamental Field Coordinates in the Yee-Cell

<i>Field Coordinate</i>	<i>Fundamental Location</i>
$E_x$	$(i + \frac{1}{2}, j, k)$
$E_y$	$(i, j + \frac{1}{2}, k)$
$E_z$	$(i, j, k + \frac{1}{2})$
$H_x$	$(i, j + \frac{1}{2}, k + \frac{1}{2})$
$H_y$	$(i + \frac{1}{2}, j, k + \frac{1}{2})$
$H_z$	$(i + \frac{1}{2}, j + \frac{1}{2}, k)$

Using the above derivation, the fields are found and summarised in equation set 6.26.

$$\begin{aligned}
D_x \Big|_{(i+\frac{1}{2},j,k)}^{n+1} &= \frac{2\epsilon\kappa_y - \sigma_y\Delta t}{2\epsilon\kappa_y + \sigma_y\Delta t} D_x \Big|_{(i+\frac{1}{2},j,k)}^n + \frac{2\epsilon\Delta t}{2\epsilon\kappa_y + \sigma_y\Delta t} \\
&\cdot \left[ \frac{H_z \Big|_{(i+\frac{1}{2},j+\frac{1}{2},k)}^{n+\frac{1}{2}} - H_z \Big|_{(i+\frac{1}{2},j-\frac{1}{2},k)}^{n+\frac{1}{2}}}{\Delta y} - \frac{H_y \Big|_{(i+\frac{1}{2},j,k+\frac{1}{2})}^{n+\frac{1}{2}} - H_y \Big|_{(i+\frac{1}{2},j,k-\frac{1}{2})}^{n+\frac{1}{2}}}{\Delta z} \right] \\
E_x \Big|_{(i+\frac{1}{2},j,k)}^{n+1} &= \frac{2\epsilon\kappa_z - \sigma_z\Delta t}{2\epsilon\kappa_z + \sigma_z\Delta t} E_x \Big|_{(i+\frac{1}{2},j,k)}^n + \frac{1}{\epsilon(2\epsilon\kappa_z + \sigma_z\Delta t)} \\
&\cdot \left[ (2\epsilon\kappa_x + \Delta t\sigma_x) D_x \Big|_{(i+\frac{1}{2},j,k)}^{n+1} - (2\epsilon\kappa_x - \Delta t\sigma_x) D_x \Big|_{(i+\frac{1}{2},j,k)}^n \right] \\
D_y \Big|_{(i,j+\frac{1}{2},k)}^{n+1} &= \frac{2\epsilon\kappa_z - \sigma_z\Delta t}{2\epsilon\kappa_z + \sigma_z\Delta t} D_y \Big|_{(i,j+\frac{1}{2},k)}^n + \frac{2\epsilon\Delta t}{2\epsilon\kappa_z + \sigma_z\Delta t} \\
&\cdot \left[ \frac{H_x \Big|_{(i,j+\frac{1}{2},k+\frac{1}{2})}^{n+\frac{1}{2}} - H_x \Big|_{(i,j+\frac{1}{2},k-\frac{1}{2})}^{n+\frac{1}{2}}}{\Delta z} - \frac{H_z \Big|_{(i+\frac{1}{2},j+\frac{1}{2},k)}^{n+\frac{1}{2}} - H_z \Big|_{(i-\frac{1}{2},j+\frac{1}{2},k)}^{n+\frac{1}{2}}}{\Delta x} \right] \\
E_y \Big|_{(i,j+\frac{1}{2},k)}^{n+1} &= \frac{2\epsilon\kappa_x - \sigma_x\Delta t}{2\epsilon\kappa_x + \sigma_x\Delta t} E_y \Big|_{(i,j+\frac{1}{2},k)}^n + \frac{1}{\epsilon(2\epsilon\kappa_x + \sigma_x\Delta t)} \\
&\cdot \left[ (2\epsilon\kappa_y + \Delta t\sigma_y) D_y \Big|_{(i,j+\frac{1}{2},k)}^{n+1} - (2\epsilon\kappa_y - \Delta t\sigma_y) D_y \Big|_{(i,j+\frac{1}{2},k)}^n \right] \\
D_z \Big|_{(i,j,k+\frac{1}{2})}^{n+1} &= \frac{2\epsilon\kappa_x - \sigma_x\Delta t}{2\epsilon\kappa_x + \sigma_x\Delta t} D_z \Big|_{(i,j,k+\frac{1}{2})}^n + \frac{2\epsilon\Delta t}{2\epsilon\kappa_x + \sigma_x\Delta t} \\
&\cdot \left[ \frac{H_y \Big|_{(i+\frac{1}{2},j,k+\frac{1}{2})}^{n+\frac{1}{2}} - H_y \Big|_{(i-\frac{1}{2},j,k+\frac{1}{2})}^{n+\frac{1}{2}}}{\Delta x} - \frac{H_x \Big|_{(i,j+\frac{1}{2},k+\frac{1}{2})}^{n+\frac{1}{2}} - H_x \Big|_{(i,j-\frac{1}{2},k+\frac{1}{2})}^{n+\frac{1}{2}}}{\Delta y} \right] \\
E_z \Big|_{(i,j,k+\frac{1}{2})}^{n+1} &= \frac{2\epsilon\kappa_y - \sigma_y\Delta t}{2\epsilon\kappa_y + \sigma_y\Delta t} E_z \Big|_{(i,j,k+\frac{1}{2})}^n + \frac{1}{\epsilon(2\epsilon\kappa_y + \sigma_y\Delta t)} \\
&\cdot \left[ (2\epsilon\kappa_z + \Delta t\sigma_z) D_z \Big|_{(i,j,k+\frac{1}{2})}^{n+1} - (2\epsilon\kappa_z - \Delta t\sigma_z) D_z \Big|_{(i,j,k+\frac{1}{2})}^n \right]
\end{aligned} \tag{6.26}$$

The corresponding magnetic fields are summarised in appendix B.1.

The fields in equation set 6.26, are located on non-integer coordinates, which cannot be implemented conveniently on a PC. A simple renumbering makes it possible to implement

the fields on an integer grid. (Note that this is just for programming convenience, the actual field positions retain the  $\frac{1}{2}$ -step offset where necessary.)

$$\begin{aligned}
 n + \frac{1}{2} &\Rightarrow n & n - \frac{1}{2} &\Rightarrow n - 1 \\
 i + \frac{1}{2} &\Rightarrow i & i - \frac{1}{2} &\Rightarrow i - 1 \\
 j + \frac{1}{2} &\Rightarrow j & j - \frac{1}{2} &\Rightarrow j - 1 \\
 k + \frac{1}{2} &\Rightarrow k & k - \frac{1}{2} &\Rightarrow k - 1
 \end{aligned} \tag{6.27}$$

Further simplification of the equations can be achieved by defining the variables in equation set 6.28.

$$\begin{aligned}
 CAX &= \frac{2\epsilon\kappa_x - \sigma_x\Delta t}{2\epsilon\kappa_x + \sigma_x\Delta t} \\
 CAY &= \frac{2\epsilon\kappa_y - \sigma_y\Delta t}{2\epsilon\kappa_y + \sigma_y\Delta t} \\
 CAZ &= \frac{2\epsilon\kappa_z - \sigma_z\Delta t}{2\epsilon\kappa_z + \sigma_z\Delta t} \\
 CBX &= \frac{1}{2\epsilon\kappa_x + \sigma_x\Delta t} \\
 CBY &= \frac{1}{2\epsilon\kappa_y + \sigma_y\Delta t} \\
 CBZ &= \frac{1}{2\epsilon\kappa_z + \sigma_z\Delta t}
 \end{aligned} \tag{6.28}$$

The computer ready E-field equations have a new position coordinate and are shown in equation set 6.29.

$$\begin{aligned}
 D_x|_{(i,j,k)}^{n+1} &= CAY \cdot D_x|_{(i,j,k)}^n + CBY \cdot 2\epsilon\Delta t \\
 &\cdot \left[ \frac{H_z|_{(i,j,k)}^n - H_z|_{(i,j-1,k)}^n}{\Delta y} - \frac{H_y|_{(i,j,k)}^n - H_y|_{(i,j,k-1)}^n}{\Delta z} \right] \\
 E_x|_{(i,j,k)}^{n+1} &= CAZ \cdot E_x|_{(i,j,k)}^n + CBZ \cdot \frac{1}{\epsilon} \\
 &\cdot \left[ (2\epsilon\kappa_x + \Delta t\sigma_x)D_x|_{(i,j,k)}^{n+1} - (2\epsilon\kappa_x - \Delta t\sigma_x)D_x|_{(i,j,k)}^n \right]
 \end{aligned}$$

$$\begin{aligned}
D_y|_{(i,j,k)}^{n+1} &= CAZ \cdot D_y|_{(i,j,k)}^n + CBZ \cdot 2\epsilon\Delta t \\
&\cdot \left[ \frac{H_x|_{(i,j,k)}^n - H_x|_{(i,j,k-1)}^n}{\Delta z} - \frac{H_z|_{(i,j,k)}^n - H_z|_{(i-1,j,k)}^n}{\Delta x} \right] \\
E_y|_{(i,j,k)}^{n+1} &= CAX \cdot E_y|_{(i,j,k)}^n + CBX \cdot \frac{1}{\epsilon} \\
&\cdot \left[ (2\epsilon\kappa_y + \Delta t\sigma_y)D_y|_{(i,j,k)}^{n+1} - (2\epsilon\kappa_y - \Delta t\sigma_y)D_y|_{(i,j,k)}^n \right] \\
D_z|_{(i,j,k)}^{n+1} &= CAX \cdot D_z|_{(i,j,k)}^n + CBX \cdot 2\epsilon\Delta t \\
&\cdot \left[ \frac{H_y|_{(i,j,k)}^n - H_y|_{(i-1,j,k)}^n}{\Delta x} - \frac{H_x|_{(i,j,k)}^n - H_x|_{(i,j-1,k)}^n}{\Delta y} \right] \\
E_z|_{(i,j,k)}^{n+1} &= CAY \cdot E_z|_{(i,j,k)}^n + CBY \cdot \frac{1}{\epsilon} \\
&\cdot \left[ (2\epsilon\kappa_z + \Delta t\sigma_z)D_z|_{(i,j,k)}^{n+1} - (2\epsilon\kappa_z - \Delta t\sigma_z)D_z|_{(i,j,k)}^n \right]
\end{aligned} \tag{6.29}$$

Refer to appendix B.2 for all magnetic field equations.

Implementation of the UPML in the whole domain, requires definition of 27 regions. (Refer to Figure 6.2.)

The update equations as defined in equation set 6.29 are updated in all regions; however, the  $\kappa$  and  $\sigma$  coefficients depend on the region. For instance,  $\sigma_x$ , is a coefficient that increases polynomially from zero in the normal update region (region 14 in Figure 6.2) to a certain defined maximum value. The increase is only along the x-axis.  $\sigma_x$  stays zero along the y and z axes. For a complete summary of the various cases in all regions, refer to [40, p303].

The box containing the 27 regions is terminated on the outside with PEC's. This is achieved by adhering to boundary conditions on PEC's:

$$\vec{n} \times \vec{E} = 0 \tag{6.30}$$

To illustrate, refer to the update equation for  $E_x$ , given below for easy reference and

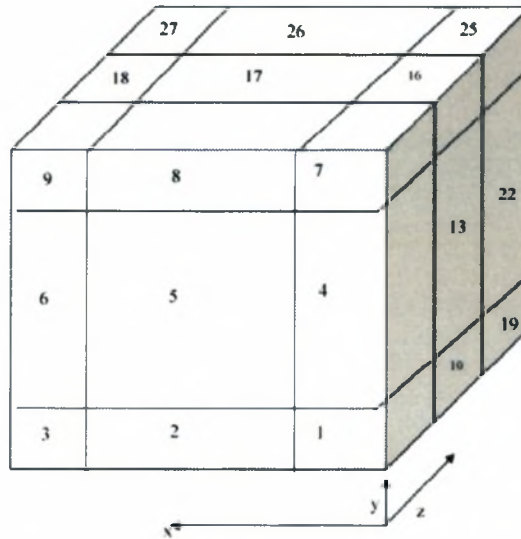


**Figure 6.2:** UPML Regions Required in Full 3D Evaluation.

simplified to two dimensions for the purpose of illustration:

$$D_x \Big|_{(i+\frac{1}{2},j)}^{n+1} = \frac{2\epsilon\kappa_y - \sigma_y\Delta t}{2\epsilon\kappa_y + \sigma_y\Delta t} D_x \Big|_{(i+\frac{1}{2},j)}^n - \frac{2\epsilon\Delta t}{2\epsilon\kappa_y + \sigma_y\Delta t} \cdot \left[ \frac{H_y \Big|_{(i+\frac{1}{2},j)}^{n+\frac{1}{2}} - H_y \Big|_{(i+\frac{1}{2},j)}^{n-\frac{1}{2}}}{\Delta z} \right] \tag{6.31}$$

In Region 2,  $\sigma_y$  should increase from zero (at the intersection with region 5) to a maximum calculated value. For purposes of illustration,  $\sigma_{max}$  will be taken as 2 in Figure 6.3.

Figure 6.3 shows an X-Y view of region 2, where region 2 consists of  $3 \times 3 = 9$  cells. In equation 6.31,  $D_x$  is defined at  $x = i + \frac{1}{2}$  and  $y = j$ . The physical location (according to the Yee cell), is thus indicated with a blue arrow.  $\sigma_y$ 's value has to be calculated at this physical location.

A computer stores values only at integer positions in a matrix (such as is indicated with a red dot). Since the physical update position is of prime importance, the value calculated at  $(i + \frac{1}{2}, j)$  is stored at location  $(i, j)$ .

In the x-direction, the physical and computer positions differ by 0.5. In this example, the

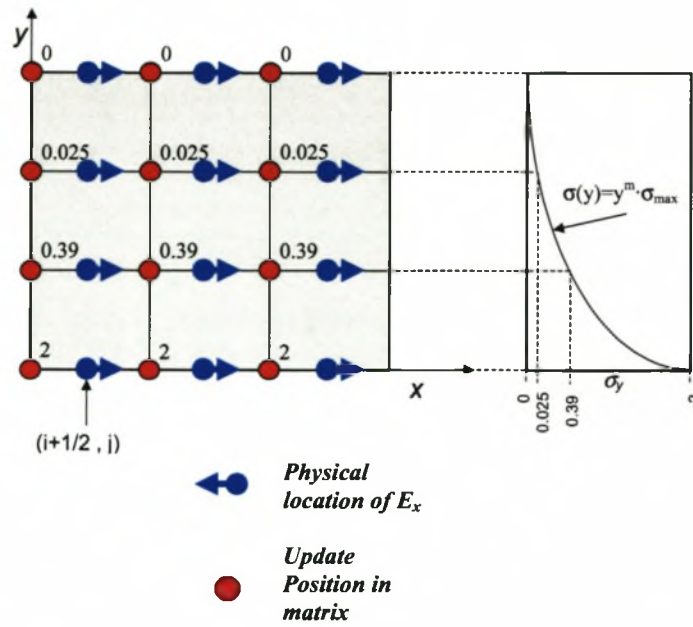


**Figure 6.3:** Location of  $\sigma_x$  when Calculating  $D_x$  and  $E_x$  in Region 2

profile of  $\sigma_y$  only changes in the y-direction and is constant in the x-direction.

### 6.1.3 Results

Initial tests were done using a Gaussian derivative soft source [13] centered in a lattice. A reference of lattice size  $101 \times 101 \times 101$ , terminated with a 10 cell UPML was used, and compared with results obtained using an  $11 \times 11 \times 11$  lattice (with 10 cell UPML). The reference lattice had to be significantly larger than the test lattice, so that reflections from the UPML boundaries introduced by the reference would be minimised. The reference used more memory than was available and had to use swap space on the hard drive. The free memory required for the reference calculation was  $(101 + (2 \times 10))^3$  cells  $\times$  8 bytes  $\times$  54 matrices  $\approx$  765 MB.

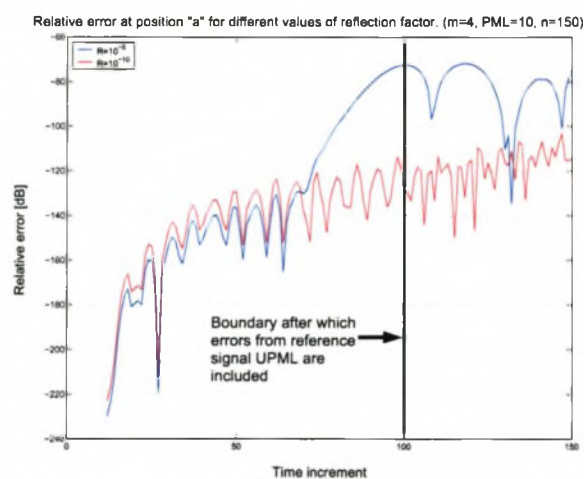


**Figure 6.4:** Relative Errors Obtained with Different Values of Reflection Factor,  $R$ . (UPML = 10 cells,  $m=4$ )

Figure 6.4 shows the relative error obtained with the described set-up when the reflection factor was adjusted from  $R = 10^{-5}$  to  $R = 10^{-10}$ . Adjusting the reflection factor had the effect of changing  $\sigma_{max}$  from 6 to approximately 2. The boundary shown indicates that a centered reference signal will take at least 101 time steps to travel from the centre of the lattice, to the UPML region and back to the centre, after which it will affect the signal at the centre. If the observation points are located elsewhere, the influence from the reference will be noticed earlier. <sup>1</sup>

<sup>1</sup>Since the errors caused by reflection from the UPML are cumulative, it is imperative that the reference lattice be as large as possible so that reflections caused by the reference UPML do not affect the test.

The relationship between  $\sigma_{max}$  and  $R$  was shown in equation 6.16.

To put these results in context, it is necessary to relate them to the literature. No literature could be found on 3-D UPML with a source centered in an empty lattice. However, related literature revealed that the reflections obtained in the example was typical of UPML performance. This literature is briefly discussed below.

**UPML and Non-Homogeneous Media**[16] Gedney implemented both stripline and microstrip in a 3-D UPML terminated FDTD region. In all cases a grading parameter of  $m = 4$  was found to be optimum. By varying  $\sigma$ , he found consistently that the reflection error is below  $-100$  dB for frequencies up to 50 GHz.

**UPML and Lossy and Dispersive Media** [17] It has been shown that Berenger's PML method has difficulties in modelling evanescent fields [14] and [17], however, Gedney shows in this article that a waveguide terminated with a 10 cell UPML and excited with a  $TE_{10}$  mode can have a reflection error as low as  $-100$  dB up to frequencies of 50 GHz.

**UPML and Berenger PML** Since a direct comparison with published results was not possible, a comparative study was done on similarities in results of PML and UPML.

Berenger in [7] and Gedney in [17] show that UPML and Berenger PML are the same up to the 5<sup>th</sup> decimal place ( $-100$  dB). Gedney did a comparison of reflection error against frequency for PML and UPML when terminating a stripline with a 10-cell thick Matched Layer. The test was done for all frequencies up to 40 GHz and exactly the same reflection error was obtained with both methods. This reflection error was between  $-80$  dB and  $-100$  dB.

These papers show that under their specific conditions it is reasonable to expect that results obtained with UPML (if above  $-100$  dB) are as good as those obtained with Berenger PML. The assumption was thus made (though not proven) that this relationship will be valid for any homogeneous, lossless, non-dispersive region.

Gedney demonstrated in [40, p317] the implementation of a 3-D Berenger PML, using a hard source excitation centered in a lattice of air. He chose a 16 cell PML layer and

simulated 100 time steps. The results are presented in the form of a ‘local error’<sup>2</sup>, which is defined as:

$$e_{local} |_{i,j,k}^n = E_{z,T} |_{i,j,k}^n - E_{z,B} |_{i,j,k}^n \quad (6.32)$$

where  $E_{z,B}$  is a reference signal simulating the ideal of an infinitely large FDTD grid during tests and  $E_{z,T}$  is the test signal in a 100x100x50 domain.

The source used in the example is a Hertzian dipole hard source, which is a single  $E_z$  field component centered in a lattice with  $\epsilon_r=1$ . This source is a smooth compact pulse peaking at  $n=20$  time-steps with a value of 1 and has the mathematical description of:

$$E_z |_{center\ of\ lattice}^n = \frac{1}{32} \cdot [10 - 15 \cos(\pi n/20) + 6 \cos(2\pi n/20) - \cos(3\pi n/20)] \quad n \leq 40 \quad (6.33)$$

The source is graphically illustrated in Figure 6.5.

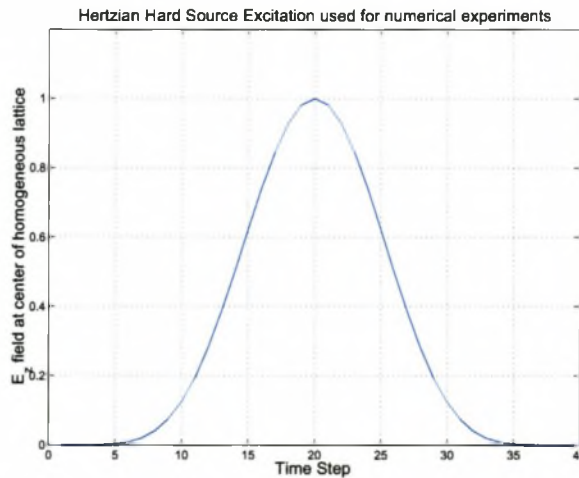


**Figure 6.5:** Hertzian Hard Source used for Numerical Experiments

It was not possible to duplicate this result exactly, due to the demands on resources. The

<sup>2</sup>Defining a local error such as was used in this example does not seem useful as no frame of reference is defined. It makes more sense to define a relative error such as was used in the other examples as it is normalised and therefore referenced

test case would require 994 MB of memory.

$$\begin{aligned}
 (100 + 2 \cdot 16) \times (100 + 2 \cdot 16) \times (100 + 2 \cdot 16) & \text{ cells} \\
 \times 8 & \text{ bytes of memory} \\
 \times 54 & \text{ fields} \\
 \approx 994 \text{ MB} & \tag{6.34}
 \end{aligned}$$

The reference would need 2.6 Gb of free memory to execute.

$$\begin{aligned}
 (150 + 2 \cdot 16) \times (150 + 2 \cdot 16) \times (150 + 2 \cdot 16) & \text{ cells} \\
 \times 8 & \text{ bytes of memory} \\
 \times 54 & \text{ fields} \\
 \approx 2.6 \text{ Gb} & \tag{6.35}
 \end{aligned}$$

The resources available were limited to 770 MB RAM.

The example was used with a smaller computational domain, while using the same hard source.

A Hertzian hard-sourced  $E_z$  field component is centered in a lattice of size 101x101x101. This update region is completely enveloped by a 5-cell UPML, making the dimensions of the total lattice 106x106x106 cells. The signal thus obtained was used as a reference. It was allowed to run for 75 time-steps after which it was compared with results using a lattice size (excluding the 16-cell UPML) of 11x11x11. (The 75 time steps were chosen to be less than 100, which is the time it would take the initial signal to reach the UPML region and be reflected back to the origin.) In both cases, the source will be centered in the lattice and observed at 2 positions. Positions 'a' and 'b' are placed one cell away from the PML region as shown below in Figure 6.6 (Note that the observation points are centered in the z-direction):

In Figure 6.7, it is seen that the local error is dramatically lower than the relative error (Figure 6.4). The local error in Figure 6.7 is approximately  $-180$  dB compared to the  $-100$  dB of the relative error shown in Figure 6.4. The reason for this is that a local error is defined as a difference in values, whereas the relative error normalizes this difference to the maximum value that the reference signal experience at that point.

Gedney obtained a result of  $-175$  dB at a similar point in his example. Even though the experiment described above was not identical to the example presented by Gedney, there was such agreement in results when comparable points were investigated, that the results

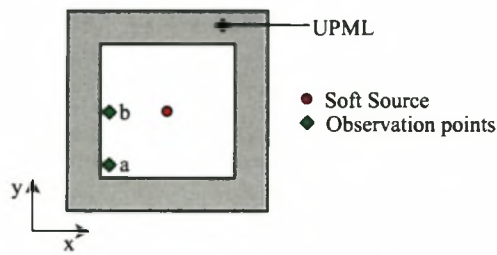


**Figure 6.6:** Position of Observation Points in Experiments

shown in Figure 6.7 was taken to be acceptable and correct.

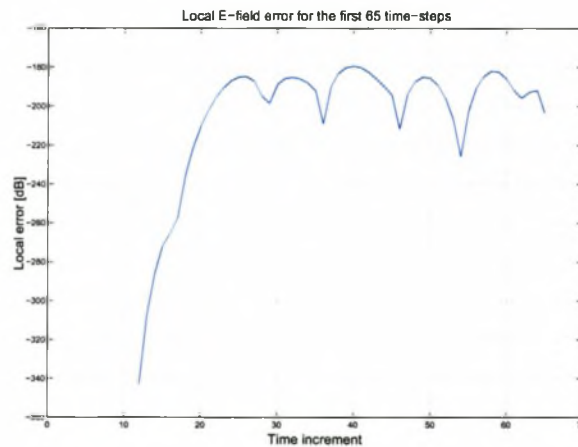


**Figure 6.7:** Local E-field Error at Different Time Steps at a Location which is Centered on the  $z$ -axis at the Outer Boundary of an  $11 \times 11 \times 11$  Test Lattice, used for Comparison with Documented Results

## 6.2 Implementing the Devices into the FDTD Code

The FDTD code was written in Matlab version 6.0.0.88 Release 12. The processor used was an AMD Athlon 1 GHz processor. The computer had 770 MB RAM and the operating system was Microsoft Windows 2000 version 5.00.2195 with service pack 2 installed.

A Matlab file, custom written by a third party was used to generate the mesh from data extracted from AutoCAD.

**Coding Choices and Resulting Tradeoffs** The choices made during implementation of the UPML code are summarised in table 6.2.

**Table 6.2:** Coding Tradeoffs

<i>Choices</i>	<i>Alternative</i>	<i>Pros</i>	<i>Cons</i>
Global application of UPML	Local application	Simplicity, reduced coding time	Increased execution time, more memory
Coefficient calculations at execution time and stored in memory	Coefficient calculation at every iteration	Decreased execution time	More memory

A global application of the UPML over the full domain (computational plus UPML) and not only at the boundaries was chosen over a local application of UPML. This choice greatly simplified the coding and thus development time. However, this choice, coupled with the fact that coefficients are stored in memory at all times, resulted in a need for 54 full matrices to contain the UPML field components. These matrices are identified in table 6.3.

$\kappa$  and  $\sigma$  are the scaling coefficients. Due to the non-symmetrical location of the fields on the fundamental Yee-cell, the scaling parameters differ for each field.

Thus, ignoring smaller matrices and variables, there is a need for at least 54 full sized matrices.

**Ports** An accurate model of the coupler would include ports in the form of cylindrical connectors of characteristic impedance  $50 \Omega$ . However, as the developed software is still

**Table 6.3:** Allocation of Matrices

<i>Matrix Data</i>	<i>Number of matrices re-quired</i>
$E_{x,y,z}$	3
$D_{x,y,z}$	3
$H_{x,y,z}$	3
$B_{x,y,z}$	3
$D_{x,y,z}$ (previous time step)	3
$B_{x,y,z}$ (previous time step)	3
$\kappa_x$ (6 fields)	6
$\kappa_y$ (6 fields)	6
$\kappa_z$ (6 fields)	6
$\sigma_x$ (6 fields)	6
$\sigma_y$ (6 fields)	6
$\sigma_z$ (6 fields)	6

in an experimental stage, the grid is limited to a uniform cubic mesh and cannot perform the cylindrical meshing required for such an implementation.

To overcome this inherent limitation in the experimental software, the ports were implemented as infinite  $50 \Omega$  striplines. The infinite striplines were simulated by terminating finite  $50 \Omega$  lines in a 10 cell UPML.

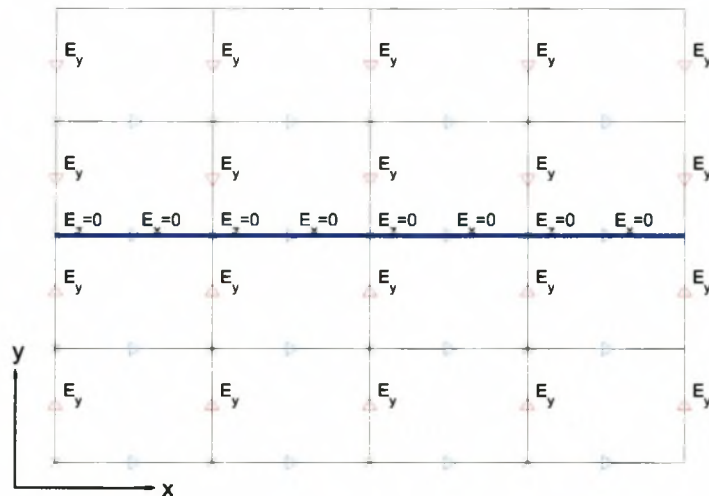


**Figure 6.8:** Cross Section of  $50 \Omega$  port (Excitation Plane) with Locations of Excitation Fields Indicated

**Excitation** To simulate the behaviour of a stripline launcher, a uniform  $E_y$ -field is applied below and above the conductor and the ground planes at port 1 at the  $50 \Omega$  line. (This is referred to as the excitation plane). The excitation plane is graphically illustrated in Figure 6.8. For simplicity, only two rows of cells are shown below and above the  $50 \Omega$  line.

The physical field positions are indicated with arrows. The red, vertically pointed arrows indicate the direction of the  $E_y$ -field. Above the  $50 \Omega$  line, the E-field points downwards in the direction of the line and below the line, the field points upwards.

The FDTD structure is excited in the excitation plane with a soft source in the form of a Gaussian derivative pulse, chosen for its broadband properties.

**Conductor** The conductor is implemented by applying Faraday's continuity condition,  $\vec{n} \times \vec{E} = 0$ , to an infinitely thin layer. As the coupler lies in the X-Z plane, this implies that  $E_x$  and  $E_z$  must be set to zero on each node that lies on the conductor. (Refer to figure 6.8.)

The physical coupler is housed in a metal box. The boundary conditions thus imply that the tangential E-fields on these boundaries be set to zero. The metal plate required at the ports should have round holes for the connectors. As the connectors were not simulated as cylindrical, the metal plates were completely left out at these two faces.

**Location of Measurement Plane** Higher order modes will be excited near the source plane, since this plane represents a discontinuity in the fields. A simple method to exclude these evanescent waves from the calculation, is to move the measurement plane away from the source plane. This is common practice in microwave engineering and the S-Parameters can be calculated using the transmission line formula. The formula for  $S_{11}$  is then as shown in equation 6.36.

$$S_{11}(f, z) = \frac{V_{ref}(f, z' = l)}{V_{inc}(f, z' = l)} \cdot e^{-2j\beta l} \quad (6.36)$$

In equation 6.36,  $z$  refers to the actual position of excitation and  $z'$  refers to the shifted position of the observation plane.

**Calculating S-Parameters** The voltages measured at the ports of the FDTD computational domain include incident and reflected voltages. In such a system, the following voltages can be defined:

$$\begin{aligned}
 V_1 &= V_{1i} + V_{1r} \\
 V_2 &= V_{2i} + V_{2r} \\
 I_1 &= I_{1i} - I_{1r} \\
 I_2 &= I_{2i} - I_{2r}
 \end{aligned} \tag{6.37}$$

The voltages can be expressed in terms of the currents:

$$\begin{aligned}
 V_{1i} &= R_s I_{1i} \\
 V_{1r} &= R_s I_{1r} \\
 V_{2i} &= R_l I_{2i} \\
 V_{2r} &= R_l I_{2r}
 \end{aligned} \tag{6.38}$$

In equation 6.37 and 6.38, ‘*i*’ refers to an incident voltage or current and ‘*r*’ refers to a reflected voltage or current.  $V_1$  and  $V_2$  are the voltages calculated with the FDTD code, with  $V_1$  being the input port.  $R_s$  and  $R_l$  are the source and load resistances. These impedances are both  $50 \Omega$ .

At port 1, an incident wave,  $a_1 = \frac{V_{1i}}{\sqrt{R_s}}$ , and a reflected wave,  $b_1 = \frac{V_{1r}}{\sqrt{R_s}}$  are defined.

Using this terminology, the reflected voltage wave at port 2, can be written in terms of the total voltage measured at port 2.

$$\begin{aligned}
 b_2 &= \frac{V_{2r}}{\sqrt{R_l}} \\
 &= \frac{V_2 - R_l I_2}{2\sqrt{R_l}}
 \end{aligned} \tag{6.39}$$

The incident wave at port 1 can be written in terms of the voltage measured at port 1.

$$\begin{aligned}
 a_1 &= \frac{V_{1i}}{\sqrt{R_s}} \\
 &= \frac{V_1 - R_s I_1}{2\sqrt{R_s}}
 \end{aligned} \tag{6.40}$$

$S_{21}$  is defined when port 2 is terminated in a matched load, ie  $a_2 = 0$ .

Furthermore, the voltage and current measured at port 1 can be written in terms of the applied voltage.

$$\begin{aligned} V_1 &= \frac{Z_{in} E_g}{Z_{in} + R_g} \\ I_1 &= \frac{E_g}{Z_{in} + R_g} \end{aligned} \quad (6.41)$$

$Z_{in}$  is the input impedance of the device.

Combining all these, the S-parameters relating to power transfer to output ports are found.

$$\begin{aligned} S_{21} &= S_{12} = \frac{2V_2}{E_g} \\ S_{31} &= S_{13} = \frac{2V_3}{E_g} \\ S_{41} &= S_{14} = \frac{2V_4}{E_g} \end{aligned} \quad (6.42)$$

The rest of the S-Parameters (excluding  $S_{ii}$ ), are defined in a similar way, but would require excitation at the other ports. Due to long simulation times, this was not implemented.

As the FDTD simulation calculates the sum of the incident and reflected waveforms, another analysis is needed for calculation of  $S_{ii}$ . To obtain an incident waveform, an analysis is done using a straight stripline, which has the same cross-sectional dimensions as the actual device, but it should be of infinite extent (i.e. be absorbed on the far end by the UPML). The incident waveform thus obtained is subtracted from the incident plus reflected signal obtained from analysis of the device. [30] [36]

The calculation for  $S_{11}$  can be summarised as shown in equation 6.43.

$$S_{11} = \frac{V_1 - V_1^{ref}}{V_1^{ref}} \quad (6.43)$$

$V_1^{ref}$  is the reference calculated using the infinite stripline.

### 6.2.1 Wilkinson Divider

The Wilkinson divider was implemented to test the accuracy of the experimental FDTD software. As the aim was to analyse the high frequency coupler, which is a pure stripline configurations, the model of the Wilkinson divider was slightly altered. The microstrip configuration was changed to stripline; resulting in a configuration with an effective dielectric constant of 1.95. As isolation would not be calculated, the resistors were excluded from the simulations as well.

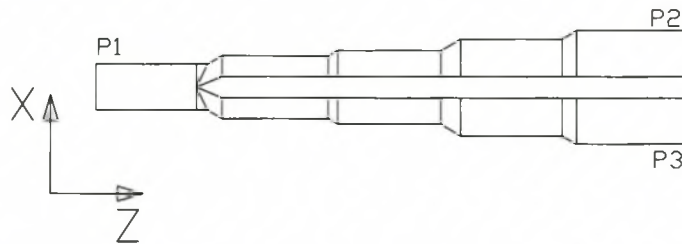


**Figure 6.9:** The Wilkinson Divider Model Used for Comparing own FDTD with MWO Results

The divider model and the definition of the axes are shown in Figure 6.9. The size of the computational domain was chosen such that higher order modes were minimised. However, the width of the divider is unavoidably such that the cut-off frequency of the  $TE_{10}$  mode is at 13.6 GHz, which is still in the passband.

A TEM field is applied at port 1, in the form of a  $y$ -directed electric field. The location of this field is in the X-Y plane, 2 cells away from the UPML in the computational domain. A Gaussian derivative soft source was used as excitation.

The grid-size was limited by the available RAM and time per simulation. The size of the resultant matrices is  $31 \times 74 \times 285$ , requiring approximately 282 MB of free memory to execute. This excludes the 110 MB of memory required by the operating system and for the functioning of Matlab. Each simulation consisted of 2000 time steps and ran for approximately 12 hours.

A uniform mesh was used, effectively dividing the computational domain into sections of size  $\Delta S = 0.112$  mm. This size was chosen for accurate representation of the physical device. The argument for this grid size is similar to that explained in detail in chapter 3.5.1.

For numerical stability,  $\Delta S$  and  $\Delta T$  are related through the FDTD stability equation in equation 6.44.

$$\Delta T = \frac{\sqrt{\epsilon_r} \Delta S}{c\sqrt{3}} \quad (6.44)$$

The relationship  $S = \frac{c\Delta T}{\Delta S}$  is known as the Courant number. For numerical stability in 3D FDTD,  $S$  must be chosen as  $\frac{1}{\sqrt{3}}$ . As the Courant number is derived from the generalised dispersion relation for full-vector-field Yee algorithms [40, p 113], using this number will ensure that the numerical wave will undergo no non-physical attenuation while propagating in the grid.

The resultant time step,  $\Delta T$ , is 29.85 pS. This time step is very small, but a necessity for numerical stability. The frequency resolution obtained from this time domain data, is limited. For 2000 time steps, the resolution is  $\frac{1}{\Delta T \cdot 2000} = 1.68$  GHz.

The results obtained from this implementation were compared to similar results simulated by MWO. Note that in both analyses, the loss was taken to be zero. Under this condition, power division should be equal at ports 2 and 3, and should be  $-3$  dB. The results are shown in Figure 6.10.

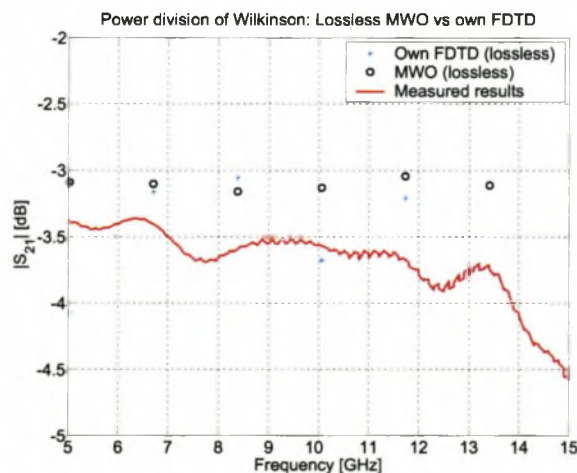


**Figure 6.10:**  $|S_{21}|$  of Wilkinson Divider Calculated Using own FDTD code and Compared with MWO and Measured Results

Since the Wilkinson divider is symmetrical,  $S_{31}$  is equal to  $S_{21}$ . This was observed in the results but it is not shown in Figure 6.10.

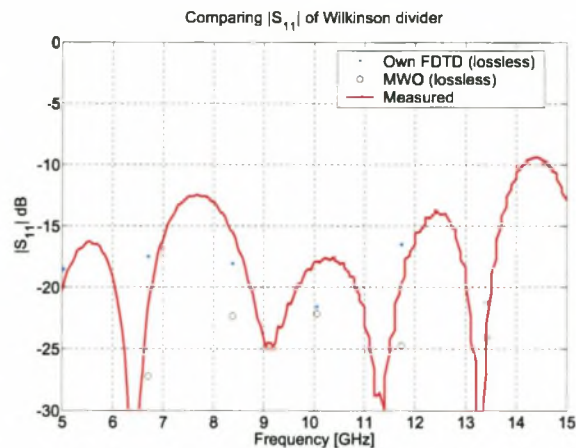


**Figure 6.11:**  $|S_{11}|$  of Wilkinson Divider Calculated using own FDTD Code and Compared with MWO and Measured Results

When comparing the results in Figure 6.10, it is shown that in the passband, the results of the experimental software agree very well with those obtained using MWO. Note that the frequency point at 13.4 GHz is off the bottom of the scale. This is possibly due to the imperfect source exciting the  $TE_{10}$  mode. (However, a corresponding effect was not observed on  $|S_{11}|$ ). The calculated variation in  $|S_{21}|$  (excluding the value at 13.4 GHz) is approximately 0.6 dB.

The calculated reflection coefficient compares better with the measured results than the MWO results. This is due to the fact that MWO uses perfect sources and it is known from earlier results that the implemented junctions were not perfect.

Figure 6.12 demonstrates some of the data accumulated during analysis of the Wilkinson divider. This is a screenshot of the  $E_x$  field component after 500 timesteps. This figure demonstrates the conductor boundary conditions; all  $E_x$  fields are zero on the conductor. Another interesting effect observed from this figure, is the magnetic wall along the symmetry axis of the divider. This indicates that the currents flowing in the  $z$ -direction of the divider are symmetrical in magnitude and phase along the symmetry line of the structure.

The power division is also demonstrated. The E-field ‘bubble’ observed at the input, splits into two equal size E-field ‘bubbles’ as is expected.

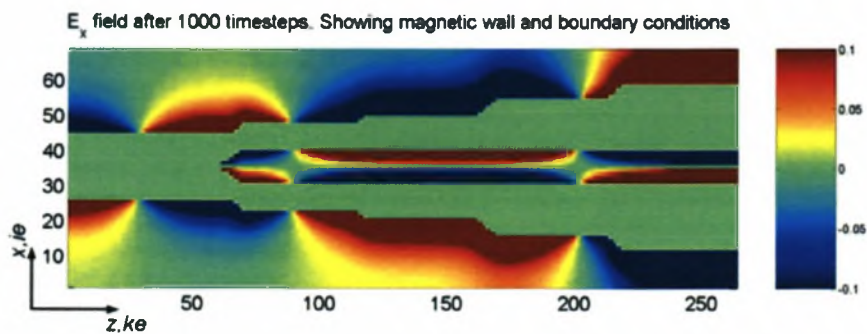


**Figure 6.12:** Picture Showing a Screenshot of  $E_x(x, z)$  field component (Computed using Own FDTD)

### 6.2.2 Analysis of the High Frequency Coupler

The  $-8.34$  dB coupler needed in the design of the  $-3$  dB high frequency coupler, designed in chapter 3.7, was analysed.

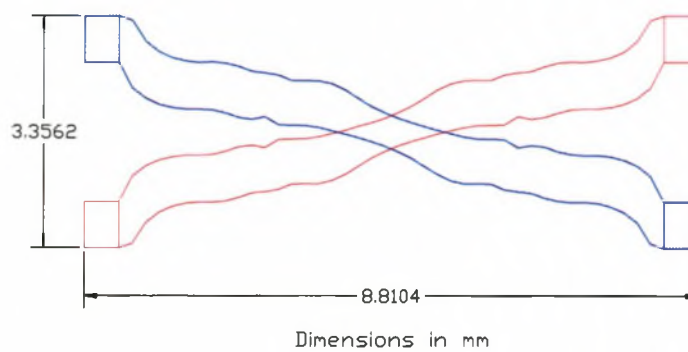


**Figure 6.13:** Layout of  $-8.34$  dB Coupler analysed Using Experimental FDTD Software.

The layout of the conductors of the coupler is shown in Figure 6.13. (A table with details of the offsets and widths is available in appendix D.) The coupler is a stripline configuration, with a dielectric constant of 2.2. The top layer and bottom layer of the coupler are separated by a distance of  $0.127$  mm. The distance between conductors and the ground plane is  $3 \times 0.127 = 0.381$  mm, making the total height of the coupler  $2 \times 0.381 + 0.127 = 0.889$  mm.

The model was analysed in the commercial FDTD package Microwave Studio from CST. Using this package, it was found that an accuracy of  $\lambda_m/100$  or  $50.5 \mu\text{m}$  resulted in a consistent result.

The limiting dimension in the coupler, is the centre substrate. In order to model this dimension properly, the thickness of the centre substrate had to be an integer multiple of the gridsize. Choosing the gridsize as  $\Delta S = 0.127/3$ , resulted in a uniform gridsize of  $42.3 \mu\text{m}$ .

The excitation was done as for the Wilkinson divider. This was a Gaussian derivative soft source, with a timestep as found from the Courant number.

The coupler was housed in a rectangular waveguide, resulting in PEC boundaries along the length of the coupler, with 10 cell UPML terminations at the four ports. The UPML parameters were selected to be the optimum as found from the literature. (Discussed in detail at the beginning of the chapter).

The final mesh resulted in matrices of size  $24 \times 106 \times 295$ . The total free memory required was 324 MB. The analysis ran for 2000 timesteps and executed for approximately 14 hours.

To calculate the S-parameters, two analyses were required. The first was a full analysis of the coupler, and the second was an analysis of a  $50 \Omega$  line (for obtaining of a reference signal). This line was the same size and location as the excitation port in the first analysis, but extended to infinity (ie. it was terminated in UPML on the far side of the computational domain).

In simulation, it was found that the method used in the previous section to calculate the S-Parameters, is very dependent on the actual positioning of the conductors. This problem was not encountered in the Wilkinson analysis, as most of the electric field was concentrated between the conductor and the bottom groundplane.

However, in the coupler, the excitation is almost symmetrical and due to the different layers, the field is sometimes more concentrated above the top conductor and other times, below the bottom conductor.

A more elegant way of finding the S-Parameters is shown in [30] and uses the basic definition of S-Parameters, namely

$$S_{ij} = \frac{V_i^-}{V_j^+} \sqrt{\frac{Z_{c1}}{Z_{c2}}}, \quad (6.45)$$

where  $Z_{c1}$  and  $Z_{c2}$  are the characteristic impedances of the transmission lines at the ports.

In this analysis they were both  $50 \Omega$ .

The voltages at the ports were calculated using a line integral over a cross-section (see Figure 6.14 and equation 6.46). [25]

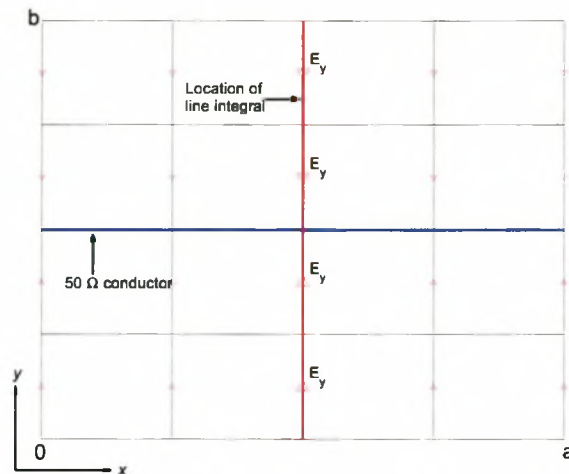


**Figure 6.14:** Location of Line Integral for Calculating the Voltage at a Port

$$V_i = \int_0^b E_y\left(\frac{a}{2}, y, z_i\right) dy \quad (6.46)$$

$z_i$  is the  $z$  position of the observation plane. This plane was placed inside the computational domain, usually 2 cells away from the UPML layer. The only exception to this, was port 1, where the observation plane was located 10 cells away from the excitation to allow evanescent waves to die out before reaching the plane.

In equation 6.45,  $V_i^-$  is the FDTD voltage measured at the output ports (reflected) using the full Wilkinson model, and  $V_j^+$  is the reference (incident) voltage obtain at port 1 using the  $50 \Omega$  line.

The calculated S-Parameters are shown in Figure 6.15. This figure also shows the results obtained for a model of similar size in MWO and CST respectively. It has to be pointed out that MWO and CST did not use cubic grids for the analysis.

The results calculated with the experimental FDTD agree very well with the results obtained using MWO. The coupling results from CST do not correspond that well with

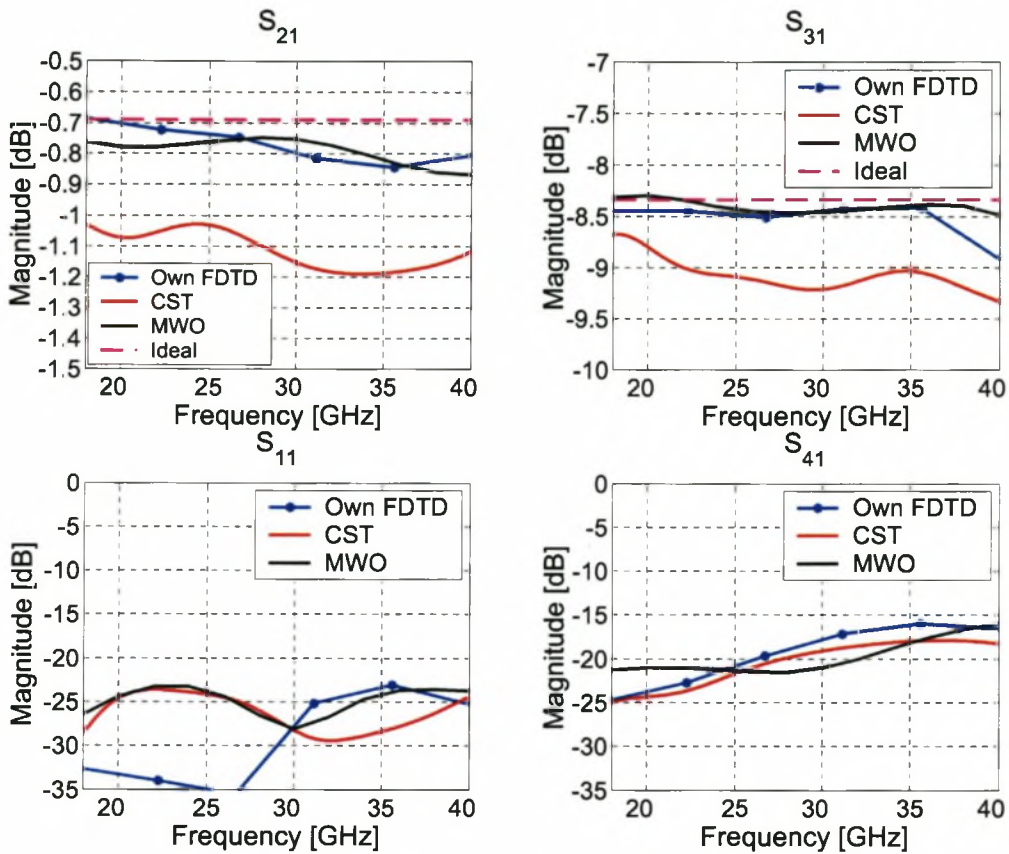


**Figure 6.15:** Magnitudes of S-Parameters of High Frequency Coupler Calculated Using own FDTD Code and Compared with MWO and CST Results

MWO and the experimental FDTD. One of the reasons for this was that CST automatically meshes a structure within certain guidelines provided by the user. However, it was not possible to get CST to coincide the mesh with the boundaries of the centre conductor. As such, this crucial dimension was not modelled correctly. It is uncertain how CST structures its grid, but it is well known that in the FDTD, if the grid does not conform to the shape of the physical boundary additional errors result. This is because the PEC boundaries are enforced on an auxiliary boundary, which is often a staircase approximation of the actual boundary. Gedney and Lansing state that often this formulation does not converge to the correct answer, no matter how fine the mesh is made. [40, p 473] This non-convergence was observed with results from CST.

In Figure 6.16, a screenshot was taken of the magnitude of the  $E_x$  field component of the coupler after 500 timesteps. The propagation along the conductor is beautifully illustrated

in this screenshot; the field incident at port one (P1) is forced to bend with the structure, so that energy will be transferred to port 2 (P2). Some of the energy has already coupled to port 3 (P3) in this figure. The effect of the boundary conditions on the conductor at port 3 is not clear in this figure as the conductor is located on a different layer.

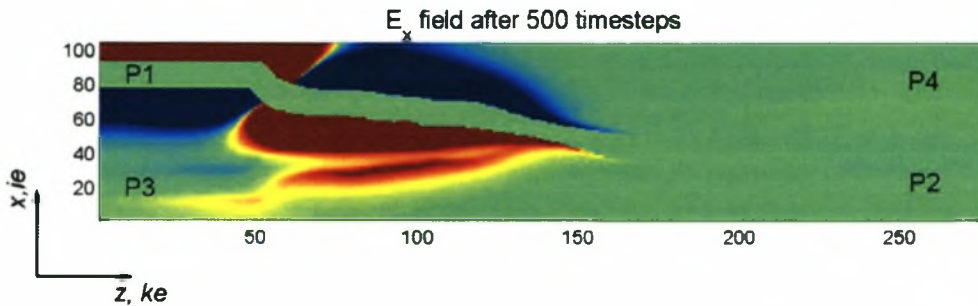


**Figure 6.16:** Picture Showing a Screenshot of  $E_x(x, z)$  Field Component of the HF Coupler (Computed using Own FDTD)

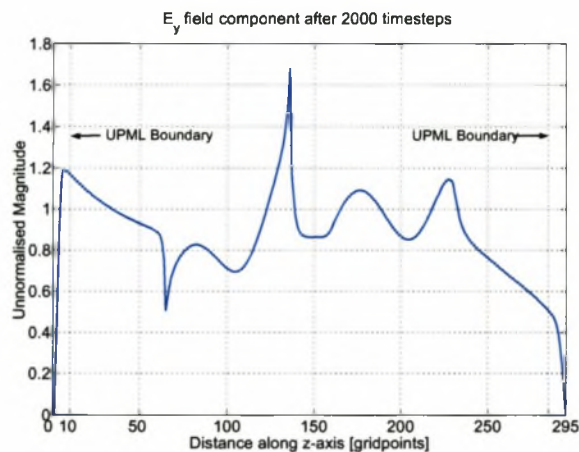


**Figure 6.17:**  $E_y(z)$  as a function of the length of the coupler, showing absorbing effect of UPML (Computed using Own FDTD)

Figure 6.17 illustrates the effect of the UPML layer on the field component that was used as excitation. The  $E_y$  component is observed in the center of structure at location ( $ie = 65, je = 11, ke = 1 : 295$ ) after 2000 timesteps. It is clearly observed that the field is forced to zero by the UPML layer. On this graph no noticeable reflection is noticed. (The UPML will cause reflections, but in order to determine how much reflections is introduced by the UPML, a reference signal with a large computational domain is required. The reference signal will be a signal free of reflections from UPML. This is not feasible to construct as such a reference would require a large amount of memory.)

## 6.3 Conclusion

The derivation of the UPML for use in three-dimensional FDTD was discussed in detail. The chapter briefly introduced common ABC's and explained why the UPML was the best boundary layer choice for the FDTD implementation.

The basic 3D implementation was tested with a Gaussian derivative source centered in a lattice. The results were compared to the literature and an excellent agreement was found.

An analysis was done on the Wilkinson divider developed in chapter 4. This required the implementation of a TEM source, perfect conductors and  $50 \Omega$  ports. The S-Parameters obtained from this analysis were compared with those obtained using MWO and with the actual measured values and were found to be in good agreement.

The chapter concluded with an analysis of the 18–40 GHz coupler designed in chapter 3.7. These results were compared with results obtained from MWO and CST and it was found that a disadvantage of the commercial time domain package is its automesh feature; the experimental FDTD code outperformed the commercial code when meshes of equal size were used. This was due to a non-accurate meshing of a crucial dimension using CST.

One of the reasons why the FDTD method was chosen for implementation of the wideband planar microwave structures, was that the FDTD method can obtain wideband frequency domain information from a single time domain pulse. While this is true, the extreme accuracy required for the structure, resulted in such a small timestep, that the amount of time necessary to obtain the time domain information was 12–14 hours. Even then, the frequency resolution was quite low.

The results did prove however, that the FDTD method is well suited for the problem as results agreed very well with measured results and those obtained using the MOM technique.

# Chapter 7

## Recommendations

The design cycle of microwave components typically include more than one physical realisation iteration. The main reason for this is that it is impossible to simulate all aspects of the physical implementation of a device. In this study, the main contributing factors to non-perfect measured results were found to be those listed below.

- Material properties are not always exactly as specified by the manufacturer. These properties include dielectric constant and loss.
- The mechanical design of the housing for the devices may be impractical. In trying to gain access to hidden parts, damage was done to the sensitive transition sections.
- The transition areas were designed with analysis software with which the author was not familiar (CST) and to which only limited access was available. The results obtained were trusted and not verified independently.

These items suggest the following:

- In a second iteration, (more) accurate material properties can be used in simulation.
- The physical housing of the coupler should give easy access to all four transition sections.
- The pressure exerted on the dielectrics of the coupler should be even. This can be done by designing a box with a lid at the top and a lid at the bottom.

- Another optimisation of transition sections is strongly recommended, where special care has to be taken to use a mesh size that is fine enough. The design should also preferably be analysed in two different EM packages.
- The optimisation of subsections used in the couplers, could be done using physical lines, instead of using MWO's linear optimiser. Though time consuming, this will greatly improve results.

The experimental FDTD code has several disadvantages. These disadvantages are all due to compromises that valued simplicity and ease of implementation above all else. The FDTD code can be made more efficient by the following:

- Implementing a contour-path subcell model is highly recommended for structures whose bounding surfaces do not conform to grid planes in a uniform Cartesian mesh. [40, Chapter 10] The main difference between the cubic mesh and the diagonal split-cell model, is that with this method, a PEC boundary can also be defined along cell diagonals, thereby reducing modelling errors.
- In the experimental FDTD code, the limiting dimension was the thickness of the center dielectric. Maloney and Smith, [40, Chapter 10] introduced a technique whereby a larger grid can be used everywhere except for the dielectric. This will lower demands on memory. The method is called the 'Maloney-Smith technique for thin material sheets.'
- Another method that could be investigated, is nonorthogonal and unstructured grids [40, Chapter 11]. These grids make it possible to have high accuracy around the sections where the accuracy is needed and lower accuracy at other sections. Once again, this will lower the demands on resources.
- An important change that is recommended, is to use a local application of the UPML rather than a global application as was implemented in the experimental software. The global application resulted in a requirement for storing UPML coefficients and fields in all regions. A local application can significantly reduce the memory requirements as actual UPML region makes up a very small percentage of the region in which the FDTD has to be performed.

## Chapter 8

### Conclusion

This study investigated two complementary areas of the study of electromagnetics; namely the design of passive microwave components and implementation of time-domain computational electromagnetic software that was used in the analysis of the passive microwave components.

The development of the time domain software was useful in the sense that it resulted in a much deeper understanding of the physical interaction of fields in the microwave components. Furthermore, a greater understanding of the intricacies of EM simulation software was developed, resulting in a better ability to design components, while understanding the inherent limitations of such software.

Microwave equal division power dividers were designed in this thesis. Specifically a broadband Wilkinson power divider, a directional coupler operating between 6.2 and 13.8 GHz and a high frequency directional coupler operating between 18 and 40 GHz were designed. The design details were discussed and attention was given to the EM implementation of the designs and to issues relating to physical implementation of microwave planar components.

Two of the devices were built and showed to be in good agreement with the results obtained from simulation.

A 3D FDTD code (with UPML boundary) was implemented. Results obtained were compared to the literature and two of the designed devices were implemented into the

experimental code. All these comparative implementations were in excellent agreement with the literature, with the measured results and with results obtained using commercial EM simulation packages.

The thesis concluded by making recommendations of improvements that can be made to the physical component designs and suggested different gridding techniques that can be implemented in the experimental FDTD code.

# Appendix A

## Calculation of the Port Reflections for the Wilkinson Power Divider

### A.1 Calculation of $S_{11}$

To calculate  $S_{11}$  for the Wilkinson power divider, the even and odd mode analysis method is used. The impedance seen at the input port will be calculated for the even and odd mode and from this,  $S_{11}$  can be calculated. The node names that will be used in the derivation are defined in Figure A.1. For example,  $Z_{DA1}$  is the impedance that would be seen in the odd mode, when looking towards transmission line  $Z1$ .

The total input impedance seen at port 1 is the average of the input impedance seen at port 1 for the even and the odd mode.

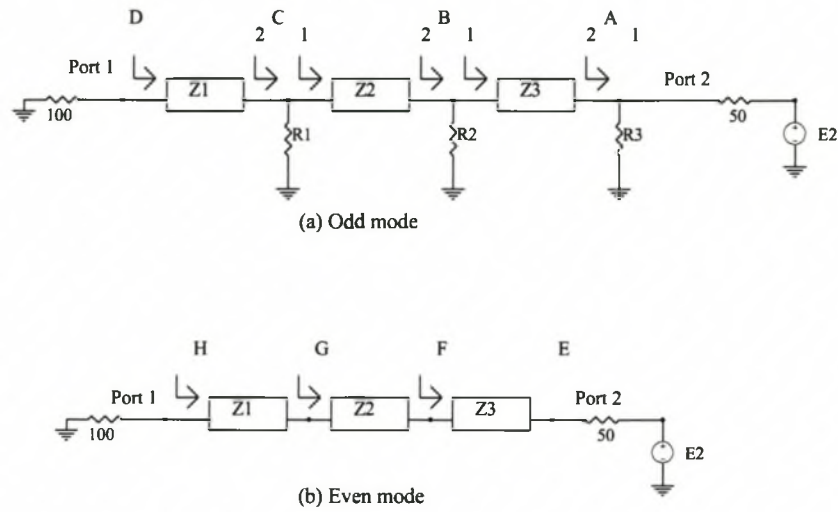


**Figure A.1:** Definition of Nodes for Calculation of  $S_{11}$  using Even and Odd Mode Analysis

**Even mode** The even mode input impedance ( $Z_{in_e}$ ) is derived from Figure A.1 and shown in A.1.

$$\begin{aligned}
 Z_F &= \frac{Z_3^2}{50} \\
 &= 66.09 \Omega \\
 Z_G &= \frac{Z_2^2}{Z_F} \\
 &= 75.65 \Omega \\
 Z_H &= \frac{Z_1^2}{Z_G} \\
 &= 100.00
 \end{aligned} \tag{A.1}$$

The input impedance at port 1 is  $Z_{in_e} = Z_H = 100.00 \Omega$ .

**Odd mode** The short circuit at port 1, results in an input impedance of  $Z_{in_o} = 0 \Omega$ .

Thus, from  $Z_{in} = \frac{Z_{in_e} + Z_{in_o}}{2}$ , the input impedance at port 1 is calculated as  $Z_{in} = 50.00 \Omega$ .

$S_{11}$  is calculated from the input impedance.<sup>1</sup>

$$S_{11} = \frac{Z_{in} - Z_0}{Z_{in} + Z_0}$$

$$S_{11} = 0 \tag{A.2}$$

$Z_0$  is the characteristic impedance of the line ( $50 \Omega$ ).

## A.2 Calculation of $S_{22}$ and $S_{33}$

$S_{22}$  and  $S_{33}$  are calculated similarly to  $S_{11}$ . The nodes used in these calculations are shown in Figure A.2.

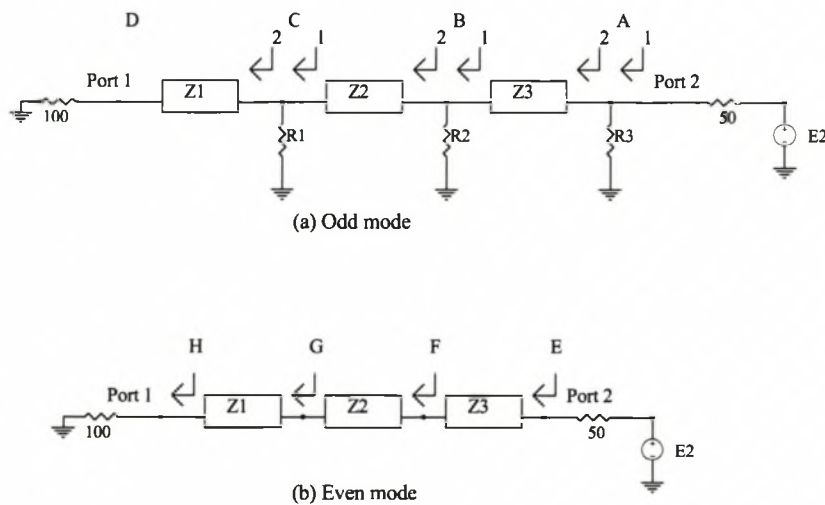


**Figure A.2:** Definition of Nodes for Calculation of  $S_{22}$  using Even and Odd Mode Analysis

<sup>1</sup>When combining the even and odd mode results, the impedance at port 1 becomes  $50 \Omega$  and it is therefore possible to obtain S Parameters

**Even Mode** The input impedance seen at port 2 for the even mode excitation is calculated in A.3.

$$\begin{aligned}
 Z_G &= \frac{Z1^2}{100} \\
 &= 75.66 \Omega \\
 Z_F &= \frac{Z2^2}{Z_G} \\
 &= 66.09 \Omega \\
 Z_E &= \frac{Z3^2}{Z_F} \\
 &= 50.00 \Omega
 \end{aligned} \tag{A.3}$$

Thus,  $Z_{in_e}$  at port 2 is  $50 \Omega$ .

**Odd Mode** The input impedance seen at port 2 for the odd mode excitation is calculated in A.4.

$$\begin{aligned}
 Z_{C2} &= \infty \text{ (Short circuit transforms to open circuit due to } 90^\circ \text{ line)} \\
 Z_{C1} &= R1 \\
 &= 53.59 \Omega \\
 Z_{B2} &= \frac{Z2^2}{Z_{C1}} \\
 &= 93.30 \Omega \\
 Z_{B1} &= Z_{B2} \parallel R2 \\
 &= 49.56 \Omega \\
 Z_{A2} &= \frac{Z3^2}{Z_{B1}} \\
 &= 66.67 \Omega \\
 Z_{A1} &= R3 \parallel Z_{A2} \\
 &= 50.00 \Omega
 \end{aligned} \tag{A.4}$$

The input impedance for the odd mode is  $Z_{in_o} = 50 \Omega$ . The total impedance seen at port 2 is  $Z_{in_2} = \frac{Z_{in_e} + Z_{in_o}}{2} = 50 \Omega$ . and the total reflection is  $S_{22} = 0$ .

Due to symmetry,  $S_{33}$  is calculated to be 0.

Thus, all ports are matched for the Wilkinson divider.

# Appendix B

## Magnetic Fields of the UPML

### B.1 Physical Location of UPML Magnetic Fields

Faraday's law is used in the deriving of the  $H$ -fields (Refer to Faraday's law, equation 6.9). The relationship between the  $H$ -field and the  $B$ -field are shown in equation B.1 [40].

$$\begin{aligned} B_x &= \mu \frac{s_z}{s_x} H_x \\ B_y &= \mu \frac{s_x}{s_y} H_y \\ B_z &= \mu \frac{s_y}{s_z} H_z \end{aligned} \tag{B.1}$$

Substituting of equation B.1 into Faraday's law results in the matrix shown in equation B.2.

$$\begin{bmatrix} \frac{\partial E_z}{\partial y} & - & \frac{\partial E_y}{\partial z} \\ \frac{\partial E_x}{\partial z} & - & \frac{\partial E_z}{\partial x} \\ \frac{\partial E_y}{\partial x} & - & \frac{\partial E_x}{\partial y} \end{bmatrix} = -\frac{\partial}{\partial t} \begin{bmatrix} \kappa_y & 0 & 0 \\ 0 & \kappa_z & 0 \\ 0 & 0 & \kappa_x \end{bmatrix} \begin{bmatrix} B_x \\ B_y \\ B_z \end{bmatrix} - \frac{1}{\epsilon} \begin{bmatrix} \sigma_y & 0 & 0 \\ 0 & \sigma_z & 0 \\ 0 & 0 & \sigma_x \end{bmatrix} \begin{bmatrix} B_x \\ B_y \\ B_z \end{bmatrix} \tag{B.2}$$

The magnetic fields are found in a similar way to the electric fields in chapter 6.

$$\begin{aligned}
B_x \Big|_{(i,j+\frac{1}{2},k+\frac{1}{2})}^{n+\frac{3}{2}} &= \frac{2\epsilon\kappa_y - \sigma_y\Delta t}{2\epsilon\kappa_y + \sigma_y\Delta t} B_x \Big|_{(i,j+\frac{1}{2},k+\frac{1}{2})}^{n+\frac{1}{2}} - \frac{2\epsilon\Delta t}{2\epsilon\kappa_y + \sigma_y\Delta t} \\
&\cdot \left[ \frac{E_z \Big|_{(i,j+1,k+\frac{1}{2})}^{n+1} - E_z \Big|_{(i,j,k+\frac{1}{2})}^{n+1}}{\Delta y} - \frac{E_y \Big|_{(i,j+\frac{1}{2},k+1)}^{n+1} - E_y \Big|_{(i,j+\frac{1}{2},k)}^{n+1}}{\Delta z} \right] \\
H_x \Big|_{(i,j+\frac{1}{2},k+\frac{1}{2})}^{n+\frac{3}{2}} &= \frac{2\epsilon\kappa_z - \sigma_z\Delta t}{2\epsilon\kappa_z + \sigma_z\Delta t} H_x \Big|_{(i,j+\frac{1}{2},k+\frac{1}{2})}^{n+\frac{1}{2}} + \frac{1}{\mu(2\epsilon\kappa_z + \sigma_z\Delta t)} \\
&\cdot \left[ (2\epsilon\kappa_x + \Delta t\sigma_x) B_x \Big|_{(i,j+\frac{1}{2},k+\frac{1}{2})}^{n+\frac{3}{2}} - (2\epsilon\kappa_x - \Delta t\sigma_x) B_x \Big|_{(i,j+\frac{1}{2},k+\frac{1}{2})}^{n+\frac{1}{2}} \right] \\
B_y \Big|_{(i+\frac{1}{2},j,k+\frac{1}{2})}^{n+\frac{3}{2}} &= \frac{2\epsilon\kappa_z - \sigma_z\Delta t}{2\epsilon\kappa_z + \sigma_z\Delta t} B_y \Big|_{(i+\frac{1}{2},j,k+\frac{1}{2})}^{n+\frac{1}{2}} - \frac{2\epsilon\Delta t}{2\epsilon\kappa_z + \sigma_z\Delta t} \\
&\cdot \left[ \frac{E_x \Big|_{(i+\frac{1}{2},j,k+1)}^{n+1} - E_x \Big|_{(i+\frac{1}{2},j,k)}^{n+1}}{\Delta z} - \frac{E_z \Big|_{(i+1,j,k+\frac{1}{2})}^{n+1} - E_z \Big|_{(i,j,k+\frac{1}{2})}^{n+1}}{\Delta x} \right] \\
H_y \Big|_{(i+\frac{1}{2},j,k+\frac{1}{2})}^{n+\frac{3}{2}} &= \frac{2\epsilon\kappa_x - \sigma_x\Delta t}{2\epsilon\kappa_x + \sigma_x\Delta t} H_y \Big|_{(i+\frac{1}{2},j,k+\frac{1}{2})}^{n+\frac{1}{2}} + \frac{1}{\mu(2\epsilon\kappa_x + \sigma_x\Delta t)} \\
&\cdot \left[ (2\epsilon\kappa_y + \Delta t\sigma_y) B_y \Big|_{(i+\frac{1}{2},j,k+\frac{1}{2})}^{n+\frac{3}{2}} - (2\epsilon\kappa_y - \Delta t\sigma_y) B_y \Big|_{(i+\frac{1}{2},j,k+\frac{1}{2})}^{n+\frac{1}{2}} \right] \\
B_z \Big|_{(i+\frac{1}{2},j+\frac{1}{2},k)}^{n+\frac{3}{2}} &= \frac{2\epsilon\kappa_x - \sigma_x\Delta t}{2\epsilon\kappa_x + \sigma_x\Delta t} B_z \Big|_{(i+\frac{1}{2},j+\frac{1}{2},k)}^{n+\frac{1}{2}} - \frac{2\epsilon\Delta t}{2\epsilon\kappa_x + \sigma_x\Delta t} \\
&\cdot \left[ \frac{E_y \Big|_{(i+1,j+\frac{1}{2},k)}^{n+1} - E_y \Big|_{(i,j+\frac{1}{2},k)}^{n+1}}{\Delta x} - \frac{E_x \Big|_{(i+\frac{1}{2},j+1,k)}^{n+1} - E_x \Big|_{(i+\frac{1}{2},j,k)}^{n+1}}{\Delta y} \right] \\
H_z \Big|_{(i+\frac{1}{2},j+\frac{1}{2},k)}^{n+\frac{3}{2}} &= \frac{2\epsilon\kappa_y - \sigma_y\Delta t}{2\epsilon\kappa_y + \sigma_y\Delta t} H_z \Big|_{(i+\frac{1}{2},j+\frac{1}{2},k)}^{n+\frac{1}{2}} + \frac{1}{\mu(2\epsilon\kappa_y + \sigma_y\Delta t)} \\
&\cdot \left[ (2\epsilon\kappa_z + \Delta t\sigma_z) B_z \Big|_{(i+\frac{1}{2},j+\frac{1}{2},k)}^{n+\frac{3}{2}} - (2\epsilon\kappa_z - \Delta t\sigma_z) B_z \Big|_{(i+\frac{1}{2},j+\frac{1}{2},k)}^{n+\frac{1}{2}} \right]
\end{aligned} \tag{B.3}$$

## B.2 Computer Position of UPML Magnetic Fields

In equation set 6.29, the E fields, as calculated for implementation on the PC were shown. The magnetic fields are derived in a similar way and are presented in B.4.

$$\begin{aligned}
 B_x|_{(i,j,k)}^{n+1} &= CAY \cdot B_x|_{(i,j,k)}^n - CBY \cdot 2\epsilon\Delta t \\
 &\cdot \left[ \frac{E_z|_{(i,j+1,k)}^{n+1} - E_z|_{(i,j,k)}^{n+1}}{\Delta y} - \frac{E_y|_{(i,j,k+1)}^{n+1} - E_y|_{(i,j,k)}^{n+1}}{\Delta z} \right] \\
 H_x|_{(i,j,k)}^{n+1} &= CAZ \cdot H_x|_{(i,j,k)}^n + CBZ \cdot \frac{1}{\mu} \\
 &\cdot \left[ (2\epsilon\kappa_x + \Delta t\sigma_x)B_x|_{(i,j,k)}^{n+1} - (2\epsilon\kappa_x - \Delta t\sigma_x)B_x|_{(i,j,k)}^n \right] \\
 B_y|_{(i,j,k)}^{n+1} &= CAZ \cdot B_y|_{(i,j,k)}^n - CBZ \cdot 2\epsilon\Delta t \\
 &\cdot \left[ \frac{E_x|_{(i,j,k+1)}^{n+1} - E_x|_{(i,j,k)}^{n+1}}{\Delta z} - \frac{E_z|_{(i+1,j,k)}^{n+1} - E_z|_{(i,j,k)}^{n+1}}{\Delta x} \right] \\
 H_y|_{(i,j,k)}^{n+1} &= CAX \cdot H_y|_{(i,j,k)}^n + CBX \cdot \frac{1}{\mu} \\
 &\cdot \left[ (2\epsilon\kappa_y + \Delta t\sigma_y)B_y|_{(i,j,k)}^{n+1} - (2\epsilon\kappa_y - \Delta t\sigma_y)B_y|_{(i,j,k)}^n \right] \\
 B_z|_{(i,j,k)}^{n+1} &= CAX \cdot B_z|_{(i,j,k)}^n - CBX \cdot 2\epsilon\Delta t \\
 &\cdot \left[ \frac{E_y|_{(i+1,j,k)}^{n+1} - E_y|_{(i,j,k)}^{n+1}}{\Delta x} - \frac{E_x|_{(i,j+1,k)}^{n+1} - E_x|_{(i,j,k)}^{n+1}}{\Delta y} \right] \\
 H_z|_{(i,j,k)}^{n+1} &= CAY \cdot H_z|_{(i,j,k)}^n + CBY \cdot \frac{1}{\mu} \\
 &\cdot \left[ (2\epsilon\kappa_z + \Delta t\sigma_z)B_z|_{(i,j,k)}^{n+1} - (2\epsilon\kappa_z - \Delta t\sigma_z)B_z|_{(i,j,k)}^n \right]
 \end{aligned} \tag{B.4}$$

# Appendix C

## UPML

### C.1 Proof that the UPML region is matched for all angles, polarisation and frequency of incident field

Stephen Gedney and Allen Tavlove proved that the UMPL is matched for  $TE_z$  polarisation [40, p298]. The appendix will complement this proof, by showing that it is also matched for  $TM_z$  polarisation and will show some of the theory that was excluded from the original proof.

Consider an arbitrarily polarised time-harmonic plane wave  $\vec{H}^{inc} = \vec{H}_0 e^{-j\beta_{1x}x - j\beta_{1y}y}$  propagating in region 1, the isotropic half-space  $x < 0$ , and incident on region 2, which is comprised of a uniaxial anisotropic medium having the permittivity and permeability tensors in C.1

$$\bar{\bar{\epsilon}}_2 = \epsilon_2 \begin{bmatrix} a & 0 & 0 \\ 0 & b & 0 \\ 0 & 0 & b \end{bmatrix}, \quad \bar{\bar{\mu}}_2 = \mu_2 \begin{bmatrix} c & 0 & 0 \\ 0 & d & 0 \\ 0 & 0 & d \end{bmatrix} \quad (C.1)$$

The plane waves will satisfy Maxwell's source free curl equations.

$$\begin{aligned}\nabla \times \vec{E} &= -j\omega\mu\vec{H} \\ \nabla \times \vec{H} &= j\omega\epsilon\vec{E}\end{aligned}\quad (\text{C.2})$$

A plane wave E-field of generalised form is shown in equation C.3.

$$\vec{E}_2 = (A\hat{x} + B\hat{y}) e^{-j\beta_{2x}x - j\beta_{2y}y} \quad (\text{C.3})$$

For the field shown in C.3, the  $\nabla$  operator ( $\nabla = \frac{\partial}{\partial x}\hat{x} + \frac{\partial}{\partial y}\hat{y} + \frac{\partial}{\partial z}\hat{z}$ ), will result in

$$\begin{aligned}\frac{\partial}{\partial x} &= -j\beta_{2x}\check{\nabla} \\ \frac{\partial}{\partial y} &= -j\beta_{2y}\check{\nabla}\end{aligned}\quad (\text{C.4})$$

or, if  $\vec{\beta}_2 = \beta_{2x}\hat{x} + \beta_{2y}\hat{y}$  then  $\nabla \times \vec{E} = \vec{\beta}_2 \times \check{\nabla} \vec{E}$ , where  $\vec{\beta}_2$  is the wavevector in anisotropic region 2.

Maxwell's curl equations for time-harmonic plane waves can then be written as

$$\begin{aligned}\vec{\beta}_2 \times \check{\nabla} \vec{E} &= \omega\bar{\mu}_2\check{\nabla} \vec{H} \\ \vec{\beta}_2 \times \check{\nabla} \vec{H} &= -\omega\bar{\epsilon}_2\check{\nabla} \vec{E}\end{aligned}\quad (\text{C.5})$$

The wavevector (in region 2) can be derived using the vector identity

$$\nabla \times \nabla \times \vec{A} = \nabla(\nabla \cdot \vec{A}) - \nabla^2 \vec{A} \quad (\text{C.6})$$

where  $\nabla$  is replaced by  $\beta$  and realising that  $\nabla \cdot \vec{D} = \nabla \cdot \vec{B} = 0$ ,

$$\begin{aligned}\nabla \times \check{\nabla} \vec{H} &= \bar{\epsilon} \frac{\partial \check{\nabla} \vec{E}}{\partial t} \\ \vec{\beta}_2 \times \check{\nabla} \vec{H} &= -\omega\bar{\epsilon}\check{\nabla} \vec{E} \\ \bar{\epsilon}^{-1}\vec{\beta}_2 \times \check{\nabla} \vec{H} &= -\omega\check{\nabla} \vec{E}\end{aligned}\quad (\text{C.7})$$

Using the vector identity, equation C.7 becomes

$$\begin{aligned}\vec{\beta}_2 \times \bar{\epsilon}^{-1}\vec{\beta}_2 \times \check{\nabla} \vec{H} &= -\omega\vec{\beta}_2 \times \check{\nabla} \vec{E} \\ \vec{\beta}_2 \times \bar{\epsilon}^{-1}\vec{\beta}_2 \times \check{\nabla} \vec{H} + \omega^2\bar{\mu}\check{\nabla} \vec{H} &= 0\end{aligned}\quad (\text{C.8})$$

Taflove and Gedney express the cross products as matrix operators and show that the solutions of the wave equation can be decoupled into forward and backward TE<sub>z</sub> and TM<sub>z</sub> modes. For the TM<sub>z</sub> case, this solution is repeated in equation C.9.

$$k_2^2 - (\beta_{2_x})^2 b^{-1} d^{-1} - (\beta_{2_y})^2 b^{-1} c^{-1} = 0 \quad (\text{C.9})$$

Assuming a TM<sub>z</sub> wave incident in region 1;

$$\vec{\tilde{E}}_1 = - E_0(1 + \Gamma e^{2j\beta_{1_x}x})e^{-j\beta_{1_x}x - j\beta_{1_y}y} \hat{z} \quad (\text{C.10})$$

the magnetic field is found from Faraday's law  $\nabla \times \vec{\tilde{E}} = -j\omega\mu\vec{\tilde{H}}$ .

$$\begin{aligned} \nabla \times \vec{\tilde{E}} = & - j\beta_{1_y}E_0(1 + \Gamma e^{2j\beta_{1_x}x})e^{-j\beta_{1_x}x - j\beta_{1_y}y} \hat{x} \\ & + (j\beta_{1_x})E_0(1 + \Gamma e^{2j\beta_{1_x}x})e^{-j\beta_{1_x}x - j\beta_{1_y}y} \hat{y} \\ & - (2j\beta_{1_x})E_0(\Gamma e^{2j\beta_{1_x}x})e^{-j\beta_{1_x}x - j\beta_{1_y}y} \hat{y} \end{aligned}$$

The magnetic field in region 1 is thus as shown in equation C.11.

$$\vec{\tilde{H}}_1 = \left[ \frac{\beta_{1_y}}{\omega\mu_1}(1 + \Gamma e^{2j\beta_{1_x}x})\hat{x} - \frac{\beta_{1_x}}{\omega\mu_1}(1 - \Gamma e^{2j\beta_{1_x}x})\hat{y} \right] e^{-j\beta_{1_x}x - j\beta_{1_y}y} \quad (\text{C.11})$$

The electric field in region 2 is assumed to consist of only a transmitted wave, and is still TM. The fields in region 2 are then as shown in equation C.12.

$$\begin{aligned} \vec{\tilde{E}}_2 &= E_0\tau e^{-j\beta_{2_x}x - j\beta_{2_y}y} \hat{z} \\ \vec{\tilde{H}}_2 &= \left[ \frac{\beta_{2_y}}{\omega\bar{\mu}_2c}\hat{x} - \frac{\beta_{2_x}}{\omega\bar{\mu}_2d}\hat{y} \right] E_0\tau e^{-j\beta_{2_x}x - j\beta_{2_y}y} \end{aligned} \quad (\text{C.12})$$

Enforcing continuity of the tangential  $E$  and  $H$  fields across  $x = 0$ , results in expressions for the reflection and the transmission coefficients.

$$\begin{aligned} \tau &= 1 + \Gamma \\ \Gamma &= \frac{\beta_{1_x}\mu_2d - \beta_{2_x}\mu_1}{\beta_{1_x}\mu_2d} \end{aligned} \quad (\text{C.13})$$

For all angles of incidence,  $\beta_{2_y} = \beta_{1_y}$ . Substituting this relation into C.9 and solving for  $\beta_{2_x}$ , results in

$$\beta_{2_x} = \sqrt{k_2^2bd - \beta_{1_y}^2c^{-1}d} \quad (\text{C.14})$$

By choosing  $\mu_1 = \mu_2$ ,  $b = c^{-1}$  and  $b = d$ , equation C.14 is simplified

$$\beta_{2_x} = d\beta_{1_x} \tag{C.15}$$

Substitution of equation C.15 into equation C.13, shows that for the TM case, the interface between regions 1 and 2 is reflectionless for all angles of wave incidence.

## Appendix D

# Detailed Track Dimensions for Couplers

The track dimensions calculated for the couplers are listed in this appendix. These numbers are used to create the polygon that becomes the coupler tracks. The length of each section of the low frequency coupler is 0.723 mm. The length of each section of the high frequency coupler is 0.22 mm.

Figure D.1 defines the location of the offsets and widths listed.

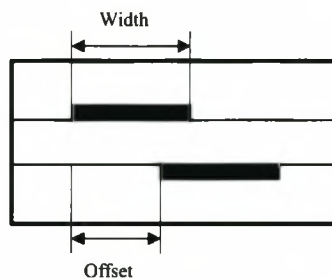


**Figure D.1:** Location of Widths and Offsets for a Broadside Coupler

**Table D.1:** Track Dimensions for Low-Frequency Coupler

<i>Section</i>	<i>Width [mm]</i>	<i>Offset [mm]</i>
1	0.6806	2.524
2	0.6794	1.96
3	0.6798	1.663
4	0.6796	1.49
5	0.679	1.395
6	0.6788	1.356
7	0.6792	1.35
8	0.6782	1.332
9	0.6767	1.24
10	0.6722	1.103
11	0.666	0.9848
12	0.6579	0.9065
13	0.6537	0.8718
14	0.6533	0.8659
15	0.653	0.8555
16	0.6374	0.7844
17	0.5949	0.6477
18	0.5293	0.4826
19	0.4655	0.3133
20	0.4274	0.1759
21	0.405	0

**Table D.2:** Track Dimensions for High-Frequency Coupler

<i>Section</i>	<i>Width [mm]</i>	<i>Offset [mm]</i>
1	0.6716	2.684
2	0.6732	1.946
3	0.6743	1.648
4	0.6743	1.476
5	0.6746	1.383
6	0.674	1.345
7	0.678	1.345
8	0.6729	1.318
9	0.6697	1.225
10	0.6681	1.091
11	0.6713	1.049
12	0.604	1.048
13	0.6475	0.8575
14	0.6466	0.8519
15	0.6445	0.8398
16	0.6296	0.7694
17	0.5865	0.6322
18	0.5182	0.4632
19	0.4539	0.2894
20	0.4178	0.145
21	0.4021	0

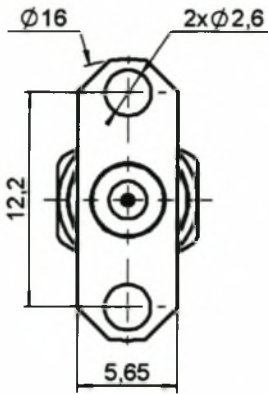
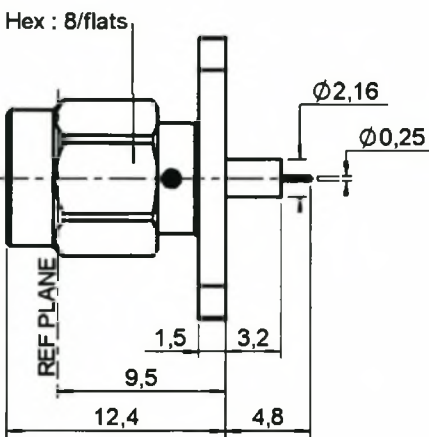
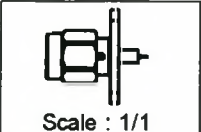
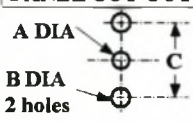
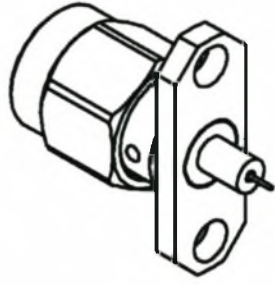
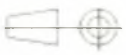
# **Appendix E**

## **Datasheets**

**E.1 Radiall R125.484.000 SMA Connector**

**E.2 Mini-Systems, Inc. Microwave Chip Resistor**

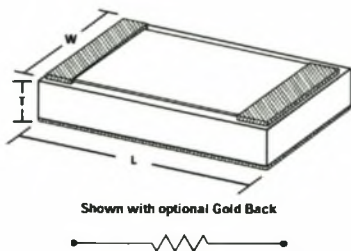
**E.3 Taconic TLY-5 Laminate**

TECHNICAL DATA SHEET		1 / 2															
<b>2 HOLES FLANGE PLUG RECEPTACLE. WITH SHOULDER CONTACT</b>		<b>R125.484.000</b> Series : SMA															
																	
 <p>Scale : 1/1</p>																	
<b>PANEL CUT OUT</b>																	
																	
<table border="1" style="margin-left: auto; margin-right: auto;"> <thead> <tr> <th colspan="3">mm</th> </tr> <tr> <th></th> <th>Maxi</th> <th>mini</th> </tr> </thead> <tbody> <tr> <td>A</td> <td>2.25</td> <td>2.2</td> </tr> <tr> <td>B</td> <td>2.65</td> <td>2.6</td> </tr> <tr> <td>C</td> <td>12.25</td> <td>12.15</td> </tr> </tbody> </table>			mm				Maxi	mini	A	2.25	2.2	B	2.65	2.6	C	12.25	12.15
mm																	
	Maxi	mini															
A	2.25	2.2															
B	2.65	2.6															
C	12.25	12.15															
																	
																	
<p>All dimensions are in mm.</p>																	
<b>COMPONENTS</b>	<b>MATERIALS</b>	<b>PLATINGS (µm)</b>															
BODY	STAINLESS STEEL	GOLD 0.5 OVER NICKEL 2															
CENTER CONTACT	BRASS	GOLD 2.5 OVER NICKEL 2															
OUTER CONTACT	-	-															
INSULATOR	PTFE	-															
GASKET	SILICONE RUBBER	-															
OTHERS PARTS	STAINLESS STEEL	GOLD 0.5 OVER NICKEL 2															
-	-	-															
-	-	-															
<p>Issue : 0222 D                  In the effort to improve our products, we reserve the right to make changes judged to be necessary.</p>																	
																	

TECHNICAL DATA SHEET			2 / 2
<b>2 HOLES FLANGE PLUG RECEPTACLE. WITH SHOULDER CONTACT</b>		<b>R125.484.000</b> Series : SMA	
<b><u>PACKAGING</u></b>		<b><u>SPECIFICATION</u></b>	
Standard	Unit	Other	
<b>100</b>	<b>'W' option</b>	<b>Contact us</b>	
<b><u>ELECTRICAL CHARACTERISTICS</u></b>		<b><u>ENVIRONMENTAL</u></b>	
Impedance	<b>50 <math>\Omega</math></b>	Operating temperature	<b>-65/+165 °C</b>
Frequency	<b>0-18 GHz</b>	Hermetic seal	<b>NA Atm.cm3/s</b>
VSWR	<b>1.06 + 0.002 x F(GHz) Maxi</b>	Panel leakage	<b>NA</b>
Insertion loss	<b>0.07* <math>\sqrt{F(GHz)}</math> dB Maxi</b>		
RF leakage	<b>-( 60 - F(GHz)) dB Maxi</b>		
Voltage rating	<b>500 Veff Maxi</b>		
Dielectric withstanding voltage	<b>1000 Veff mini</b>		
Insulation resistance	<b>5000 M<math>\Omega</math> mini</b>		
<b><u>MECHANICAL CHARACTERISTICS</u></b>		<b><u>OTHERS CHARACTERISTICS</u></b>	
Center contact retention		Assembly instruction	<b>NA</b>
Axial force – Mating end	<b>27 N mini</b>	Others :	
Axial force – Opposite end	<b>27 N mini</b>	* Coaxial Transmission Line Only	
Torque	<b>2.8 N.cm mini</b>		
Recommended torque			
Mating	<b>100 N.cm</b>		
Panel nut	<b>NA N.cm</b>		
Mating life	<b>500 Cycles mini</b>		
Weight	<b>3.264 g</b>		
<p><b>Issue : 0222 D</b> In the effort to improve our products, we reserve the right to make changes judged to be necessary.</p>			

# MICROWAVE CHIP RESISTORS

## MSMW SERIES



### MECHANICAL DATA

SERIES	L	W	T	TOLERANCE
MSMW 110	0.040" x	0.020" x	0.010"	(±0.003")
MSMW 112	0.050" x	0.050" x	0.010"	(±0.003")
MSMW 115	0.050" x	0.025" x	0.010"	(±0.003")
MSMW 118	0.021" x	0.017" x	0.010"	(±0.003")
MSMW 120	0.100" x	0.050" x	0.010"	(±0.003")
MSMW 121	0.100" x	0.100" x	0.010"	(±0.003")
MSMW 122	0.020" x	0.016" x	0.010"	(±0.003")
MSMW 124	0.150" x	0.085" x	0.010"	(±0.003")

### ELECTRICAL DATA

SERIES	OHMIC VALUE	POWER RATING @ 70°C
MSMW 110	2Ω - 18KΩ	125mW
MSMW 112	10Ω - 3KΩ	125mW
MSMW 115	2Ω - 800Ω	125mW
MSMW 118	2Ω - 300Ω	125mW
MSMW 120	5Ω - 250Ω	125mW
MSMW 121	3Ω - 3KΩ	500mW
MSMW 122	2Ω - 300Ω	125mW
MSMW 124	25Ω - 400Ω	500mW

ABSOLUTE TOLERANCE 1%, 2%, 5%, 10%  
 T.C.R. ±50ppm/°C STANDARD (NiCr); ±150ppm/°C STANDARD (TaN)

CONSULT SALES FOR OTHER VALUES / TOLERANCES AND NICHROME VALUES UNDER 50Ω.

### SERIES DATA

SUBSTRATE MATERIAL	99.6% ALUMINA STANDARD, QUARTZ** OPTIONAL
CURRENT NOISE	-20dB TYPICAL
OPERATING VOLTAGE	100 V MAX.
SHORT TERM OVERLOAD	5X RATED POWER, 25°C, 5 SEC., ±0.25% MAX. ΔR/R: ±0.1% MSI TYPICAL
HIGH TEMP EXPOSURE	150°C, 100 HRS., ±0.25% MAX. ΔR/R: ±0.03% MSI TYPICAL
THERMAL SHOCK	MIL-STD 202, METHOD 107F, ±0.25% MAX. ΔR/R: ±0.1% MSI TYPICAL
MOISTURE RESISTANCE	MIL-STD 202, METHOD 106, ±0.5% MAX. ΔR/R: ±0.1% MSI TYPICAL
STABILITY	1000 HRS., 70°C, 100% POWER, ±0.5% MAX. ΔR/R: ±0.1% MSI TYPICAL
OPERATING TEMP RANGE	-55°C TO +150°C
FREQUENCY	DC THROUGH 20 GHz
STRAY DISTRIBUTED CAPACITANCE	
ALUMINA / NiCr	0.06pF
ALUMINA / TaN	0.08pF
QUARTZ / NiCr	0.02pF
QUARTZ / TaN	0.05pF

### PART NUMBER DESIGNATION

MSMW	XX	XXXX	X	X
	SUBSTRATE / RESISTIVE FILM	OHMIC VALUE	TOLERANCE	OPTION
110, 112	AT = Alumina / TaN	5-Digit	F = 1%	F = ±100ppm/°C
115, 118	AN = Alumina / NiCr	Number: 1st	G = 2%	G = Gold Bond Pads Std.*
120, 121	QT = Quartz / TaN	4 Digits Are Significant	J = 5%	GB = Gold Backside
122, 124	QN = Quartz / NiCr	With 'R' As Decimal Point When Required.	K = 10%	T = With Solder Bumps
	PN = Polished / NiCr	5th Digit Represents Number of Zeros.		

EXAMPLES: MSMW 110AT-10001F-GB = 110 Series, Alumina Substrate, 10KΩ, ±1% Tol., ±150ppm/°C, Tantalum, Gold Backside.

MSMW 110AT-5R000K-G = 110 Series, Alumina Substrate, 5Ω, ±10% Tol., ±150ppm/°C, Tantalum, Bare Back.

\*Always used when no other option is required.

\*\*Consult sales for power capabilities on Quartz substrate

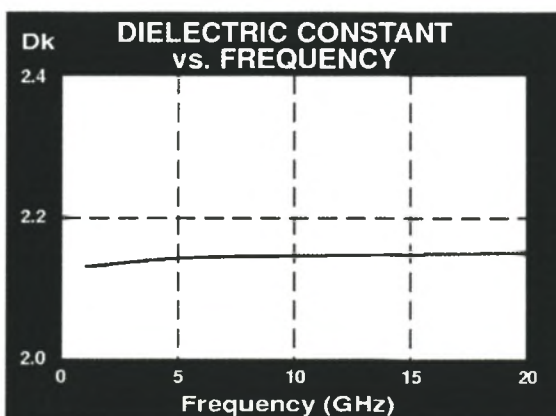
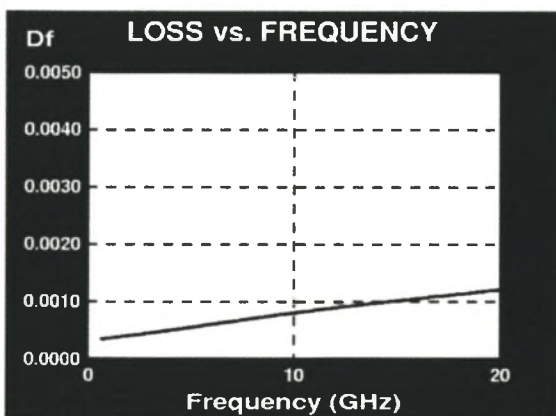
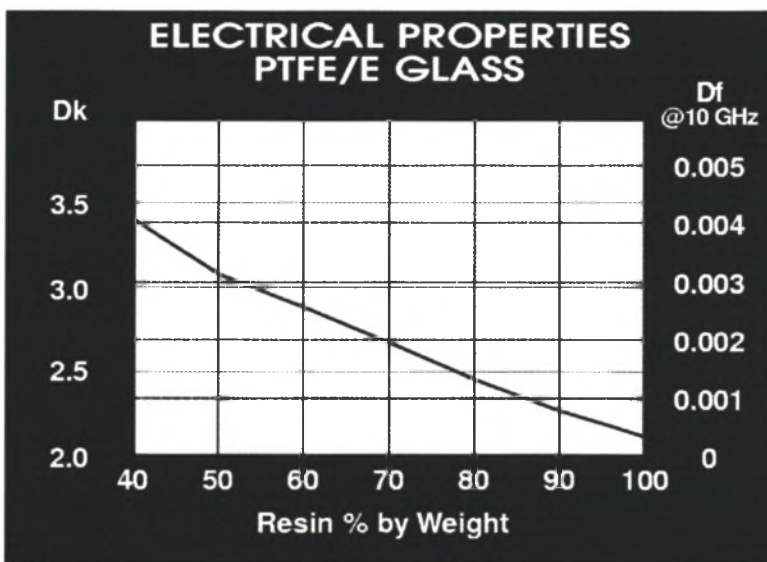


45 FRANK MOSSBERG DRIVE, ATTLEBORO, MA 02703  
 508-226-2111 FAX: 508-226-2211

DCN TF 100-C-0698

TLY-5A TYPICAL VALUES					
Property	Test Method	Units	Value	Units	Value
Dielectric Constant @ 10 GHz	IPC-TM 650 2.5.5.5		2.17		2.17
Dissipation Factor @ 10 GHz	IPC-TM 650 2.5.5.5		0.0009		0.0009
Moisture Absorption	IPC-TM 650 2.6.2.1	%	<.02	%	<.02
Dielectric Breakdown	IPC-TM 650 2.5.6	kV	>60	kV	>60
Volume Resistivity	IPC-TM 650 2.5.17.1	Mohm/cm	10 <sup>7</sup>	Mohm/cm	10 <sup>7</sup>
Surface Resistivity	IPC-TM 650 2.5.17.1	Mohm	10 <sup>7</sup>	Mohm	10 <sup>7</sup>
Arc Resistance	IPC-TM 650 2.5.1	seconds	>180	seconds	>180
Flexural Strength Lengthwise	IPC-TM 650 2.4.4	lbs./in.	>12,000	N/mm <sup>2</sup>	>83
Flexural Strength Crosswise	IPC-TM 650 2.4.4	lbs./in.	>10,000	N/mm <sup>2</sup>	>69
Peel Strength (1oz copper)	IPC-TM 650 2.4.8	lbs./linear in.	12.0	N/mm	2.1
Thermal Conductivity	Cenco-Fitch	BTU/in./hr/ft <sup>2</sup> /°F	2.79	W/m/K	0.40
x-y CTE	ASTM D 3386 (TMA)	ppm/°C	20	ppm/°C	20
z CTE	ASTM D 3386 (TMA)	ppm/°C	280	ppm/°C	280
UL-94 Flammability Rating	UL-94		V-0		V-0

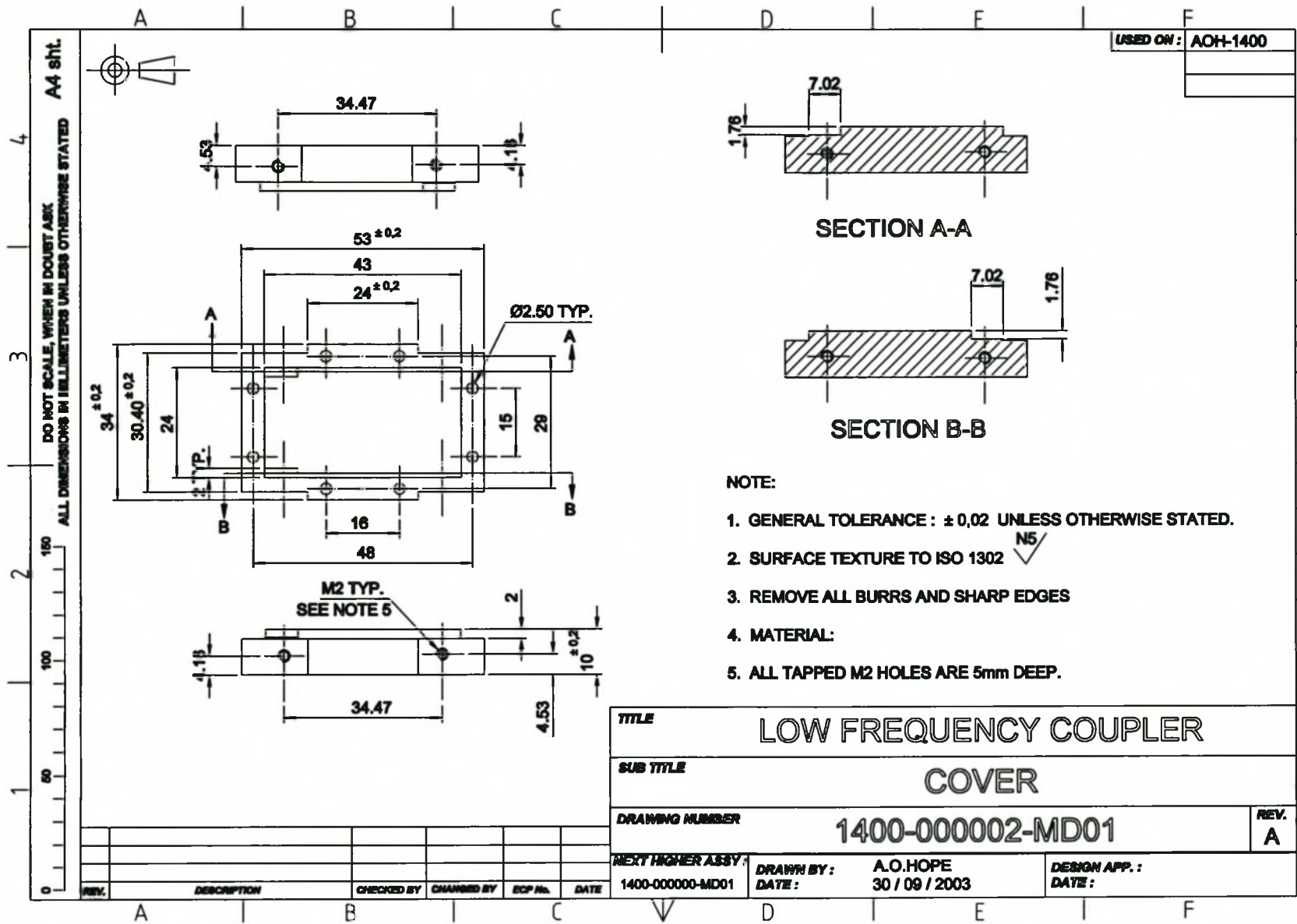
Type	Dk
TLY-5A	2.17
TLY-5	2.20
TLY-3	2.33
TLT-0   TLX-0	2.45
TLT-9   TLX-9	2.50
TLT-8   TLX-8	2.55
TLT-7   TLX-7	2.60
TLT-6   TLX-6	2.65
TLE-95	2.95
TLC-27	2.75
TLC-30	3.00
TLC-32	3.20
RF-30	3.00
RF-35   RF-35P	3.50
RF-60	6.15
CER-10	10

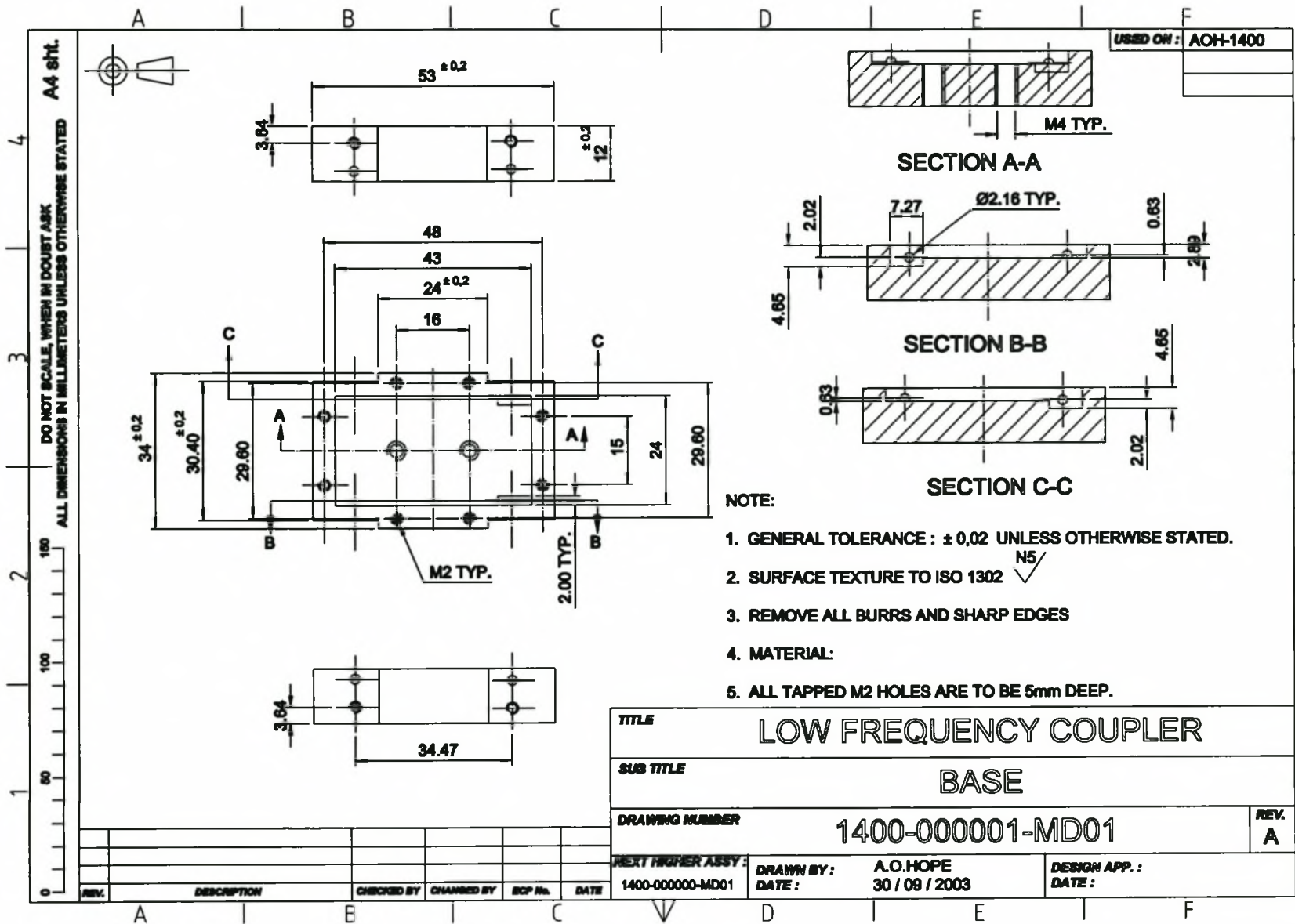


# Appendix F

## Technical Drawing

### F.1 Low Frequency Coupler





# Bibliography

- [1] Agilent Technologies. *8510 Network Analyzer User's Guide*, February 1994.
- [2] H. M. Altschuler and A.A. Oliner. Discontinuities in the center conductor of symmetric strip transmission lines. *IEEE Transactions on Microwave Theory and Techniques*, MTT-8:pp. 328–339, May 1960.
- [3] W.V. Andrew, C.A. Balanis, and P.A. Tirkas. A comparison of the Berenger perfectly matched layer and the Lindman higher-order ABCs for the FDTD method. *IEEE Microwave and guided wave letters*, 5(6):pp. 192–194, June 1995.
- [4] J.P. Berenger. A perfectly matched layer for the absorption of electromagnetic waves. *Journal of Computational Physics*, 114:pp. 185–200, 1994.
- [5] J.P. Berenger. A perfectly matched layer for free-space simulations in finite-difference computer codes. *Annales des Telecommunications*, 51:pp. 39–46, 1996.
- [6] J.P. Berenger. Perfectly matched layer for the FDTD solution of wave-structure interaction problems. *IEEE Transactions on Antennas and Propagation*, 51:pp. 110–117, 1996.
- [7] J.P. Berenger. Numerical reflection from FDTD PML's: A comparison of the split PML with the unsplit and CFS PMLs. *IEEE Transactions on Antennas and Propagation*, 50(3):pp. 258–265, March 2002.
- [8] P. Bhartia and P. Pramanick. Computer-aided models for broadside coupled striplines and millimeter-wave suspended substrate microstrip lines. *IEEE Transactions on Microwave Theory and Techniques*, MTT-36:pp. 1476–1481, November 1988.

- [9] R. Chadha and K.C. Gupta. Compensation of discontinuities in planar transmission lines. *IEEE Transactions on Microwave Theory and Techniques*, MTT-30(12):pp. 2151–2156, December 1982.
- [10] S.B. Cohn. Optimum design of stepped transmission line transformers. *IRE. Trans. Microwave Theory and Techniques*, MTT-3:pp. 16–21, April 1955.
- [11] S.B. Cohn. A class of broadband three-port TEM-mode hybrids. *IEEE Transactions on Microwave Theory and Techniques*, MTT-16(2):pp. 110–116, February 1968.
- [12] Seymour B Cohn and Ralph Levy. History of microwave passive components with particular attention to directional couplers. *IEEE Transactions on Microwave Theory and Techniques*, MTT-32(9):pp. 1046–1054, September 1984.
- [13] D.B. Davidson. *Classnotes: Electromagnetics 833, An introduction to (Radio Frequency) Computational Electromagnetics*. E & E Department, University of Stellenbosch, South Africa, 2002.
- [14] J. de Moerloose and M.A. Stuchly. Behavior of Berengers ABCs for evanescent waves. *IEEE Microwave and guided wave letters*, 5:pp. 344–346, October 1995.
- [15] R. Garg and I.J. Bahl. Microstrip discontinuities. *Int. J. Electronics*, 45(1):pp. 81–87, 1978.
- [16] S.D. Gedney. An anisotropic perfectly matched layer absorbing medium for the truncation of FDTD lattices. *IEEE Transactions on Antennas and Propagation*, 44(12):pp. 1630–639, December 1996.
- [17] S.D. Gedney. An anisotropic PML absorbing media for the FDTD simulation of fields in lossy and dispersive media. *Electromagnetics*, (16):pp. 399–415, 1996.
- [18] J.S. Izadian and S.M. Izadian. *Microwave transition design*. Artech House, USA, first edition, 1988.
- [19] Harlan Howe Jr. Stripline is alive and well. *Microwave Journal*, 14:pp 25, 1971.
- [20] Harlan Howe Jr. *Stripline circuit design*. Artech House, USA, first edition, 1974.
- [21] David W Kammler. The design of discrete n-section and continuously tapered symmetrical microwave TEM directional couplers. *IEEE Transactions on Microwave Theory and Techniques*, MTT 17(8):pp. 577–590, August 1969.

- [22] D.S. Katz, E.T. Thiele, and Allen Taflove. Validation and extension to three dimensions of the Berenger PML absorbing boundary condition for FDTD meshes. *IEEE Microwave and Guided Wave letters*, 4(8):pp. 268–270, August 1994.
- [23] Inder Bahl K.C. Gupta, Ramesh Garg and Prakash Bhartia. *Microstrip Lines and Slotlines*. Artech House, Norwood, USA, second edition, 1996.
- [24] J.S. Lim, S.W. Lee, C.S. Kim, J.S. Park, D. Ahn, and S Nam. A 4:1 unequal Wilkinson power divider. *IEEE Microwave and Wireless Components Letters*, 11(3):pp. 124–126, March 2001.
- [25] Z. Lin and K. Naishadham. A simple method to correct the reflection error of absorbing boundary condition in the FDTD analysis of waveguides. Technical report, Wright State University, Department of Electrical Engineering, Dayton, OH 45435, 1998.
- [26] Rajesh Mongia, Inder Bahl, and Prakash Bhartia. *RF and Microwave coupled-line circuits*. Artech House, 685 Canton Street, Norwood, USA, first edition, 1999.
- [27] Institute of Electrical Engineers. *MMIC design*, volume 1 of *Circuits and Systems*. The Institution of Electrical Engineers, London, United Kingdom, 1995.
- [28] S.I. Orlov. Concerning the theory of nonuniform transmission lines. *Journal of Technical Physics of USSR*, (1):pp. 2284–2294, January 1957.
- [29] C. Pelster. A 2–18 GHz image-rejection mixer. Master’s thesis, University of Stellenbosch, Stellenbosch, South Africa, February 1991.
- [30] A.C. Polycarpou, P.A.Tirkas, and C.A. Balanis. The Finite-Element Method for modeling circuits and interconnects for electronic packaging. *IEEE Transactions on Microwave Theory and Techniques*, 45(10):1870, October 1997.
- [31] David M. Pozar. *Microwave Engineering*. John Wiley & Sons, Inc, USA, second edition, 1998.
- [32] K.P. Prokopidis, N.V. Kantartzis, and T.D. Tsiboukis. Performance optimization of the PML absorber in lossy media via closed-form expressions of the reflection coefficient. Dept. of Electrical and Computer Engineering, Aristotle University of Thessaloniki, GR 54006 Thessaloniki, GREECE.

- [33] S. Ramo, John R. Whinnery, and Theodore van Duzer. *Fields and waves in communication electronics*. John Wiley & Sons, USA, third edition, 1994.
- [34] Z.C. Sacks, D.M. Kingsland, R. Lee, and J.F. Lee. A perfectly matched anisotropic absorber for use as an absorbing boundary conditions. *IEEE Transactions on Antennas and Propagation*, 43:pp. 1460–1463, 1995.
- [35] M.C. Scardelletti, G. E. Ponchak, and T.M. Weller. Miniaturized Wilkinson power dividers utilizing capacitive loading. *IEEE Microwave and Wireless Components letters*, 12(1):pp 6–8, January 2002.
- [36] D.M. Sheen, S.M. Ali, M.D. Abouzahra, and J.A. Kong. Application of the Three-Dimensional Finite-Difference Time-Domain Method to the analysis of planar microstrip circuits. *IEEE Transactions on Microwave Theory and Techniques*, 38(7):pp. 849–857, July 1990.
- [37] J.P. Shelton. Impedances of offset parallel-coupled strip transmission lines. *IEEE Transactions on Microwave Theory and Techniques*, MTT-39:pp. 2123–2128, December 1991.
- [38] R. Shelton, J. Wolf, and R. van Wagoner. Tandem couplers and phase shifters for multi-octave bandwidth. *Microwaves*, pages pp. 14–19, April 1965.
- [39] Warren L. Stutzman and Gary A. Thiele. *Antenna Theory and Design*. John Wiley & Sons, Inc, USA, second edition, 1998.
- [40] Allan Tavlove and Susan C. Hagness. *Computational electrodynamics: The finite-difference time-domain method*. Artech House, Norwood, USA, second edition, 2000.
- [41] C.P. Tresselt. The design and construction of broadband, high-directivity, 90 degree couplers using nonuniform line techniques. *IEEE Transactions on Microwave Theory and Techniques*, MTT-14:pp. 647–656, December 1966.
- [42] J.S. Wight, O.P. Jain, W.J. Chudobiak, and V. Makios. Equivalent circuits of microstrip impedance discontinuities and launchers. *IEEE Transactions on Microwave Theory and Techniques*, pages pp. 48 – 52, January 1974.
- [43] Z. Wu and J. Fanc. Numerical implementation and performance of perfectly matched layer boundary condition for waveguide structures. *IEEE Transactions on Microwave Theory and Techniques*, 43(12):pp. 2676–2683, December 1995.

- [44] K.S. Yee. Numerical solution of initial boundary value problems involving maxwell's equations in isotropic media. *IEEE Transactions on Antennas and Propagation*, 14:302-307, 1966.